12-2012

Refractive Index Chemical Sensing with Noble Metal Nanoparticles

Phillip Blake
University of Arkansas, Fayetteville

REFRACTIVE INDEX CHEMICAL SENSING WITH NOBLE METAL NANOPARTICLES

REFRACTIVE INDEX CHEMICAL SENSING WITH NOBLE METAL NANOPARTICLES

A dissertation submitted in partial fulfillment
of the requirements for the degree of
Doctor of Philosophy in Chemical Engineering

By

Phillip Blake
University of Utah
Bachelor of Science in Chemical Engineering, 2008

December 2012
University of Arkansas

ABSTRACT

Chemical sensing is a key component in modern society, especially in engineering applications. Because of their widespread impact, improvements to chemical sensors are a significant area of research. One class of sensors, plasmonic sensors, is being heavily researched because of their ability to detect low levels of analyte in near real time without destroying the analyte. This work studies a new class of plasmonic sensor that utilizes diffractive coupling to improve sensor performance. Specifically, this work outlines the first study of diffractive coupling sensors with typical nanoparticle shapes. Sensitivity of this new class of sensor is directly compared to typical localized surface plasmon resonance sensors. Spectral peak location sensitivity was found to be equal to or greater than typical plasmonic sensors. These results were corroborated with numerical simulation with and without nanoparticle interaction to demonstrate the power of harnessing diffractive coupling in nanoparticle sensors.

The sensing results were then extended to analyze ordered arrays of nanorings. Nanorings were chosen because they have the highest reported sensitivity of any plasmonic shape (880 nm/RIU) in the literature and have a high surface area to volume ratio, which is a key parameter for plasmonic sensors. Theoretical simulations of diffractive coupling nanorings indicate that sensitivity is comparable to non-coupling nanorings in the literature (890 nm/RIU vs. 880 nm/RIU, respectively). Another metric of sensor performance, the figure of merit, was much higher (34) than the non-coupling ring (2). Ordered nanoring arrays which exhibit diffractive coupling improve upon current refractive index based plasmonic sensors. Further improvements to nanoring sensors' figure of merit are possible based on simulation results for nanosphere arrays.

This dissertation is approved for recommendation
to the Graduate Council.

Dissertation Director:

_____

Dr. D. Keith Roper

Dissertation Committee:

_____

Dr. Tom O. Spicer

_____

Dr. Greg Thoma

_____

Dr. Rick Ulrich

_____

Dr. Morgan Ware

DISSERTATION DUPLICATION RELEASE

I hereby authorize the University of Arkansas Libraries to duplicate this dissertation when needed for research and/or scholarship.

Agreed _____
Phillip Blake

Refused _____
Phillip Blake

ACKNOWLEDGEMENTS

This work is the culmination of many years of dedicated study and interest. It is important that I give credit to all those who made this work possible and who gave me opportunities to succeed in my research. Foremost, I would like to thank and acknowledge my advisor, Dr. D. Keith Roper. He provided an opportunity for me to pursue a graduate degree and take part in research that is both intriguing and important to the world. I would not have been able to accomplish this research without his guidance. I have benefited greatly from his compassion for his students. I would also like to thank my committee members, Drs. Greg Thoma, Tom O. Spicer, Rick Ulrich, and Morgan Ware for their support of my work.

I would also like to acknowledge Dr. George Uhlig, who gave me an opportunity as a young college student to learn how enjoyable research can be and taught me to value time with friends and family. I have had the opportunity to work with many wonderful people. I would like to thank Dr. Wonmi Ahn for her help when I was a new graduate student and for the helpful conversation that we had over many a lunch. I have benefited from many interactions with other graduate students in my research group as well: Dr. Aaron Russell, Drew DeJarnette, Braden Harbin, Gyoung gug Jang, Ben Taylor, Udayarka Karra, Nick Kamerath, and Laura Velasco. There are too many undergraduates to list them all, but they have all been wonderful to work with, but I do want to acknowledge those whom I worked with participating in research experiences: Shawn Coleman, Shawn Cherry, Sophie Kühne, Alison Thoma, Jara Obermann, and James Proctor.

I also want to acknowledge Frontier Scientific and Dugway Proving Grounds for giving me a chance to apply the principles that I was learning in my courses to real-world chemical

engineering problems. I am thankful for those who have provided funding for my research, especially the National Science Foundation.

Finally, none of this would have been possible without those of my family who have encouraged me. I am grateful to my parents, Bruce and Deborah Blake, for teaching me to love to learn. I am grateful for the support of all my siblings, who believed in me even when it was hard for me to believe in myself. I also owe much to my wife, Valerie, who has inspired me to be my very best.

DEDICATION

I dedicate this dissertation to my wife Valerie and my children Peter and Logan. There is no greater joy than spending time with those you love.

TABLE OF CONTENTS

LIST OF FIGURES

LIST OF TABLES

LIST OF NOMENCLATURE

ABBREVIATIONS

CDA	COUPLED DIPOLE APPROXIMATION
DDA	DISCRETE DIPOLE APPROXIMATION
DPN	DIP PEN NANOLITHOGRAPHY
EBL	ELECTRON BEAM LITHOGRAPHY
EM	ELECTROMAGNETIC
EUV	EXTREME ULTRAVIOLET
FDTD	FINITE DIFFERENCE TIME DOMAIN
FIB	FOCUSED ION BEAM
FOV	FIELD OF VIEW
FOM	FIGURE OF MERIT
FWHM	FULL WIDTH AT HALF MAXIMUM
HSQ	HYDROGEN SILSESQUIOXANE
LIL	LASER INTERFERENCE LITHOGRAPHY
LSPR	LOCALIZED SURFACE PLASMON RESONANCE
NIL	NANOIMPRINT LITHOGRAPHY
NIR	NEAR INFRARED
NP	NANOPARTICLE
NPGS	NANO PATTERN GENERATION SYSTEM
NSL	NANOSPHERE LITHOGRAPHY
PDMS	POLYDIMETHYLSILOXANE
PMMA	POLY(METHYL METHACRYLATE)
RI	REFRACTIVE INDEX
RIU	REFRACTIVE INDEX UNIT
RSA-CDA	RAPID, SEMI-ANALYTIC COUPLED DIPOLE APPROXIMATION
SEM	SCANNING ELECTRON MICROSCOPE
SERS	SURFACE ENHANCED RAMAN SCATTERING
SPP	SURFACE PLASMON POLARITON

SYMBOLS

α_i	SCALAR POLARIZABILITY OF PARTICLE *i*
λ	*WAVELENGTH, nm*
A	SENSOR SURFACE AREA, cm^2
A_{img}	NANOPARTICLE AREA IN IMAGE, *pixels*
A_{xc}	NANOPARTICLE CROSS-SECTIONAL AREA, cm^2
D	NANOPARTICLE CIRCLE EQUIVALENT DIAMETER, *nm*
d_x	INTER-PARTICLE SPACING IN X DIRECTION, *nm*
d_y	INTER-PARTICLE SPACING IN Y DIRECTION, *nm*
E_{LOC}	LOCAL ELECTRIC FIELD
E_O	INCIDENT ELECTRIC FIELD
h	NANORING HEIGHT, *nm*
k	WAVE VECTOR, nm^{-1}
N_{NP}	NUMBER OF NANOPARTICLES IN SENSOR SURFACE AREA
n	LOCAL REFRACTIVE INDEX
P	NANOPARTICLE PERIMETER, *pixels*
P_i	POLARIZATION VECTOR OF PARTICLE *i*
ΔRU	CHANGE IN RESPONSE UNITS, *nm*
ΔRI_M	CHANGE IN REFRACTIVE INDEX OF SURROUNDING MEDIUM, *RIU*
r_{ij}	DISTANCE BETWEEN PARTICLES *i* AND *j*, *nm*
r_{in}	NANORING INNER RADIUS, *nm*
S	SENSITIVITY, *nm/RIU*
t	NANORING THICKNESS, *nm*

CHAPTER 1

PLASMONIC SENSORS

1.1 MOTIVATION FOR PLASMONIC CHEMICAL SENSORS

Chemical sensing is a key component in modern society, especially in engineering applications. Chemical sensors are used to control and monitor emissions, improve product purity, ensure safe working conditions, and diagnose disease.[8,9] Because of their widespread impact, improvements to chemical sensors are a significant area of research. A specific example where improved sensors could be beneficial is in blood glucose level testing. Diabetes is a condition that affects 25.8 million people in the United States.[10] Current methods for testing blood glucose levels require a blood sample to be placed on a chemical sensor. This process is both invasive and painful. Recent research has shown a correlation between blood glucose levels and acetone in exhaled breath.[11] Detection for this research utilized a gas chromatograph to detect the acetone levels in parts per million, which is not a feasible solution for in-home detection because of costs, lack of portability, and time between sample collection and results. Localized surface plasmon resonance (LSPR) based sensors are a potential solution to allow monitoring blood glucose levels in a non-invasive and cost effective method. Current LSPR sensors have demonstrated sensing of specific materials on the zeptomolar scale when immobilizing the analyte molecules in question to the nanoparticle (NP) surface.[12] However, these methods require that the analyte adsorb to the NP surface. The number of molecules detected in the cited study is ~60,000. Improvements need to be made to allow the detection of acetone from breath, since reported concentrations would only have 50-1000 acetone particles in the sensing volume of a 90 nm spherical NP.

Chemical sensors exist in a wide variety of formats, but can be grouped into several key groups based on their method of detection.[13,14] Electrical sensors take advantage of differences in resistance, current, or voltage for a sensor material when exposed to an analyte. Each class of electrical sensor has its own benefits and drawbacks, but in general electrical sensors have a high sensitivity and a wide range of operating conditions, age quickly, are non-selective, and suffer from hysteresis. Spectroscopic sensors utilize interactions between the analyte and electromagnetic (EM) waves. Spectral sensors are capable of detecting a specific analyte without isolation, but require the analyte to be spectrally active and can potentially be affected by ambient lighting. A subclass of spectroscopic sensors is plasmonic sensors, which utilize plasmonic properties of certain materials to detect an analyte based on its refractive index (RI) relative to its surroundings. Plasmonic sensors are sensitive, portable, and low cost but need to be functionalized for specificity.

Significant research is being done with plasmonic sensors because of their ability to detect analyte in real time with high sensitivity without destroying the sample. Some examples of plasmonic sensors in the literature are the detection of brain cell activity,[15] *in vivo* blood glucose level monitoring,[16] lung cancer detection,[17] and microfluidics.[18] The research outlined in this dissertation will aid in the development of better plasmonic sensors and can expand the applications where plasmonic sensors are used. For the purposes of this work, improvements in plasmonic sensors will be determined with respect to sensitivity and figure of merit (FOM). Sensitivity is defined as the peak location shift resulting from a change in RI and has units of nm per refractive index unit (nm/RIU). FOM is the ratio of sensitivity to full width at half max of the peak used for sensing. Mathematical formulas for each of these measures are presented in Chapter 2.

The benefits of this research, however, are not limited to sensing. NPs and NP arrays are also being extensively researched for their use in energy production, including solar cell enhancements,[19–21] butanol pervaporation,[22] and improvements in heat transfer for steam powered turbines.[23] Nanoring arrays are especially interesting for photovoltaics because of their small geometric cross section.

1.2 SURFACE PLASMON RESONANCE

A surface plasmon is an oscillation of surface conduction electrons confined to a metal–dielectric interface excited by incident electromagnetic waves.[9,24–27] This oscillation, called surface plasmon resonance, exists for planar films and random or ordered nanoparticles. In planar films, this orthogonally-oscillating waveform travels parallel to the metal–dielectric interface and is called a surface plasmon polariton (SPP). In NPs, the electrons' oscillations are confined by the particle–dielectric interface, resulting in a localized surface plasmon resonance (LSPR).[27] Light of a suitable frequency will excite the surface plasmon by transferring energy into the resonant mode. As a result of these interactions with incident light, both forms of surface plasmon resonance are observed spectrally as a peak shaped response for the film or NP.[28] This oscillation of electrons also results in resonant frequency sensitivity to the RI adjacent to the metal-dielectric interface.[29–31] RI sensitivity is the basis for most plasmonic sensors.

SPP and LSPR sensors can detect analytes within a small region in the near field. This region is ~200-300 nm for SPP sensors and ~5-15 nm for LSPR sensors.[32,33] This limitation exists because plasmon modes decay exponentially as a function of distance from the surface. Many current LSPR sensors do not take advantage of effects of order in NP configuration. It has been suggested that diffractive coupling based sensors which rely on constructive interference

between NPs in ordered arrays have advantages over current SPP or LSPR sensor configurations.[32] Ordered NP arrays which exhibit this diffractive coupling have been theorized to have a more intense spectral response with a narrower peak width than current LSPR sensors. An additional benefit of diffractive coupling sensors is related to their far field diffractive coupling. It is believed that this diffractive coupling allows analyte detection in the region beyond the typical LSPR detection limit while still maintaining the detection limit of current LSPR sensors. This dissertation will examine experimental and simulated arrays of NPs with various shapes and compare them to current sensing technologies.

1.3 SPP SENSORS

SPP sensors, such as the commercially available BIACore, have been studied extensively since the groundwork of Otto and Kretchman.[34,35] Their work provided two methods for requisite momentum matching with the metallic thin film using a prism.[36] Sensors based on SPP have a typical bulk RI sensitivity of ~2 x 10^6 nm/RIU.[32,33] Since their inception, SPP sensors have be utilized to perform medical diagnostics, characterize pharmaceuticals, and monitor food and environmental safety.[9,37–39] Several important limitations exist with SPP sensors. One is the requirement of phase matching with a laser that corresponds to the SPP wavelength. This makes customizing SPP sensors for different commercial applications more difficult. The second limitation is related to the propagation length of the plasmon away from the sensing surface. The sensing signal is an average of the response to analyte in this entire region, which means that for low analyte concentrations the signal from the analyte matrix is contributing a significant portion to the overall plasmonic response. LSPR based sensors do not require a specific wavelength laser and have a much shorter propagation length, overcoming these limitations of SPP sensors.

1.4 LOCALIZED SURFACE PLASMON RESONANCE

LSPR sensors confine the plasmonic feature to a fixed NP geometry, resulting in the short decay length reported above. LSPR sensors are sensitive to the properties of the NP, namely size,[2,39–41] shape,[2,25,39,42] and elemental composition,[43–46]. LSPR sensors are typically produced with gold or silver NPs, but can and have been produced with many other plasmonic materials.[45,47,48] Silver NPs are more sensitive to RI changes but readily oxidize in sensing environments.[46] Gold, on the other hand, has a good biocompatibility for sensors located *in vivo* and resist chemical oxidation.[2] In addition to LSPR sensor sensitivity to NP characteristics, NP arrangement and inter-particle separation are also important design factors for LSPR sensors.[32,40,49–52]. Chapter 2 discusses many of the fabrication technologies that are used for creating LSPR sensors, with a focus on ordered NP array. Other methods that will not be discussed in detail include colloidal growth followed by deposition[33,53] and colloidal lithography.[54]

1.5 ORDERED NP ARRAYS

An extension of LSPR sensors utilize advanced fabrication techniques to create ordered arrays of NPs. Two main categories of ordered NP arrays exist: near field and far field. Near field sensors locate the NPs very close together to create a very intense, but small, EM field enhancement.[55] When inter-particle spacing of NPs is less than a few hundred nanometers, near field coupling occurs between adjacent NPs.[40,49,50,55] As inter-particle spacing decreases for these sensors, the EM field intensity dramatically increases. A key application of this local field enhancement is surface enhanced Raman scattering (SERS).[56,57] Significant amounts of the literature on ordered NP arrays focus on this near field enhancement to achieve very low detection limits, even single molecules.[58] Precise control of near field NP spacing allows

reproducible SERS enhancements to be achieved.[24,39] The other category of ordered LSPR sensor is those with inter-particle separations that are near or above the wavelength of incident light.[32,59] Ordered sensors can be designed such that coupling can take place for the light that is scattered between individual NPs in the array. Coupling between NPs in these arrays is a result of diffraction.

1.6 DIFFRACTIVE COUPLING

Diffractive coupling in NP arrays was first reported in 2005.[59] Diffractive coupling occurs as in phase scattered light from other NPs in the ordered array interfere constructively. This constructive interference results in an EM field enhancement for NPs in the array which is directly related to the incident EM field plus the EM field from constructively interfering scattered waves from other NPs in the ordered array. It should be noted that coupling effects are not limited to ordered arrays. However, for random NP configurations, the net far field coupling effect is zero due to constructive and destructive interference. Diffractive coupling is observed spectrally as a narrow, intense spectral extinction peak that is mainly dependent on the inter-particle distance. This diffractive coupling occurs simultaneously with the typical plasmonic response of the NPs in the array, but is a distinct feature from the LSPR feature.[60,61] Work by DeJarnette *et al.* facilitated design of diffractive coupling sensors by providing a rapid semi-analytic model to determine optimal array parameters to optimize diffractive coupling for nanospheres.[62] When the research for this dissertation was started, diffractive coupling had been observed, but no characterization of diffractive coupling sensors had been performed.

1.7 HYPOTHESIS

This work was guided by the hypothesis that gold nanorings arranged in ordered arrays with inter-particle spacings between 500-1000 nm exhibit far-field diffractive coupling. The basis

of this hypothesis was numerical results obtained for arrays of spherical nanoparticles. An equally important part of the hypothesis is that the sensitivity of diffractive nanoring sensors would be higher than current LSPR sensors. Nanorings were chosen for two reasons. First, as is shown in Table 1.1, nanoring sensors that do not exhibit diffractive coupling have the highest reported sensitivity of current LSPR sensors.[63] Second, the surface area to volume ratio of nanorings, as discussed in Chapter 5, is larger than other typical geometries examined. Nanorings arranged for diffractive coupling will result in a large, narrow extinction peak with an exceptional figure of merit based on numerical simulations.

1.8 ADVANCES IN PLASMONIC SENSING

The research that is discussed in this dissertation includes several key advances in the field of plasmonic sensors, including:

1. The first reported diffractive coupling plasmon sensor was created. This sensor was then directly compared to typical LSPR sensors with random NPs, showing that sensitivity of the diffractive coupling peak is equal to or greater than the sensitivity of random NP sensors.

2. The NP plasmon peak in ordered arrays was observed to have an increased sensitivity for ordered arrays that exhibit diffractive coupling.

3. Refractive index sensitivity normalized to the percent surface coverage by NPs in diffractive coupling ordered arrays was shown to be higher than LSPR sensors with the same shape.

4. Nanoring simulations demonstrated diffractive coupling occurs in ordered arrays of nanorings for all particle sizes and inter-particle spacings simulated.

5. Simulations for ordered arrays of nanorings showed a 15.9 % increase for the diffractive coupling peak over the plasmon peak sensitivity. These sensitivity values were in good agreement with sensitivities reported in the literature for non-interacting nanorings.

Chapters 2 and 3 will establish the experimental and theoretical framework required to accomplish this work. Chapter 4 will outline the advances with ordered nanoparticle arrays which exhibit diffractive coupling. Chapter 5 will report on simulations of ordered arrays of nanorings. Chapter 6 will summarize significant results and discuss ongoing and future applications.

TABLE 1.1: Plasmonic sensor sensitivities reported in the literature for different shape nanoparticles. A more extensive list of nanoparticle shapes are available in Mayer *et al.*[64]

Shape	Material	Sensitivity nm/RIU	FOM	Reference
Sphere	Au	76.4	0.66	Nath[53]
Cube	Ag	118	5.4	Sherry[65]
Triangle	Ag	160	2.2	Mayer[64]
Rod	Au	170	1.3	Mayer[64]
Disc	Au	200	1.7	Dmitriev[66]
Bipyramid	Au	540	4.5	Chen[67]
Stars	Au	665	5.4	Nehl[68]
Ring	Au	880	2	Larsson[63]

CHAPTER 2

NANOFABRICATION AND CHARACTERIZATION

2.1 NANOPARTICLE ARRAY FABRICATION TECHNOLOGIES

The wide range of potential applications for NP arrays has led to a large number of fabrication methods. While some researchers use the term NP array to refer to random assemblies of NPs, the focus herein will be for NP arrays with long range order which exhibit diffractive coupling. The methods for producing these ordered NP arrays include biotemplating, block-copolymer lithography, dip pen nanolithography (DPN), electron beam lithography (EBL), extreme ultraviolet (EUV) lithography, focused ion beam (FIB) lithography, laser interference lithography (LIL), nanosphere lithography (NSL), nanoimprint lithography (NIL), and X-ray lithography. Each method has its inherent benefits and limitations. A comparison of several main fabrication methods is found in Table 2.1.

EBL allows precise control of NP shape, size and inter-particle separation, but requires a conductive substrate and is slow and costly. NIL uses a master pattern to create a polymeric duplicate which can then be used to create multiple copies of the original master in an imprint resist, but requires a master produced by one of the other fabrication techniques. While this method is promising for producing many copies of an optimized pattern, it does not by itself allow control over all of the key parameters in LSPR devices. Dip pen nanolithography provides a method to manipulate on the atomic scale, but is time consuming and limited in the materials that can be deposited or manipulated. NSL has been used to produce large arrays of nanospheres, nanodisks, and nanotriangles,[69,70] in ordered patterns, but it does not allow arbitrary

shapes to be created and is difficult to eliminate defects in the resulting nanosphere templates. EBL has been used for this work due to its precise control over important fabrication parameters and equipment availability, but any of the templating methods can be used in conjunction with electroless gold plating to produce patterned features. Gold deposition and polymer liftoff is required to produce the final device.

2.2 ELECTRON BEAM LITHOGRAPHY

EBL relies on the sensitivity of a polymeric resist to exposure to electrons.[71] This resist is referred to as an electron resist. EBL is usually performed with a dedicated EBL machine or a retrofitted scanning electron microscope (SEM). The use of electrons to generate a pattern is desirable because of the short wavelength of electrons. Determination of electron wavelengths for accelerating voltages used in EBL is based on the relativistic de Broglie wavelength. For electrons at 30 kV, the wavelength is 6.98 pm. The ultimate resolution of EBL is influenced by several factors in addition to the electron wavelength. The actual area that is exposed to electrons from the electron source is larger than the wavelength of an individual electron due, in part, to the tip emission spot size, current strength of the lenses, the aperture, beam energy distribution, and shape defects in the lenses. The actual area of the electron beam ranges from 0.4 to 40.9 nm for FEI instruments like the ones used in this work, varying with spot size and accelerating voltage.

The selectivity of the developer to exposed areas versus non-exposed areas is important. The more selective the developer, the closer the feature will be to the exposed region size. As an electron enters the electron resist and substrate, there is a chance that the electron will collide with a molecule or atom, resulting in scattering. The higher the accelerating voltage, the less the electron beam will disperse as collisions occur. Monte Carlo simulations are available to model

the electron dispersion within the electron resist and substrate. Thickness of the electron resist will affect the minimum size of feature that is possible.

This research utilized two SEMs each equipped with a Nano Pattern Generation System (NPGS, JC Nabity Lithography Systems, Bozeman, MT). This system interfaces with each SEM and allows control of the electron beam to generate patterns that are created in a computer aided drafting program. The NPGS system then controls the location of the electron beam on the electron resist coated substrate to generate the pattern based on the programmed parameters. Electron resists, similar to photoresists, come in positive (exposed resist is removed) and negative (exposed resist remains). Common electron resists include poly(methyl methacrylate) (PMMA, positive), ZEP-520A, and hydrogen silsesquioxane (HSQ).

Electrons from the electron beam transfer their energy to the electron resist, resulting in a change in the polymer chain. For positive electron resists, this transfer of energy results in a chain scission event. The result of these chain scissions in the electron resist is increased solubility in the developer. When the electron resist is exposed to the developer, if the applied dose was sufficient, the patterned features will appear. This patterned area is then ready for metal deposition to form NPs.

2.3 NANOPARTICLE FORMATION

LSPR sensors can be fabricated with a number of metals. Gold and silver are the most commonly used metals for LSPR sensors. Silver NPs exhibit a higher sensitivity, but oxidize readily and are more reactive.[46,64] Silver oxidation changes the environment of the surface conduction electrons, resulting in a LSPR wavelength shift. In contrast to silver, gold NPs resist chemical oxidation. Methods of creating NPs for LSPR sensors include colloidal growth

followed by deposition,[33,53] colloidal lithography,[54] sputtering or evaporation,[72] electroplating,[73] and electroless plating (EL).[74–77] In typical EBL fabrication, the metal, commonly gold or silver, is evaporated or sputtered onto the patterned resist, creating cylindrical NPs. Previous experiments have shown some difficulty in converting these nanocylinders to nanospheres when formed with evaporation and sputtering.[76] Electroless gold plating has been shown to easily transform into gold NPs when thermally annealed.[74] Other plating methods do not allow the facile formation of nanorings from a pattern of holes. Evaporation techniques can be modified to allow for ring formation by angled deposition, but this method does not allow independent control over ring thickness and height.[78] Electroplating methods would result in structures similar to those produced with substrate selective EL plating, *i.e.* cylindrical or spheroidal.

As discussed in Chapter 3, numerical simulations for nanoparticle systems are simplest for spherical NPs. For this purpose, nanospheres were fabricated first followed by nanorings. Nanocylinders were also fabricated to compare results to other experimental data available in the literature. Nanoring fabrication is simplified by the use of electroless plating. Despite the advantages in patterning time for electroless plating, liftoff is still a difficult procedure. All of the fabricated nanoring arrays for conditions examined in Chapter 5 were destroyed during metal liftoff. This problem is not specific to EL plating, but process improvements are required for consistent sensor generation.

2.3.1 ELECTROLESS GOLD PLATING

Electroless gold plating is a versatile multistep process that can be used to create nanocylinders, nanorings, and spherical nanoparticles with the same EBL pattern.[75,76] The first step in electroless gold plating is the formation of a thin tin sensitization layer by immersion in a solution of tin (Sn^{2+}) for 3 min. This tin layer is then exposed to ammoniacal $AgNO_3$ for 2 min,

which results in silver reduction onto the tin layer. Finally, the silver is galvanically displaced by immersion in sodium gold sulfite ($Na_3[Au(SO_3)_2]$) and a reducing solution for 10 min to form the desired gold features. A key difference in EL plating and typical evaporation or sputtering is that EL plating is not specific to the substrate and is omni-directional. Figure 2.1(A) demonstrates that when EL plating is performed on surfaces templated by EBL, Au is deposited in an interconnected sheet both on the surface of the electron resist as well as the substrate. To achieve spherical nanoparticles without thermal annealing, a modified EL plating procedure was developed.[75] Figure 2.1(B-D) illustrates the different structures that are possible from the same type of lithography pattern: B) typical EL plating yields nanorings, C) Tin pre-sensitized EL plating yields cylindrical particles, and D) thermal annealing results in spheroid NPs. A scheme of EL gold plating with EBL patterned substrates is shown in Figure 2.2. First, the electron resist is spin coated onto an indium tin oxide (ITO) coated glass substrate to a desired thickness (~220 nm for this work). The electron resist is then exposed to the electron beam according to a predetermined pattern. Development of the electron resist exposes the substrate in the patterned regions, which are then tin sensitized, silver activated, and gold plated. Depending on the feature size and conditions of gold plating, the resulting structures are spheroids or nanorings. Nanorings have been shown to thermally transform into spheroid NPs when placed in an oven at 800 °C for several minutes.[76]

While many benefits exist for using EL plating for nanoring formation, several difficulties arise that are not present for more typical deposition methods. First, aqueous solutions are used for EL plating. While this is beneficial in terms of introducing the gold to the surface, several of the electron resists are slightly permeable to water. The result is a thin layer of surface deposited gold around the patterned feature. This film is observable in Figure 2.1 (B).

This film is undesirable because the gold will affect the plasmon modes of NPs on or near it. Samples that have this gold film in the background were unable to be spectrally characterized by the microscope spectrometer discussed in 2.4.2.

Second, because EL plating is non-directional, gold is plated on all exposed surfaces. This is different than evaporation or sputtering, which are directional and form distinct films on the resist and substrate surface. The result is evident in Figure 2.1 (A), an interconnected sheet of gold which is attached to the patterned elements. This results in patterned NP being sheared from the surface during liftoff. EL gold plating can be made selective for the substrate surface by moving the tin sensitization step of electroless plating before the electron resist deposition. The resulting particles have an increased circularity and form spheroid NP without thermal annealing.[75] Additional experimentation is being performed to use selective gold etching to detach the gold film on top of the electron resist from the patterned surface or block gold formation on the surface of the electron resist.

2.4 NANOPARTICLE CHARACTERIZATION

Characterization of fabricated NP sensors is a critical component of evaluating their sensing capabilities. First, because of the strong dependence of NP response to size, shape, and spacing, a thorough characterization of physical properties is required. Additionally, the sensor performance will be evaluated spectrally.

2.4.1 PHYSICAL CHARACTERIZATION

Plasmonic sensors are strongly influenced by NP size, shape, and inter-particle spacing. It is therefore important that size and shape parameters be accurately determined to compare sensor performance to other sensors in the literature and to theoretical simulations. Several sensors were fabricated for evaluation of diffractive coupling sensors. Detailed analysis of the

sensors fabricated for this work is found in Chapter 4. In addition to the diffractive sensors, random NP sensors were also fabricated using a thermal transformation of an EL plated gold film to random NP arrays.[74] Two different random NP sizes and densities were evaluated in comparison to the diffractive coupling sensors.

Sensors were imaged with a SEM to accurately determine the NP metrology. These SEM images were then analyzed using a semi-automated Matlab (Mathworks Inc, Natick, MA) program. Source for the Matlab program is included in Appendix A.1. NP symmetry is important in correlating experimental data with simulated results. Small variations in particle shape have been shown to affect EM response of NPs and NP arrays, especially for nanoring simulations.[79] The spherical nature of Au NPs fabricated were calculated using standard measures of particle diameter, circularity, and elongation.[80] Particle diameter was determined by the built in Matlab function, *regionprops*, according to the formula

$$D = \sqrt{\frac{4A_{img}}{\pi}}, \qquad \text{EQ 2-1}$$

where D is the circle-equivalent particle diameter and A_{img} is the NP area.

Circularity is the ratio

$$\frac{4\pi A_{img}}{P^2}, \qquad \text{EQ 2-2}$$

where P is the NP perimeter. Circularity approaches 1 for circular objects. Elongation is calculated by

$$1 - aspect\ ratio \rightarrow 1 - \frac{minor\ axis\ length}{major\ axis\ length} \qquad \text{EQ 2-3}$$

Elongation approaches 0 for circular objects. The value of elongation can be transformed to approach 1 for circular objects by subtracting elongation measured in EQ 2-3 from unity to obtain '1-elongation'. This transformation is performed to improve visual comparisons between circularity and elongation in data analysis by selecting a common basis where a perfect circle is 1.

2.4.2 SPECTRAL CHARACTERIZATION

Spectral characterization of NP systems is an important step in characterizing a NP sensor. As previously mentioned, SPR features are observed in the measured spectral response from a sample. These spectral data are then analyzed to determine the peak positions in different RI environments to calculate sensitivity.. For this work, two custom spectral systems were developed for sample characterization. The first spectrometer system consisted of a 6V tungsten microscope light source, a series of lenses for collimating and focusing, a polarization crystal (GT5, ThorLabs, Newton, NJ) mounted in a rotation mount (10 arcmin. resolution), a 3-axis micropositioner (25.4 μm resolution) for flow cell alignment, a 100X microscope objective (NA=0.70), additional focusing lenses, a beam splitter for visual sample positioning, and a fiber optic collimator to collect the light with a fiber optic spectrometer (AvaSpec 2048, Avantes Inc. CO). The illuminated area for this system was ~20 mm^2. Figure 2.3 shows a schematic representation of the spectrometer setup.

Effects of RI changes on the spectral characteristics of a sample are determined by exposing the sample to different liquid RI environments. Two sample holders were used for evaluation of the RI response of a sample, a 1 cm path length cuvette and a custom flow cell. A thin film of polydimethylsiloxane (PDMS) (Sylgard 184, Dow Corning, Midland, MI) was

placed between the ordered samples and the quartz cuvette to keep the samples from shifting and provide RI matching between the substrate and quartz cuvette. When this was not done, sinusoidal interference was observed in the spectral response which is attributable to a gap between the substrate and the cuvette.[81] The custom flow cell was fabricated from two polished glass slides cut into one inch squares. The upper glass slide was fitted with two NanoPorts (Upchurch Scientific, Oak Harbor, WA) which allowed for analyte introduction with minimal disruption to the flow cell. These ports were placed at opposite diagonal corners to leave a large, unobstructed region where light could be introduced to the sample and to ensure uniform distribution of analyte over the sensor surface. PDMS was used to fabricate a gasket to separate the two glass slides and provide a flow channel. The gasket was fabricated with a thickness of 0.75 mm, or 0.05 mm thicker than the sensing substrate to create the sampling chamber. Flow channels were manually cut into the PDMS to connect the ports and direct the analyte over the sensor being evaluated. A schematic of the custom flow cell is shown in Figure 2.4. Adhesive tape was used to maintain a slight pressure on the PDMS gasket to maintain a good seal when liquid was introduced. Up to seven different values of RI were used to evaluate sensor performance: air (1.00), methanol (1.328), water (1.333), acetone (1.359), ethanol (1.361), isopropanol (1.3772), and toluene (1.479).[82] Samples secured with PDMS were not tested with toluene because it is known to cause swelling in PDMS.[83] Between spectral measurements for each fluid, the cuvette was emptied of the fluid, rinsed with acetone, and air dried. Passive drying proved insufficient to fully remove the previous fluid or rinse acetone so samples were dried with breathing quality air from a compressed cylinder. Air references were taken before and after each measurement to confirm complete drying. This procedure was repeated three times for each sampling location and fluid. The data collection process was duplicated for the

ordered sample to ensure that three samples accurately represented the system. Peak positions and sensitivities for this additional data corresponded well to the initial data set. The side of the samples with the NPs was positioned ~2.3 mm from the microscope objective. The illuminated spot size was ~1.6 mm in diameter. The light was horizontally polarized for all the samples analyzed. Results obtained with the two sample holders were identical.

It is clear that this system results in the response for a large area on the sample. For systems of interacting NPs this results in a large number of interacting NPs, increasing the chance of observing inter-particle effects. Recent publications have demonstrated that as the spectral field of view is reduced to a small subset of NPs or even a single NP, the limit of detection is also reduced, which could lead to very small sample volumes.[84] The second spectral system is a reflection/transmission optical microscope (Nikon LV-100DU) equipped with a multi-grating spectrometer (Andor Shamrock 303I with Du-420A-OE detector). This system included a variable slit to reduce the number of NPs in the spectral field of view. The illuminated field of view is also variable down to ~3.0×10^{-2} mm^2. This system allows analysis of how defects and particle distributions affect the spectral signal, but is currently limited to spectral analysis of samples in air because of the short focal length between the sample and the microscope objective. This microscope spectrometer will be useful in future work to identify the influence of missing NP in ordered NP sensors and allow characterization of NP arrays on non-transparent substrates.

Sensor performance is commonly evaluated in terms of a given spectral response to RI change: peak magnitude, peak wavelength, and full width at half max (FWHM). Spectral features were identified using Matlab. Two programs were used to determine peak locations: *peakdet* and *iSignal*, both of which are available on Matlab file exchange. A Matlab script was

written to automate the peak location process with the *peakdet* program. Spectral responses, in particular peak wavelength and FWHM, are used widely to indicate sensor sensitivity. A common method of reporting sensitivity based on spectral response to RI changes is

$$S = \frac{\Delta RU}{\Delta RI_m}, \qquad \text{EQ 2-4}$$

where ΔRU is the change in spectral response and ΔRI_m is the change in RI of the surrounding dielectric medium. Response units can be signal intensity at a given wavelength, wavelength of the spectral feature, or even phase information.[85,86] The analysis herein will focus on wavelength changes for the spectral feature, but as device fabrication results in samples which better match the intense diffractive peaks observed in simulation, intensity at a fixed wavelength may result in increased sensitivity. Sensitivity is expected to be linear with respect to RI.[87] However, many publications only cite sensitivity in the range of 1.3 to 1.5.[1,67,88,89] This work will report sensitivity including the air point as air based sensitivity and excluding the air data point as methanol based sensitivity. This form of sensitivity is based upon the *aggregate* spectral response of all NPs of the sensor to a change in RI for a given spectroscopic field of view (FOV). This form of sensitivity does not directly give information about the limit of detection, the number of particles involved in the detection, or the impact of intrinsic instrument sensitivity.

An alternate measure of sensitivity has been introduced which, in addition to spectral response per change in RI, also accounts for intrinsic instrument sensitivity, active plasmon area, and spectroscopic FOV.[32] Sensitivity measurements performed on the same sensing platform allow the intrinsic sensitivity and spectroscopic FOV to be fixed. When these conditions are met, the sensitivity defined in EQ 2-4 can be adjusted to account for the amount of active

plasmonic area involved in the sensing. This modified sensitivity provides a consistent basis to compare sensitivity of different LSPR sensors and gives a better comparison between SPP and LSPR sensors. This modified sensitivity for sensors with equal intrinsic sensitivities and FOV values, reduces to:[90]

$$S_{NP} = \frac{\Delta RU}{\Delta RI} \frac{A}{A_{xc} N_{NP}}, \qquad \text{EQ 2-5}$$

where A is the area excited by the incident wave, A_{XC} is the cross-sectional area of an individual NP, and N_{NP} is the total number of NP in the area A. This figure of merit, referred to as nanoparticle sensitivity, S_{NP}, has the same units as S, but is normalized to the fraction of the surface covered with nanoparticles.

Sensitivity by itself does not fully characterize the performance of plasmonic sensors. Other factors, such as FWHM and intensity, affect how accurately peak position can be determined as well as the minimum spectral shift that can be detected. If the spectral feature is broad, it is difficult to accurately determine the peak wavelength. Low intensity makes it difficult to distinguish the sensor signal from background noise. A figure of merit (FOM) has been proposed and utilized in the literature which accounts for the effect of FWHM on the overall sensor performance.[65]

$$FOM = \frac{S}{FWHM} \qquad \text{EQ 2-6}$$

The sensors in this work will be directly compared to each other on the basis of sensitivity and FOM. These results will also be compared to reported sensor performance from the literature.

2.5 CONCLUSIONS

Nanoparticle arrays have been fabricated using EBL and EL plating to produce regular arrays of nanospheroids, nanocylinders, and nanorings. Two methods were demonstrated to produce spheroid NPs with EL plating, a thermal annealing method and a selective plating process using tin presensitization. The new selective EL plating method was shown to reduce deviations in particle size and circularity. A custom spectrometer system was fabricated to allow precise positioning of a sensor with micropositioning control over x, y, and z-axes as well as polarization and incident angle. A methodology for characterizing sensor performance based on RI sensitivity and a FWHM figure of merit was outlined.

TABLE 2.1: A COMPARISON OF NANO-FABRICATION TECHNOLOGIES.

Technology	Description	Benefits	Limitations
Direct			
EBL	Patterning of nanorings with electron beam directly in resist. Used for mask generation.	•No mask required	•Equipment cost
		•Complex patterns	•Low throughput
		•Well characterized	•Proximity effects
FIB	Ions etch material away to produce nanoring pattern	•Can directly write metal rings	•Ion mixing
		•Less long range scattering than electrons	•Implanted dopants
			•Altered optical properties
DPN	AFM tip deposits “ink”	•Complex patterns	•Substrate dependent “ink”
			•Low throughput
NSL	Microspheres are used as a mask for evaporation followed by ion etching	•Can produce large area patterns	•Line and pin defects
		•Inexpensive	•Limited lattice configurations (hex, square)
Indirect			
(Require a mask or pattern from another lithography method)			
EUV	Extreme UV light (λ~10 nm) used similar to photolithography	•Widely used	•Diffraction limited
		•High aspect ratios possible	•Exotic optic materials
X-ray	X-rays (λ~1 nm) used to expose resist	•Linewidth independent of substrate	•Expensive source
			•Complex mask
			•Mask gap changes resolution
NIL	Master pattern is duplicated in resist via contact	•Rapid	•Stamp deformation
		•One master produces multiple samples	•Highly sensitive to surface irregularities
Angle Resolved EBL	Angle resolved evaporation on EBL patterned holes	•Produces rings without directly patterning	•Complex Equipment
			•Height/width are not independent
EL-EBL	Electroless plating on EBL patterned holes	•Produces rings without directly patterning	•Liftoff is difficult

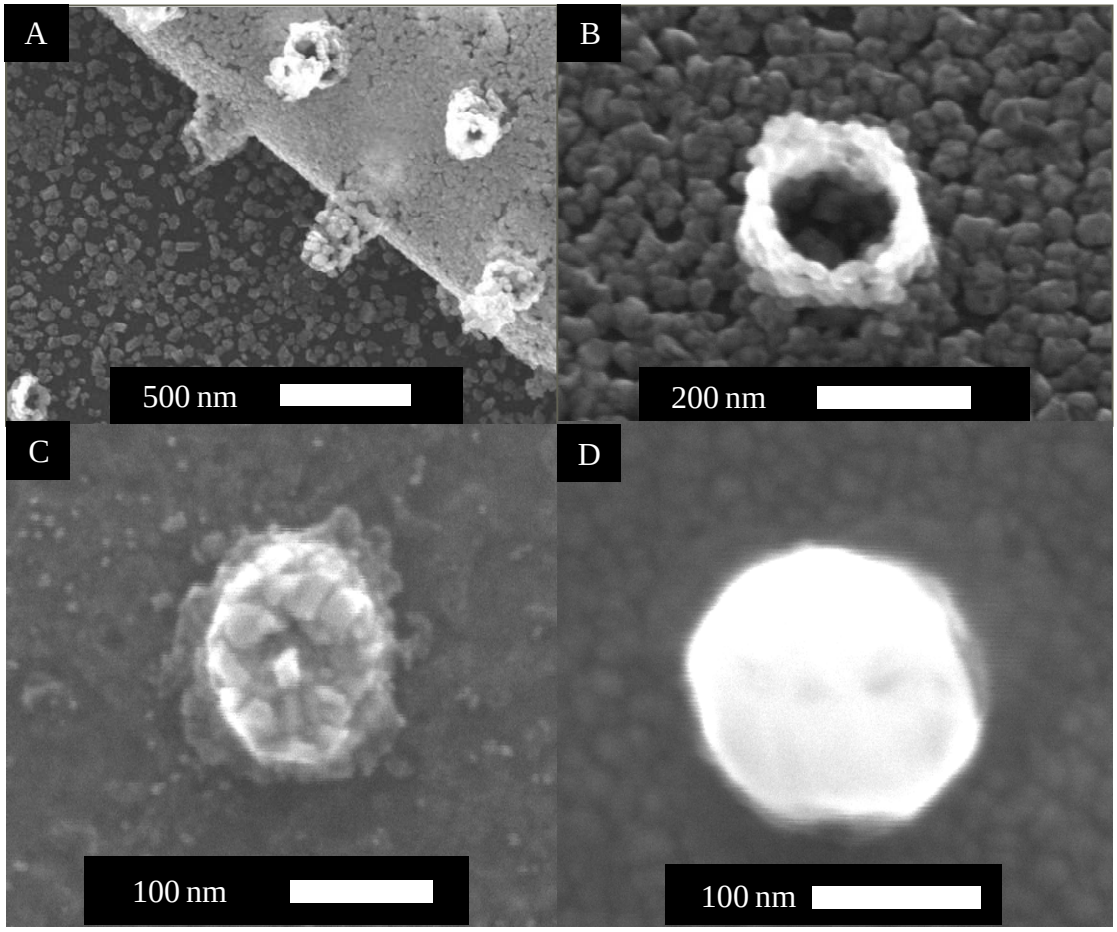

FIGURE 2.1: Structures fabricated with electroless gold plating and electron beam lithography: A) interconnected film, B) nanoring, C) nanocylinder, and D) nanosphere.

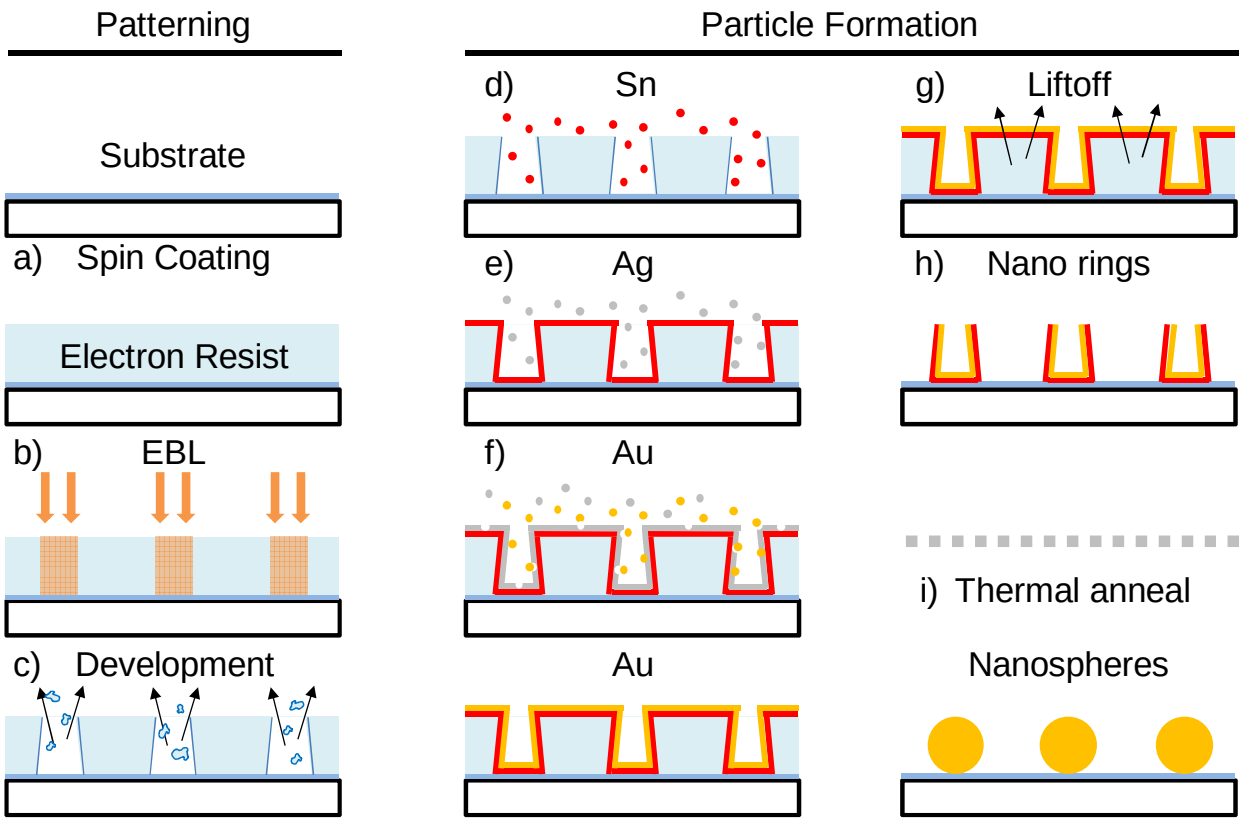

FIGURE 2.2: Scheme of EL plating with EBL to produce ordered arrays of nanorings and nanospheres.

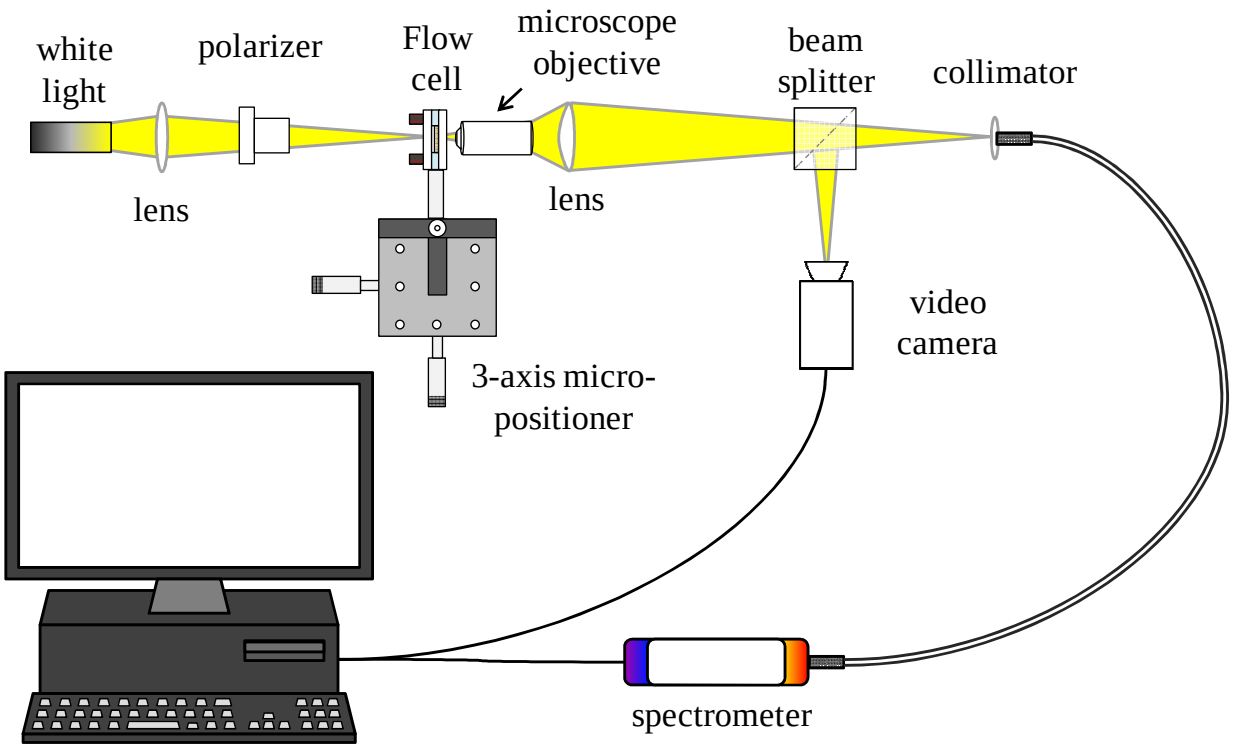

FIGURE 2.3: Illustration of primary spectroscopy system.

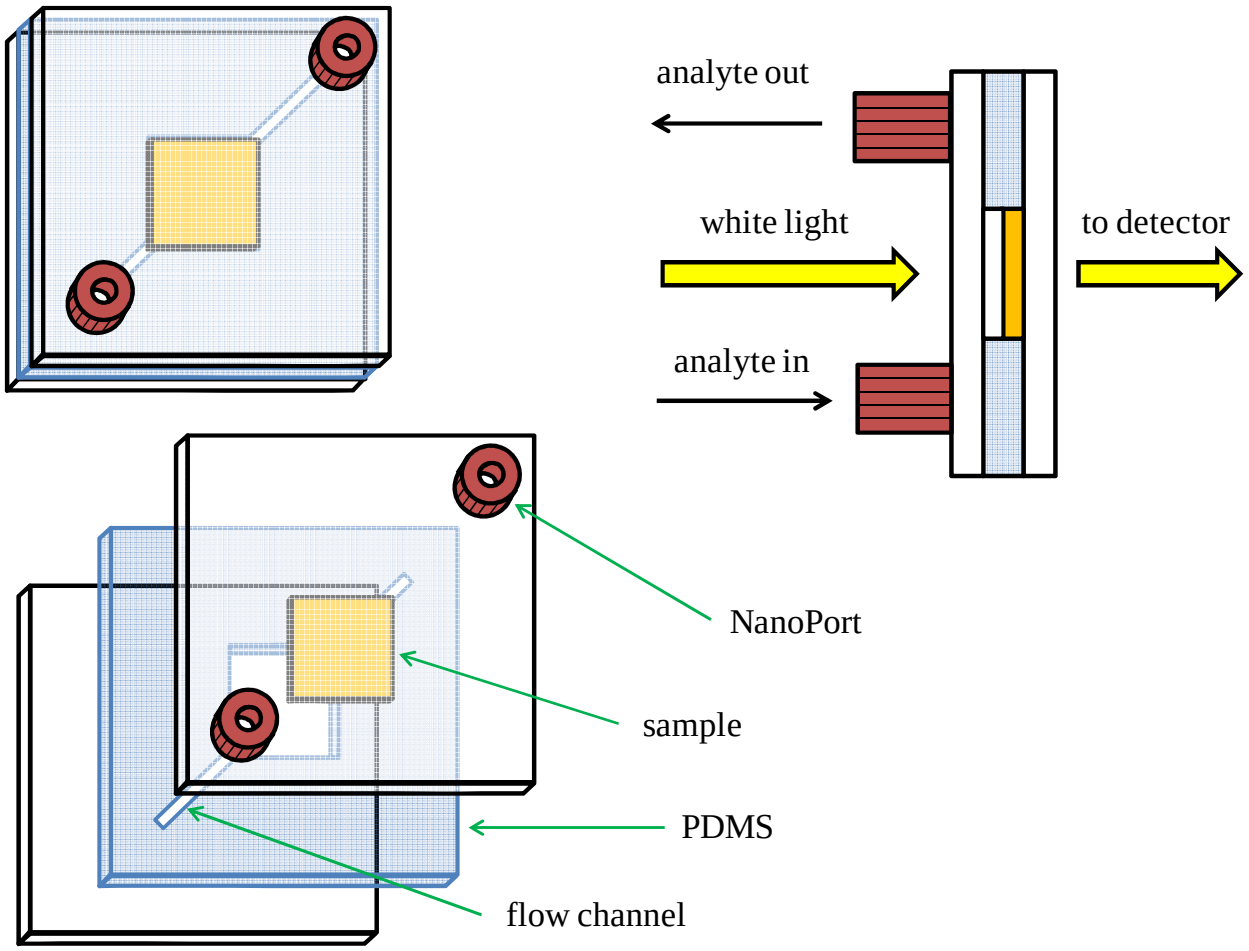

FIGURE 2.4: Schematic of custom flow cell used in the spectrometer setup shown in Figure 2.3. Top left) fully assembled view. Bottom left) showing separate layers. Right) orientation relative to light source.

CHAPTER 3

NANOPARTICLE SENSOR SIMULATION

3.1 INTRODUCTION

Nanoparticle based sensors are governed by electromagnetic (EM) interactions with light. Interactions of EM with matter are described by Maxwell's equations. While Maxwell's equations fully describe these interactions, the solution to Maxwell's equations is not always possible analytically, especially for complex shapes. Because of this, many different numerical methods of solving Maxwell's equations have been developed. Some of these methods are nominally exact methods, where the numerical results converge on the exact answer, while others make assumptions to simplify the calculations or find exact solutions for special cases. This chapter outlines some of the most common simulation methods used for evaluating nanoparticle sensors.

3.2 SUMMARY OF METHODS

A comprehensive review of different numerical methods used for NP analysis was recently published which compared the most common simulation methods.[91] Of particular interest for applications with nanorings are the finite difference time domain (FDTD) method, the discrete dipole approximation (DDA), the coupled dipole approximation (CDA), and Mie theory. Other methods exist (T-matrix, method of moments, finite element, *etc.*) but were not considered because of similarities to considered methods, lack of availability, or lack of periodic boundary condition capabilities. Of the methods considered, Mie theory and the CDA both assume spherical nanoparticles in the form used. Details on the specific implementations used for each of the considered simulation methods will be provided in the detailed description of that method in this chapter. When simulations are compared to experimental data, simulations use

the particle characteristics determined using the methods in 2.4.1. Simulations reported herein neglected the effects of the substrate, which consists of a multilayer environment of analyte–NP–ITO–glass for ordered arrays or analyte–NP–glass for random NPs. Instead, simulations assumed the nanoparticles were in a uniform RI environment. When appropriate, an effective RI was used to account for the change in local RI due to the multilayer environment. This effective RI was calculated using a weighting factor of 0.82 for the medium and 0.18 for the substrate RI, based on a uniform sensing volume shell, generating a weighted average of the medium and substrate RI.[92] A multilayer environment will red shift the LSPR and diffractive coupling frequencies, however, relative shifts in frequency due to changes RI of the medium are preserved.[93] CDA results reported in Chapter 4 utilize an experimentally determined weighting factor to better represent the effects of the substrate. A brief description of each of the simulation methods used for this work follows.

3.3 MIE THEORY

Gustav Mie determined that for spherical particles that do not interact, an exact solution to Maxwell's equations could be reached analytically.[94] This analytical solution as derived is only valid for spherical particles that do not interact. However, for random NP systems, the net interaction between particles is zero and Mie theory provides good correlation with experimental data. Mie theory was implemented in Fortran by Bohren and Hoffman, which is the basis of many of the existing Mie simulation packages.[95] A customized Matlab version of the Mie theory code developed by Maetzler was used for simulations reported herein.[96] The modified code is available in Appendix A.2. Results of the modified code were in good agreement with those produced by MiePlot (v. 4.2.03, Philip Laven), a freely available implementation of the code by Bohren and Hoffman with a graphical user interface. However, the modified code used was

faster for computations with particle distributions and returned the spectra for each of the NP sizes in the distribution.

3.4 FINITE DIFFERENCE TIME DOMAIN

FDTD is, as the name implies, a method of solving Maxwell's equations in the time domain. The target of the model is discretized in space with a desired spatial discretization $1/10^{th}$ the smallest wavelength or feature size. A benefit of FDTD is that since it is a time domain method, multiple frequencies of EM waves can be simulated simultaneously. Foundational work by Yee established an algorithm where each discretized spatial volume is solved for the electric field on the edges of the discretized volume, then stepped to the face centers of the volume to solve for the magnetic field.[97] Time discretization is strongly related to the spatial discretization volume. The simulation steps forward in time until convergence is achieved. FDTD methods can provide very accurate results, but are time and computing resource intensive. FDTD results for cylindrical particles were performed by B. Harbin. Conditions and results of this simulation can be found in our previously published work.[90]

3.5 DIPOLE APPROXIMATION METHODS

Several methods exist where Maxwell's equations are simplified by assuming that the EM field is a collection of dipoles. This approximation simplifies the integration of the electric field which results in a significant reduction in simulation times for simulated geometries where this approximation is valid. This section will discuss two similar dipole approximation methods: CDA and DDA. Although these two methods are sometimes considered the same, the difference is that CDA generally represents individual NPs as point dipoles whereas DDA typically represents a NP as a collection of individual dipoles.

3.5.1 COUPLED DIPOLE APPROXIMATION

The CDA model assumes a square array of polarizable scattering objects whose spatial dimensions are small relative to the incident wavelength such that their induced EM field can be approximated as dipolar. In addition to the dipole assumption, the CDA calculations performed for this work assume an infinite array of dipole scatterers with a uniform polarizability for each dipole in the array. The local electric field experienced by a NP *i* due to contributions from all other NPs *j* in this dipole approximation is:

$$\mathbf{E}_{loc}(\mathbf{r}_i) = \frac{\mathbf{P}_i}{\alpha_i} = \mathbf{E}_o e^{i\mathbf{kr}} - \sum_{j \neq i} \frac{e^{i\mathbf{kr}_{ij}}}{\mathbf{r}_{ij}^3} \left[k^2 \mathbf{r}_{ij} \times (\mathbf{r}_{ij} \times \mathbf{P}_j) + \frac{(1 - ik\mathbf{r}_{ij})}{\mathbf{r}_{ij}^2} (\mathbf{r}_{ij}^2 \mathbf{P}_j - 3\mathbf{r}_{ij}(\mathbf{r}_{ij} \bullet \mathbf{P}_j)) \right], \qquad \text{EQ 3-1}$$

where $\boldsymbol{P_i}$ is the polarization vector of particle *i*, $\boldsymbol{r_{ij}}$ is the distance between particles *i and j*, α_i is the scalar polarizability of particle *i*, *k* is the wave vector of the incident EM wave, $2\pi n/\lambda$, *n* is the local RI, λ is the wavelength of incident EM radiation, and $\mathbf{E}_o e^{i\mathbf{kr}}$ is the incident EM field.[98] For a symmetric, infinite array, $\boldsymbol{P_i}$ and $\boldsymbol{P_j}$ are equal. It is important to note the angle dependence that exists between the vectors $\boldsymbol{k}$, $\boldsymbol{r_{ij}}$ and $\boldsymbol{P}$. One can expand EQ 3-1 to Cartesian coordinates where each vector has components in the x, y, and z directions. By performing this transformation, it can be seen that the local EM field will be influenced by the angle of the incident light to the substrate, the polarization angle of the incident light, and whether the interacting particles are on the same plane as the induced dipole. This requires care in positioning of experimental samples when the spectral response will be compared to theoretical simulations.

Work by DeJarnette, Taylor, and Roper has resulted in a rapid, semi-analytical solution for the coupled dipole approximation (rsa-CDA).[32,62] The rsa-CDA implementation greatly reduces the required computation time for periodic arrays of spherical NPs. This allows the evaluation of thousands of different NP sizes and inter-particle spacings within a few hours. Optimal parameters for NP spacing for spherical NPs were determined with the rsa-CDA and were used as the basis for simulation parameters for nanoring arrays.

3.5.2 Discrete Dipole Approximation

The DDA is a frequency domain method that approximates the induced polarization in an arbitrarily shaped NP by calculating the EM response of polarizable dipoles on a rectangular lattice.[91] DDA development is attributed to Purcell and Pennypacker in their study of interstellar grains.[99] Further development of the model, including the production of a freely distributed DDA program, known as DDSCAT, were performed by Draine and Flatau.[100–102] The ability to simulate periodic NP structures was recently added as well as support for new data visualization software. The ability to perform periodic array calculations for arbitrary NP shapes while still retaining some of the computational time benefits of the dipole approximation were reasons that DDSCAT was used for this work. DDSCAT v7.1 and v7.2.2 were both used for simulations reported herein.

3.6 Comparison of Simulation Methods

It is not the objective of this research to compare the numerical results of one method to another. Several simulation methods have been used to illustrate the effects of underlying assumptions as they relate to this work, especially the interaction between particles which is absent in Mie theory simulations. However, for those who are interested in a detailed

comparison of different simulation methods, several have been performed and published in the literature.[36,91,103]

CHAPTER 4

DIFFRACTIVE COUPLING: SENSING APPLICATIONS

4.1 MOTIVATIONS FOR DIFFRACTIVE COUPLING SENSORS

LSPR sensor characteristics depend on NP size and shape,[25,39–42,67] elemental composition,[43–46] spatial NP arrangement,[49,104] and inter-particle separation.[32,40,50–52] NPs in LSPR sensors benefit from large optical cross sections coupled with geometric confinement of absorbed EM, resulting in significant local field enhancements within 5-15 nm of the metal–dielectric interface.[33] Current LSPR sensors rely solely upon this near field enhancement since plasmon modes decay exponentially away from the NP surface. As NPs approach each other, these fields interact, resulting in an enhanced EM field.[55] These order of magnitude field enhancements form the basis for surface enhanced Raman scattering (SERS).[24,39,105] These near field enhancements have been heavily studied for their sensing capabilities.[26,106–109] A key limitation of common LSPR and SPP sensors, including SERS sensors, is that they are limited to detection within the decay length region of the surface plasmon from the metal–dielectric interface. This decay length is 200-300 nm for SPP sensors and 5-15 nm for LSPR devices.[32]

Detection limitations resulting from the near field range limitations can be augmented by far field coupling between NPs in ordered arrays. Far field coupling occurs at inter-particle spacings approaching the LSPR wavelength.[32] Far field coupling is dependent on EM interactions resulting from waves scattered from adjacent NPs with inter-particle spacings at or near the wavelength of interest. When the phase of the scattered EM waves coincides, coupling occurs.[32,110] This coupling is not unique to ordered NP arrays. However, for random structures, the constructive interference is negated by destructive interference caused by scattered EM waves that are out of phase. The result of this constructive interference can result in an increase

in the local EM field incident on a NP due to the contributions from the constructive interference from other NPs in the array in addition to the EM field due to incident light.[62,90] This contribution is calculated for CDA methods using EQ 3-1. Because the nature of this coupling relies on the interactions of incident EM with other NPs, this constructive interference between particles is considered diffractive coupling. Diffractive coupling results in a narrow, high intensity extinction peak in the NP system's spectra. Diffractive coupling peaks differ from typical plasmon peaks because their position is predominately determined by the structural configuration of the sensor and its interactions with properties of the incident EM field (*e.g.* polarization, wavelength) not the NP size and shape.

Diffractive coupling in NP arrays is best observed by arranging similarly-sized, LSPR active NPs into regular, periodic arrays which have been designed to maximize the constructive interference between NPs at a desired wavelength. This phenomenon was first reported in NP arrays in 2005.[59] An important observation with diffractive coupling is that this coupling and its associated spectral response are distinct from the local field enhancements seen in typical LSPR devices.[60,61,111] The spectral response associated with this coupling will still be affected by changes in the local dielectric around individual NPs since it is dependent upon interactions of EM waves scattered from adjacent NPs. Potential advantages of diffractive coupling based sensors relative to current LSPR sensors include improvements in sensitivity, multi-spectral analysis, far field analyte interrogation, and reduced peak broadening from inhomogeneity in NPs. Multi-spectral analysis is possible because the diffractive peak occurs separately from the LSPR peak, allowing detection even if one of the spectral features is obfuscated by the analyte. Diffractive sensors inherently probe the region between NPs, decreasing the diffusive resistance of the analyte to the sensing region.[32] Research has shown that this coupling spectral feature is

less affected by deviations in NP shape and size than the LSPR spectral feature.[112] This increases the robustness of the resulting sensor to defects resulting from fabrication.

This chapter outlines experimental sensing results for two different diffractive coupling sensors and compares the sensitivity of these sensors to random NP sensors. A single sensing system, described in 2.4.2, was used to directly compare random and ordered NP sensors while mitigating effects of external factors on sensitivity including spectrometer spot size, sample orientation, and focal length. In addition to demonstrating diffractive coupled sensing, an increased sensitivity of the LSPR peak in ordered arrays was also observed. These experimental results are then compared to theoretical results.

4.2 DIFFRACTIVE COUPLING SENSOR

Diffractive coupling sensors were fabricated as outlined in 2.3.1. Fabrication parameters were selected based on numerical modeling (CDA) for spherical arrays of interacting NPs. Two specific diffractive coupling sensors will be reported on this chapter. The first consists of cylindrical disk shaped gold NPs created with typical fabrication methods, *i.e.* sputtering. The second consists of spheroidal gold NPs created with EL plating combined with thermal annealing. Sensing characteristics were evaluated at ambient conditions. Diffractive coupling sensor performance was directly compared to sensing performance of random NPs fabricated using EL plating and thermal annealing.

4.2.1 PHYSICAL CHARACTERIZATION

Plasmonic based sensors are strongly affected by NP size,[2,39–41] shape,[2,25,39,42] arrangement,[49] and inter-particle separation.[32,40,50–52] These dependencies require a careful analysis of fabricated sensor parameters to establish good correlation between experimental

observations and theoretical simulations. Four specific sensing arrangements were tested: larger, less dense random NPs (Random Spot 1); smaller, higher density random NPs (Random Spot 2); a cylindrical disk sputtered NP array (Sputtered Ordered), and a spheroidal EL plated ordered NP array (EL Ordered). The Sputtered Ordered sensor consisted of a 5 x 5 array of 100.5 µm x 100.5 µm square arrays of filled circles with a target horizontal and vertical spacing of 670 nm (total size 502.5 µm x 502.5 µm). The EL Ordered sensor consisted of a 1x10 array of the same 100.5 µm x 100.5 µm square arrays with the same target spacing. Physical characterization of the plated sensors was performed with SEM images analyzed with Matlab, as described in 2.4.1. Representative SEM images for each sensor are shown in Figure 4.1. Random Spot 1 (Figure 4.1 A) had a broad particle diameter distribution of 50. ± 21 nm and an average particle density of 8.04 x 10^9 NP/cm^2 based on measurements from 909 NPs. Random Spot 2 (Figure 4.1 B) consisted of NPs with a particle diameter distribution of 39. ± 14 nm with an average particle density of 1.90 x 10^{10} NP/cm^2 (N= 2096 NPs). The Sputtered Ordered sensor particle diameter distribution was 208 ± 10 nm (N=20 NPs) with an average particle density of 2.37 x 10^8 NP/cm^2 (N=104 NPs). The EL Ordered sensor particle diameter distribution was 161. ± 6 nm with an average particle density of 2.52 x 10^8 NP/cm^2 (N=226). Particle density for the random sensors was calculated from the area of the SEM image analyzed. Ordered sensors utilized the average inter-particle spacing to calculate the particle density based on a unit cell of the array. Average inter-particle spacings for the random sensors were determined from the particle density assuming the particles were on a square lattice. Inter-particle spacings for ordered arrays were calculated based on the distances to adjacent NPs in cardinal directions. Average inter-particle spacings were 111, 72, 649, and 630 nm for Random Spot 1, Random Spot 2, Sputtered Ordered, and EL Ordered, respectively. Comparison of the two ordered arrays shows a particle diameter

decrease of 22% for the EL Ordered sensor and an inter-particle spacing decrease of 2.9%. These values will be important when comparing the spectral response of the diffractive coupling spectral features.

4.2.2 SPECTRAL CHARACTERIZATION

Spectral measurements for sensitivity analysis were performed using the spectrometer setup shown in Figure 2.3. The spectral response of Random Spot 1 and the EL Ordered sensor in air were also recorded using the microscope spectrometer with a 200 µm slit width and full vertical binning. This results in spectral collection from an area of ~1 x 60 µm. A change in the spectral collection area affects the number of NP whose components combine to produce the observed spectra. Local variations in NP size distribution for the random sample result in shifts in the spectra. Spectral results for both sensors, shown in Figure 4.2, are slightly different in peak location than those from the first micro-spectrometer because the spectra represent a much smaller area of the sample. The illuminated spot size for the microscope spectrometer system is much smaller (0.0625 mm^2), which affects the number of NP involved in diffractive coupling. The random NP sample has a large variation across the surface in particle density and size. Without a micropositioner on the microscope, it is very difficult to take spectra from the same region as Random Spot 1 on the random sample, because the NPs are too small to be observed in the optical microscope. Additionally, the same effect caused by the reduced spectral collection area will be apparent in the random spectra. Sensor sensitivity was evaluated using the micro-spectrometer with micropositioner, as previously mentioned.

Maximum peak intensity between the four sensors is quite different. This intensity difference in the measured extinction spectra is easily related to the NP number density.

Dependence of the experimental extinction on NP number density can be clearly illustrated by examining the experimental and Mie theory simulation results for Random Spots 1 and 2. Mie theory simulations for Random Spot 1 resulted in peak extinction efficiency 42% larger than Random Spot 2. This difference is easily attributed to the larger scattering cross section for NPs in Random Spot 1. Experimentally, however, the peak extinction was 54% lower for Random Spot 1 than Random Spot 2. When NP number density is taken into account in the Mie theory results, the peak extinction is 66% lower. This dependence on NP number density is expected since experimental data is the result of all of the NPs in the spectral FOV whereas Mie theory is based on a single NP.

Random NP sensors exhibit a single peak that is characteristic of the LSPR response of gold. Multiple peaks are apparent in the ordered arrays. The Sputtered Ordered sample does not have a discernible LSPR peak. This sensor had small gold NPs (~15 nm) in the background of the NP array (see Figure 4.1 D). The reference spectrum was taken from a region containing these much smaller particles far away from the array which removed the spectral response of these small particles. This removal, combined with noise from the system, made the LSPR peak indistinguishable. The EL Ordered sample does exhibit a peak in this wavelength range (400-600 nm). In addition to this peak in the LSPR range, ordered NP arrays exhibit peaks in the region from 650-900 nm. These peaks are related to diffractive coupling. The first of these peaks is approximately at a wavelength equal to the inter-particle spacing. Currently, the source of other peaks in this region is not known. Several reports of additional peaks in diffractive coupling arrays exist which attribute the multiple peaks to waveguide modes in the ITO layer.[110,113] Unfortunately, these modes are not supported in air for an ITO thickness of less than

50 nm.[114] However, several observations have been made that should aid future researchers to determine the source of these peaks.

First, peaks show a strong dependence on the incident angle. Figure 4.3 shows the change in peak location for the EL Ordered sample in air as the sample is tilted from the plane orthogonal to the direction of light propagation. Tilting the sample in this fashion changes the phase of light that is incident on each NP along the tilted sensor, which in turn changes the wavelength where constructive interference will occur. Analysis of the peaks' shift with the change in angle indicates that the peaks are shifting symmetrically about a specific wavelength. Similar peak shifts are observed in the Sputtered Ordered sensor.

Second, strong polarization dependence is observed for ordered sensors. This polarization dependence is expected for diffractive coupling because the EM field excited around a particle is orthogonal to the linear polarization direction. For square arrays, when the polarization is parallel with a lattice direction, the EM field between particles will be orthogonal to the polarization. Figure 4.4 shows the change in the first (top) and second (blue circles, bottom) peaks in the diffractive coupling region for the Sputtered Ordered sample. For the first diffractive peak, polarization changes appear to change peak position in a sinusoidal fashion, but the peak shift for the main diffractive peak is larger at 230° than near 0° and the apparent maximum and minimum wavelengths do not appear to have a single period. Figure 4.4 also shows how the first two peaks in the diffractive coupling region vary with respect to each other. The second peak appears to be more sensitive to polarization changes in terms of both peak shift amplitude and frequency. The same polarization experiment was performed on a random NP sensor, but no polarization dependence was observed. The random arrangement of the NPs in a

random sensor results in both constructive and destructive interference as the polarization changes, resulting in no net change in the spectral signal. Polarization dependence has been previously observed in ordered nanoparticle arrays, but is normally attributed to particle shape non-uniformity.[115] However, the trend observed for the Sputtered Ordered sensor has been observed in several other diffractive coupling sensors with very different NP shapes (cylindrical disks, spheroids, and hemispheres). One parameter that is consistent between arrays that exhibit this polarization dependence is that the inter-particle distance in the horizontal direction is slightly larger than in the vertical direction. These differences in spacing in the vertical and horizontal grating direction have been shown to cause multiple peaks in diffractive coupling arrays.[110,113] For the Sputtered Ordered sensor, the horizontal inter-particle spacing is 658 nm while the vertical inter-particle spacing is only 634 nm, a difference of 3% from the horizontal spacing. This is compared to average peak locations of 721 and 701 nm, a difference of 3%. While there appears to be correlation, additional research is needed to determine the exact source of the multiple peaks. Another possible explanation is that one of the peaks is the result of coupling of non-axial particles. The nature of diffractive coupling would predict these peak locations to be located at some harmonic of the inter-particle spacing. A comparison of the harmonics for the five closest NPs did not match the experimental peak positions. Further work is needed to determine if interactions between coupling axial and non-axial NPs exist.

Finally, a broad peak is seen for both ordered sensors in the near infrared (NIR) range of 800-900 nm. The source of this peak is believed to be related to the ITO layer on the sensor substrate surface. For all of the experimental data reported here, the intensity of the light source in this region is low, resulting in a large amount of noise. This noise made it difficult to perform a sensitivity analysis of sensing performance for this peak. Further work is necessary to

correctly identify the source(s) of these peaks, although from this preliminary analysis they appear to be related to the diffraction phenomenon and not particle size as similar peaks are observed for both ordered sensors.

Spectral analysis of experimental data relied on a modified smoothing algorithm to remove noise from the signal. Smoothed and original spectra were compared after peak finding to verify accuracy. Average peak wavelengths in air for Random Spot 1, Random Spot 2, Sputtered Ordered, and EL Ordered are: 527.6 nm; 528.5 nm; 700.6 and 860.9 nm; and 525.2, 665.7, 752.8, and 785.6 nm, respectively. The Sputtered Ordered sensor did show a peak in some spectra during sensing experiments at ~730 nm, but the peak was not discernible in spectra for all RI fluids. Standard deviations for sensor response in each RI environment are based on at least three repetitions of the experiment.

4.3 Evaluation of Sensor Performance

Sensor performance for Random Spot 1, Random Spot 2, Sputtered Ordered, and EL Ordered sensors were evaluated in response to a range of RI fluids. Seven different values of RI were used to evaluate sensor performance: air (1.00), methanol (1.328), water (1.333), acetone (1.359), ethanol (1.361), isopropanol (1.3772), and toluene (1.479).[82] Figure 4.6 shows each of the sensors' experimental spectral response for the change from air (blue) to water (green). Peak wavelengths for each spectra were identified with the aforementioned Matlab programs. Each peak location is based on the average of peak position recorded over at least 3 experimental runs. Peak locations in each of the RI fluids are reported in Table 4.1.

NP characteristics determined in 4.2.1 were used to perform simulations based on Mie theory and rsa-CDA. Mie theory simulations used an effective RI based on the published

effective dielectric ratio reported in 3.2. The experimentally determined weighting factors were used for rsa-CDA simulations. Mie theory simulations for Random Spots 1 and 2 predict a dipole mode near 520 nm. Experimental results for Random Spots 1 and 2 were slightly red shifted in air and showed a lower sensitivity to changes in RI relative to Mie theory simulations. This difference could be partially a result of the weighting factor used to approximate the effective RI, since when the experimentally determined weighting value used with rsa-CDA simulations is applied, simulated peak positions are red-shifted.

In ordered samples with larger NPs, dipoles red shift and broaden, and a quadrupole mode appears for the Sputtered Ordered sensor. For the EL Ordered sensor, only a dipole mode is predicted in air; however, a quadrupole mode appears as RI transitions to larger simulated values. Because Mie theory only predicts the response of individual NPs, Mie simulation results for the EL Ordered and Sputtered Ordered sensors should be compared to the plasmon peak and not the diffractive peaks. Ordered arrays of nanospheres, as mentioned in Chapter 3 are not accurately modeled by Mie theory because it neglects particle interactions. These interactions are accounted for in the CDA, DDA, and FDTD methods. Simulations with rsa-CDA assumed an effective RI in air that was a weighted average of the air and substrate, with 55% of the effective RI being from the substrate/ITO and 45% from the medium RI. These weighing factors were determined by fitting the peak position determined experimentally for Random Spot 1 in air. The same weighting values were used for all of the CDA simulations for each sensor. DDA and FDTD results were also performed on the ordered cylinder sample to compare the different simulation methods. Figure 4.5(A-C) compare simulation data from Mie theory, DDA, and FDTD for the Sputtered Ordered array. CDA simulations (not shown) result in comparable medium wavelength shifts as predicted by DDA. FDTD simulations were performed with

vacuum wavelengths. FDTD simulations for medium wavelength would be desirable for comparison, but were not available as the person who did the FDTD simulations was no longer available. A detailed analysis of this sensor comparing the sensitivity of these simulation methods is available in the literature.[90] Random Spots 1 and 2 show good correlation between experimental spectra and Mie theory simulations. Experimental peaks are red shifted and peak broadening is apparent relative to the corresponding Mie theory. Similar effects have been attributed to deviations from spherical NP shape, substrate effects, and near field NP-NP interactions which are not included in Mie analysis.[93,116]

The Sputtered Ordered sensor spectra do not show a discernible plasmon peak. Figure 4.1 D shows a film of small gold NPs in the background, which was present on the entire sensor substrate and was subtracted from the spectral signal as part of the reference spectra. This removal appears to have affected the detection of the NP plasmon peak for the larger particles. However, a plasmon peak is observed for the EL Ordered sensor. Comparison between the experimental plasmon peaks in Table 4.1 to peak locations predicted by Mie theory show the experimental data blue shifted relative to Mie simulation results. This result is unusual if Mie theory accurately represents the data because common sources of variation between simulation and experiment, such as substrate effects, typically result in red shifts. Models that allow the NPs to interact have shown plasmon blue shifts when the array exhibits diffractive coupling. The LSPR blue-shift can be attributed in part to far field NP-NP interactions and is observed in simulations which account for coupling.[90] Organizing NPs into arrays results in phase interference between NPs, as quantified in the retarded dipole sum.[62] Inter-particle distances larger than the resonance wavelength exhibit constructive interference at wavelengths near the

lattice constant, but destructively interfere at the plasmon frequency. When this interference is destructive, the restoring force is enhanced, causing a blue-shift in the plasmon frequency.

Results from rsa-CDA show excellent agreement with the experimental plasmon peak location when no weighting factor is applied. Figure 4.7 directly compares experimental spectra (solid) and rsa-CDA (dashed) in air (blue) and water (green). The good correlation between plasmon wavelengths is easily observed when the spectra are vertically shifted and scaled to coincide (inset). Both the dipole and quadrupole modes that are expected for NPs of this size appear to be in agreement. The diffractive coupling peak is red shifted, broadened, and less intense than predicted by rsa-CDA. These differences from simulation to experimental data are consistent with those caused by NP size and shape variations as well as the previously mentioned variations measured for inter-particle spacing. When the experimental weighting factor is applied, the diffractive peak representing the air data coincides with experiment, but the predicted shift is smaller than observed in experiments.

Experimental sensitivities were determined for each sensor and compared to simulation sensitivities calculated from Mie theory and rsa-CDA simulations and are available in Table 4.2. Theoretical sensitivities for CDA and Mie theory are calculated from the RI change in air, methanol, water, acetone, ethanol, isopropanol, and toluene. Sensitivity response of plasmonic sensors has been shown to be linear which suggests that these different RI ranges for the different simulations should be directly comparable.[67] However, Mie theory simulations performed as part of this work show an increased sensitivity when the peak position in air is not included in the sensitivity calculation. Values for plasmon sensitivities in air between rsa-CDA and experimental data show better correlation than those predicted by Mie theory. rsa-CDA

sensitivities have less change in sensitivity between air based and methanol based sensitivities. Since the experimental data do not follow this trend, further work is needed to determine the linear range of RI sensitivity for diffractive sensors.

Figure 4.8 shows Mie theory (hollow) and experimental (filled) sensitivities for peaks observed in Figure 4.6 for Random Spot 1 (filled blue diamond, 536 nm), Random Spot 2 (filled green circle, 535 nm), EL Ordered (filled red triangles, 541,681,766 nm), and Sputtered Ordered (filled cyan square, 709 nm). Peak wavelength in methanol is listed next to each respective point as an identifier. Pointers correspond to those found in Figure 4.6 to aid in identification of peak–sensitivity correspondence. Sensitivity of the dipole peak for Random Spot 1 (536 nm) and Random Spot 2 (535 nm) are slightly lower than predicted, which is attributable to deviations from NP shape ideality in the experimental sample. On the other hand, sensitivity of the plasmon peak (541 nm) from the EL ordered array is 41% higher (198.6 nm RIU^{-1}) than predicted by Mie theory for a similar wavelength plasmon peak(140.7 nm RIU^{-1}, 544 nm). Diffractive coupling in the array resulted in a blue-shift of the LSPR due to a decreased effective polarizability. A change in the RI surrounding the array results in a non-linear change in the retarded dipole sum for a particular particle size. This non-linearity results in higher plasmon sensitivity in diffractive coupling arrays.

Experimental results indicate that diffractive coupling sensitivity is higher than LSPR sensitivity when sensitivity is calculated with respect to air. For the EL Ordered sensor, rsa-CDA predicts that the plasmon will be more sensitive than a single NP plasmon of the same wavelength. Experimental values of sensitivity for diffractive coupling sensors are in fair agreement with theoretical simulations. The Sputtered Ordered sample was also simulated with

DDA and resulted in a similar sensitivity (41 nm/RIU vs. 38 nm/RIU experimentally).[90] These simulations were performed with the wavelength in the RI of the analyte . Results from FDTD were performed with vacuum wavelengths yielded a sensitivity for the Sputtered Ordered sensor of 276 nm/RIU.[90] Work is ongoing to methodically determine what values of particle size (dipole vs. quadrupole), shape (rounded cylinders versus spheres), substrate, and pattern alignment between 100.5μm x100.5 μm array elements will yield experimental sensitivities similar to those predicted by FDTD.

An important aspect of chemical sensors, especially those made of precious metals, is the amount of material required for sensing. Sensitivities which have been adjusted to account for the fractional area of the sensor surface that is covered with NPs are determined with EQ 2-5. Experimental values for methanol based NP sensitivity for Random Spot 1, Random Spot 2, EL Ordered, and Sputtered Ordered samples are 393, 274, 3511, and 1088 nm/RIU, respectively. These values for diffractive sensors are ~10 times those of random NP sensors. Further work is needed to determine if this increase in sensitivity is solely due to the increase in particle size or if it is related to the diffractive coupling in the array.

FOM values for the diffractive peak with methanol sensitivities are 2.1, 0.9, 2.3, and 1.7 for EL Ordered experimental, Sputtered Ordered experimental, EL Ordered rsa-CDA, and Sputtered Ordered rsa-CDA, respectively. Theoretical work on diffractive coupling suggests ideal samples would exhibit a diffractive coupled feature with a very narrow FWHM (as shown in Figure 4.5 D).[62,90] These narrow FWHM values have recently been confirmed experimentally for cylindrical NPs.[117] A narrow FWHM is important for low concentration chemical sensing where minute RI changes occur because it is difficult to determine the exact peak location for

broad features, such as those predicted by Mie theory for large particles, without sophisticated data analysis algorithms and higher resolution spectrometers.[118]

4.4 SENSOR RELIABILITY

Ordered nanoparticle arrays fabricated with EL plating demonstrated a uniform response with no hysteresis for all of the experimental runs performed. Several hundred RI sensing experiments were performed, resulting in consistent peak shifts. The spheroid sample was tested in water shortly after fabrication. The average response to water two years later was identical. It should be noted that gold NPs are degraded in certain sensing environments (*e.g.* hydrogen sulfide) due to chemical reactions with the gold NP.[14] The effect of these reactions on sensor lifetime is unclear since detection of an analyte is based on the difference of the sensor in the presence and absence of analyte, thus accounting for the initial state of the NPs. The sensors are, however, prone to physical damage. The gold NPs are easily damaged by inadvertent contact with handling devices such as tweezers. In a commercial sensor design, the sensor could be easily protected against physical damage of this kind.

4.5 CONCLUSIONS

Diffractive sensing was demonstrated for the first time with sensors consisting of nanocylinders and nanospheres. Aggregate sensitivity was comparable to sensitivity values for current random LSPR sensors with spherical NPs both in the same experimental system and reported in the literature. When the area and number of NPs are factored into the sensitivity, diffractive based sensors have a significant advantage over similarly shaped NPs in random configurations. FOM values were comparable between experimental and rsa-CDA simulations for the sensors evaluated. Theoretical simulations with improved diffractive coupling peak

intensity and narrower FWHM than for the fabricated sensors were demonstrated for 150 nm diameter particles with and inter-particle spacing of 670 nm.

TABLE 4.1: Experimental and Mie theory peak locations for changes in refractive index. Gray regions represent where no data is available

Experimental		Air	Methanol	Water	Acetone	Ethanol	Isopropanol	Toluene
Refractive Index		1	1.328	1.333	1.359	1.361	1.377	1.497
Random Spot 1		527.6 ± 0.7	534.5 ± 0.6	533.6 ± 0.3	536.4 ± 1.7	536.3 ± 0.5	537.3 ± 0.6	541.8 ± 0.6
Random Spot 2		528.5 ± 0.6	536.4 ± 1.1	536.5 ± 0.6	536.9 ± 1.6	536.3 ± 0.4	537.7 ± 1.3	543.4 ± 3.3
EL Ordered	LSPR	525.2 ± 2.4	540.7 ± 0.8	539.5 ± 3.0	549.5 ± 5.0	546.8 ± 2.1	545.9 ± 2.1	
	Peak 1	665.7 ± 1.8	680.8 ± 4.3	686.3 ± 2.1	686.9 ± 1.7	686.5 ± 2.3	690.8 ± 0.9	
	Peak 2	752.8 ± 0.4	765.9 ± 0.4	766.0 ± 0.4	766.9 ± 0.4	767.5 ± 0.3	768.3 ± 0.2	
	Peak 3	785.6 ± 1.4	808.1 ± 1.4	809.6 ± 1.8	809.5 ± 1.8	809.1 ± 0.7	810.7 ± 0.4	
Sputtered Ordered	Peak 1	700.6 ± 1.3	709.4 ± 1.6	710.1 ± 1.6		711.9 ± 1.7	713.1 ± 2.7	
	Peak 2	860.9 ± 4.8	891.9 ± 10.7	883.9 ± 1.4		892.9 ± 8.0	895.1 ± 5.7	

Mie Theory		Air	Methanol	Water	Acetone	Ethanol	Isopropanol	Toluene
Refractive Index		1	1.328	1.333	1.359	1.361	1.377	1.497
Effective refractive index		1.083	1.351	1.356	1.377	1.379	1.392	1.475
Random Spot 1		516.2	533.9	534.2	535.9	536.1	537.2	545.6
Random Spot 2		513.8	529.6	529.9	531.4	531.4	532.5	539.3
EL Ordered	Quadrupole		544.4	544.6	547.2	547.2	549.2	561.5
	Dipole	577.3	666.6	668.1	676.0	676.6	681.7	718.0
Sputtered Ordered	Quadrupole	530.1	571.8	572.6	577.0	577.4	580.1	597.9
	Dipole	651.3	803.3	805.8	818.2	819.1	826.9	877.2

TABLE 4.2: Experimental and simulated values for sensitivity. Mie theory and rsa-CDA use different effective medium values.

Experimental		**Air based Sensitivity**			**Methanol based sensitivity**			**Average particle size**		
Spot 1		33.3	±	5.0	62.1	±	6.2	50	±	21
Spot 2		33.9	±	4.6	59.2	±	7.3	38	±	14
	LSPR	69.0	±	12.8	198.6	±	87.9			
EL ordered	**Peak 1**	73.1	±	9.8	180.1	±	63.3	161	±	6
	Peak 2	58.6	±	1.0	58.6	±	7.5			
Sputtered ordered	**Peak 1**	37.7	±	3.8	88.5	±	5.2	209	±	5
Mie Theory		**Air based Sensitivity**			**Methanol based sensitivity**			**Average particle size**		
Spot 1		71.6	±	3.9	95.4	±	2.4	50	±	21
Spot 2		62.7	±	2.6	78.8	±	1.6	38	±	14
EL ordered	**Quadrupole**		N/A		140.7	±	4.3	161	±	6
	Dipole	348.5	±	11.3	417.6	±	7.9			
	Quadrupole	167.1	±	7.1	211.2	±	0.9	209	±	5
Sputtered ordered	**Dipole**	571.6	±	4.1	597.1	±	2.4			
rsa-CDA		**Air based Sensitivity**			**Methanol based sensitivity**			**Average particle size**		
Spot 1		53.8	±	4.8	78.2	±	6.1	50.0	±	21.0
Spot 2		78.3	±	8.1	115.4	±	13.8	38.0	±	14.0
EL ordered	**Plasmon**	60.9	±	2.6	52.0	±	6.2	161.0	±	6.0
	Peak 1	48.0	±	2.0	48.0	±	6.0			
Sputtered ordered	**Peak 1**	56.1	±	1.2	62.5	±	1.3	209.0	±	5.0

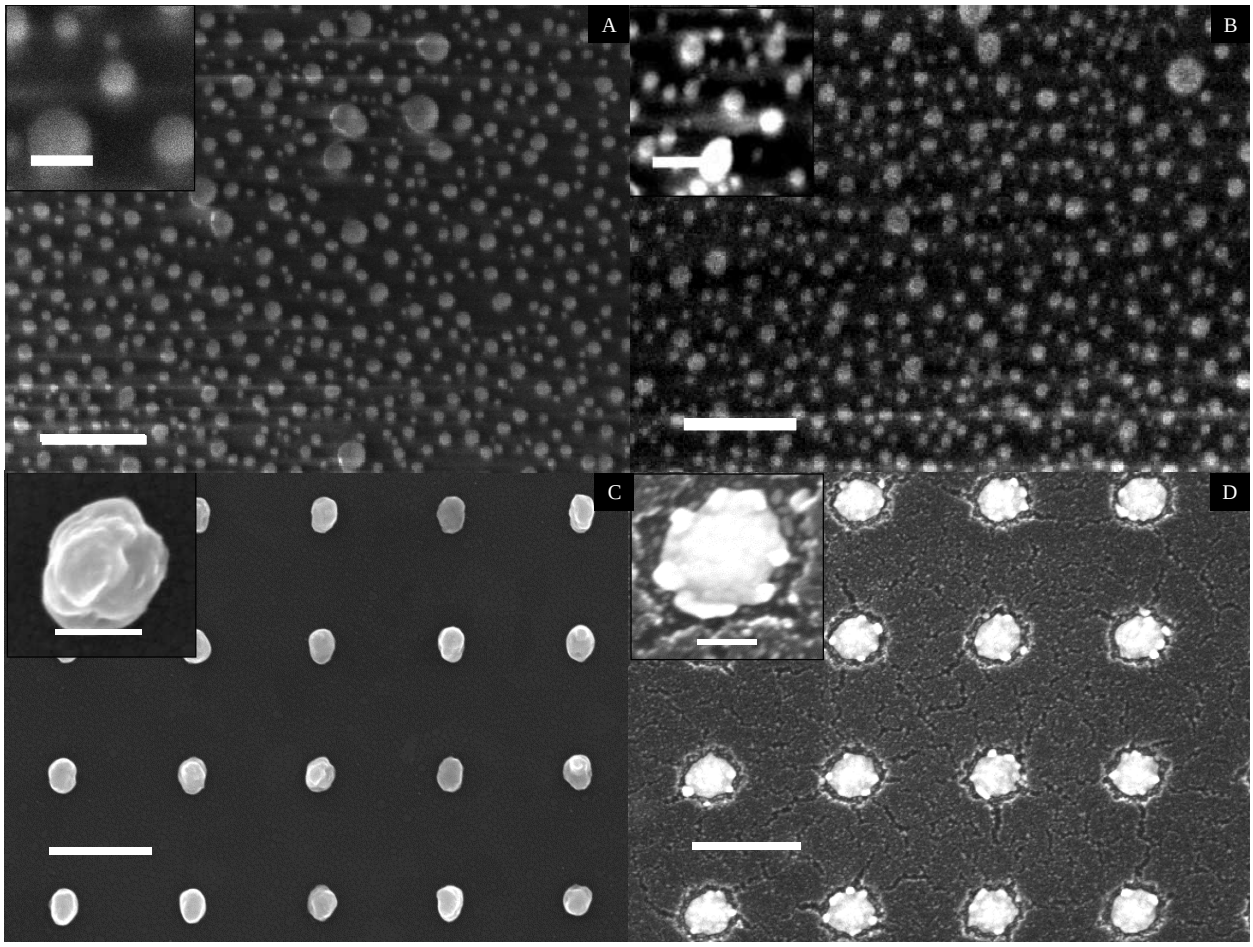

FIGURE 4.1: Representative SEM images of gold nanoparticles for typical LSPR and diffractive coupling sensors. A) Random Spot 1, B) Random Spot 2, C) EL Ordered array, D) Sputtered Ordered array. Main scale bar is 500 nm. Inset scale bar is 100 nm.

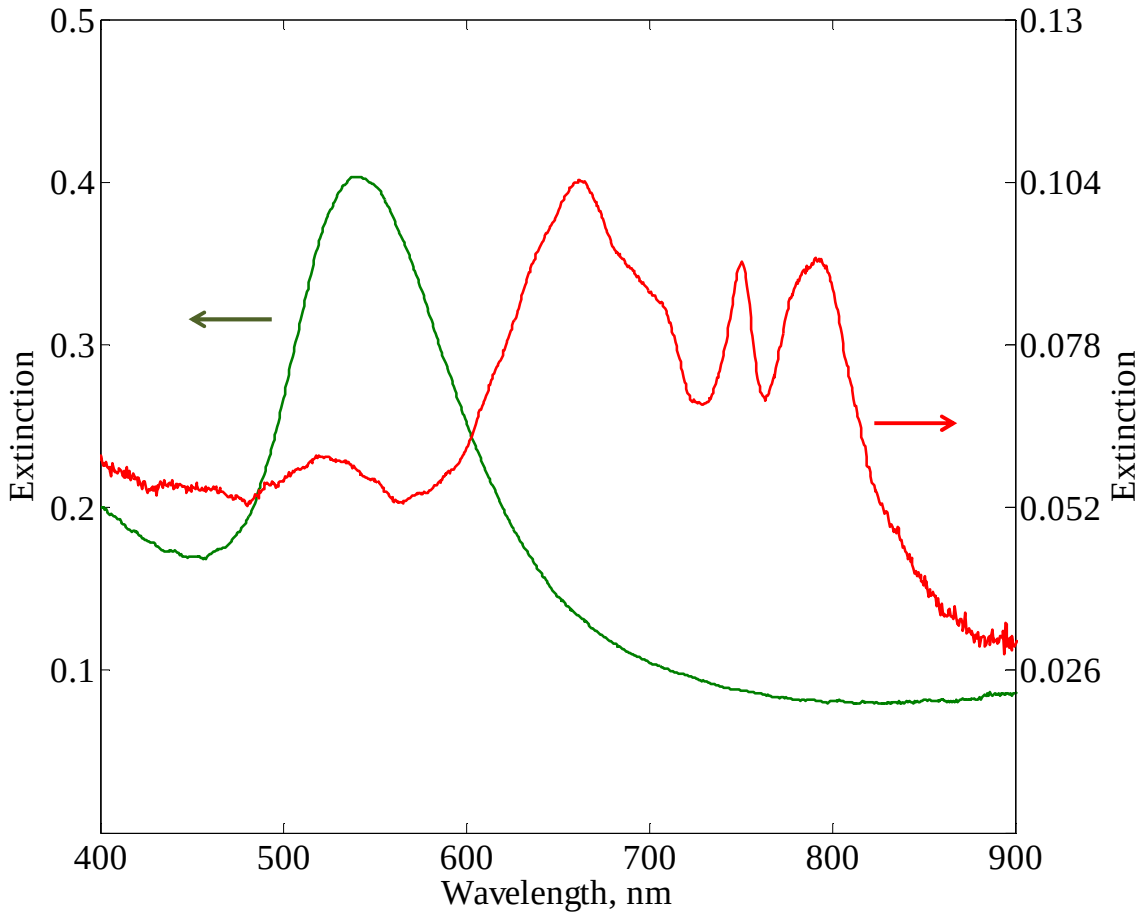

FIGURE 4.2: Spectral measurements taken with microscope spectrometer system. These spectra can be directly compared to spectra B and D in Figure 4.6. Extinction values on the left correspond to the green spectra while values on the right correspond to the red spectra.

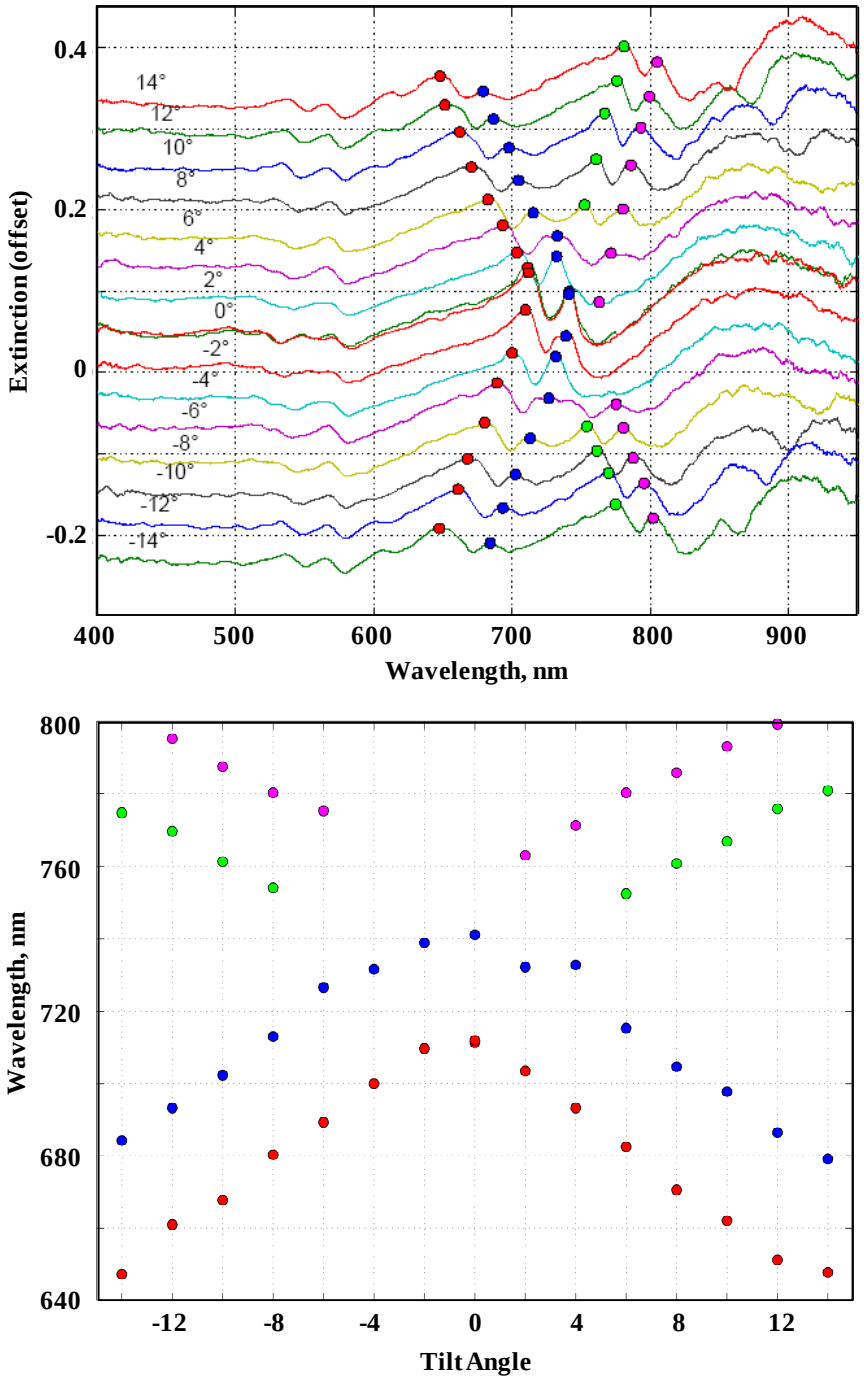

Figure 4.3: Peak shifts caused by changes in the sensor angle relative to incident light for the Sputtered Ordered sensor in air. Angles are reported as the change in angle from an initial position where the sensor is perpendicular to the light source. Bottom plot shows peak locations from above as a function of tilt angle.

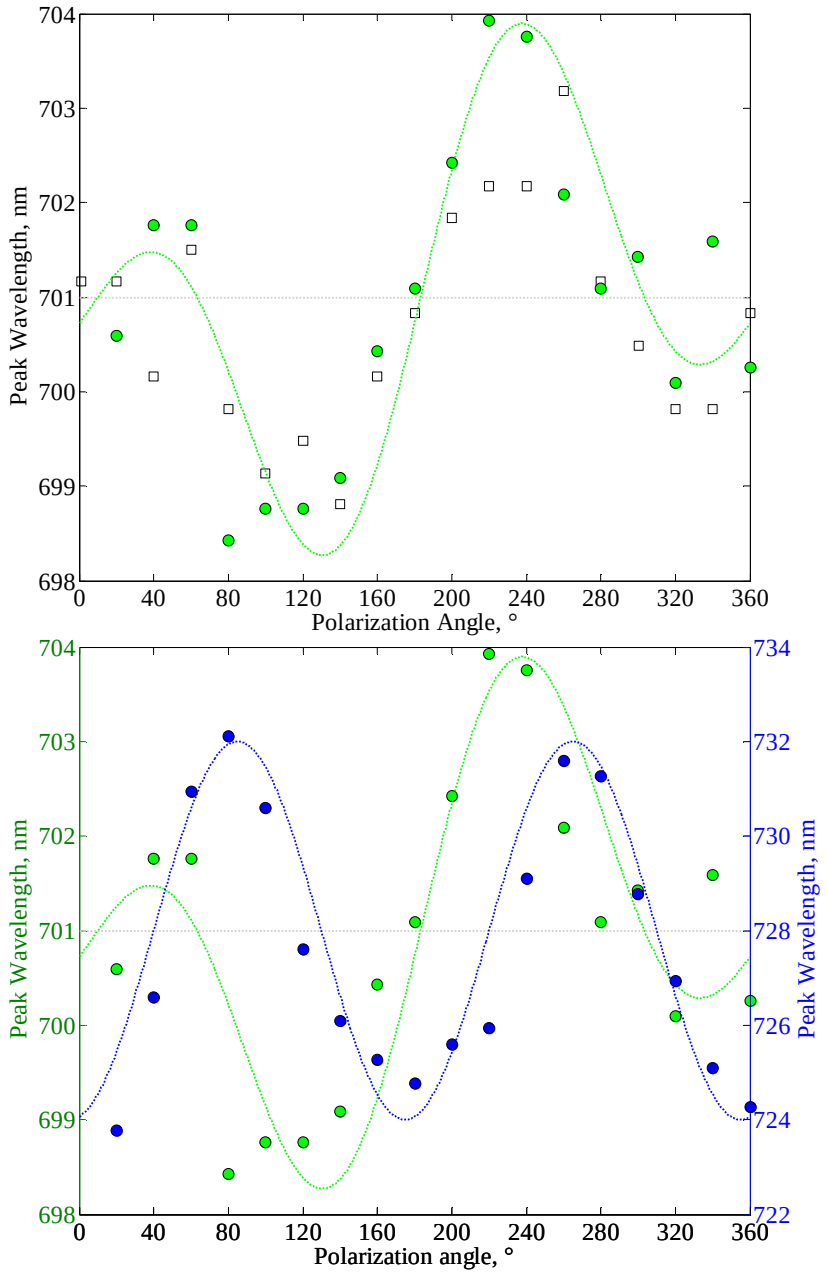

Figure 4.4: Sputtered Ordered sample diffractive coupling peak position as a function of polarization angle relative to the horizontal axis. Top) Squares and circles represent separate measurements of polarization angle dependence on the same sample. Dotted lines are to guide the eye. Bottom) Comparison of amplitude and phase for first two diffractive peaks: 701 (green circles) and 728 (blue circles).

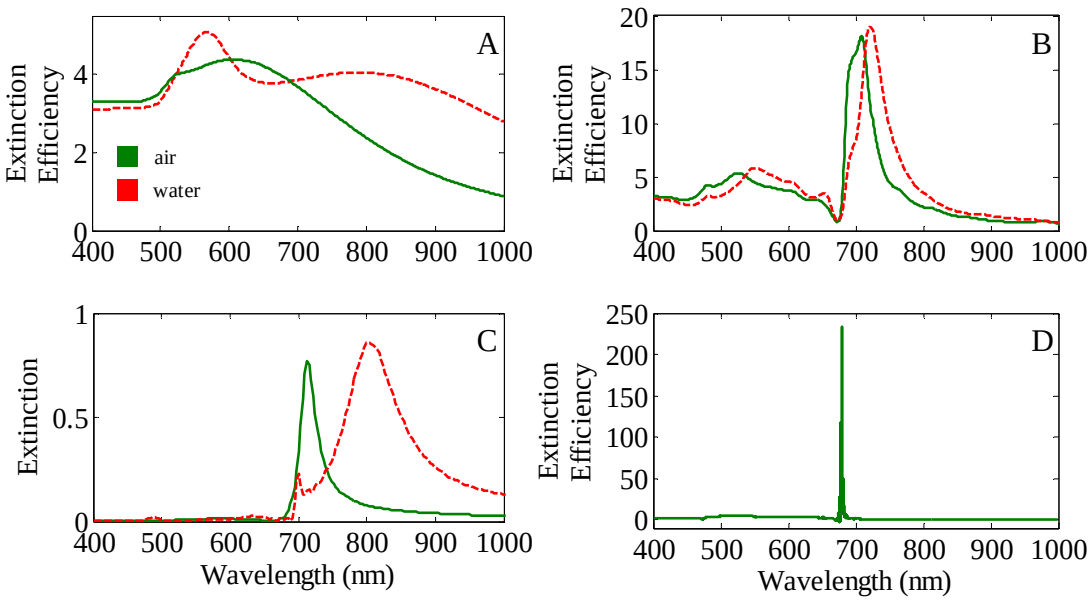

FIGURE 4.5: Spectral simulations for Sputtered Ordered NP array in air (solid green) and water (dashed red) using A) Mie theory, B) DDA, and C) FDTD (vacuum wavelength). Mie theory does not account for inter-particle interactions and does not predict coupling while DDA and FDTD predict a shift of the coupled feature. D) CDA simulations for 150 nm diameter particles with an inter-particle spacing of 670 nm show that for optimized array parameters the extinction efficiency can be significantly increased while reducing the FWHM of the diffractive coupling feature.

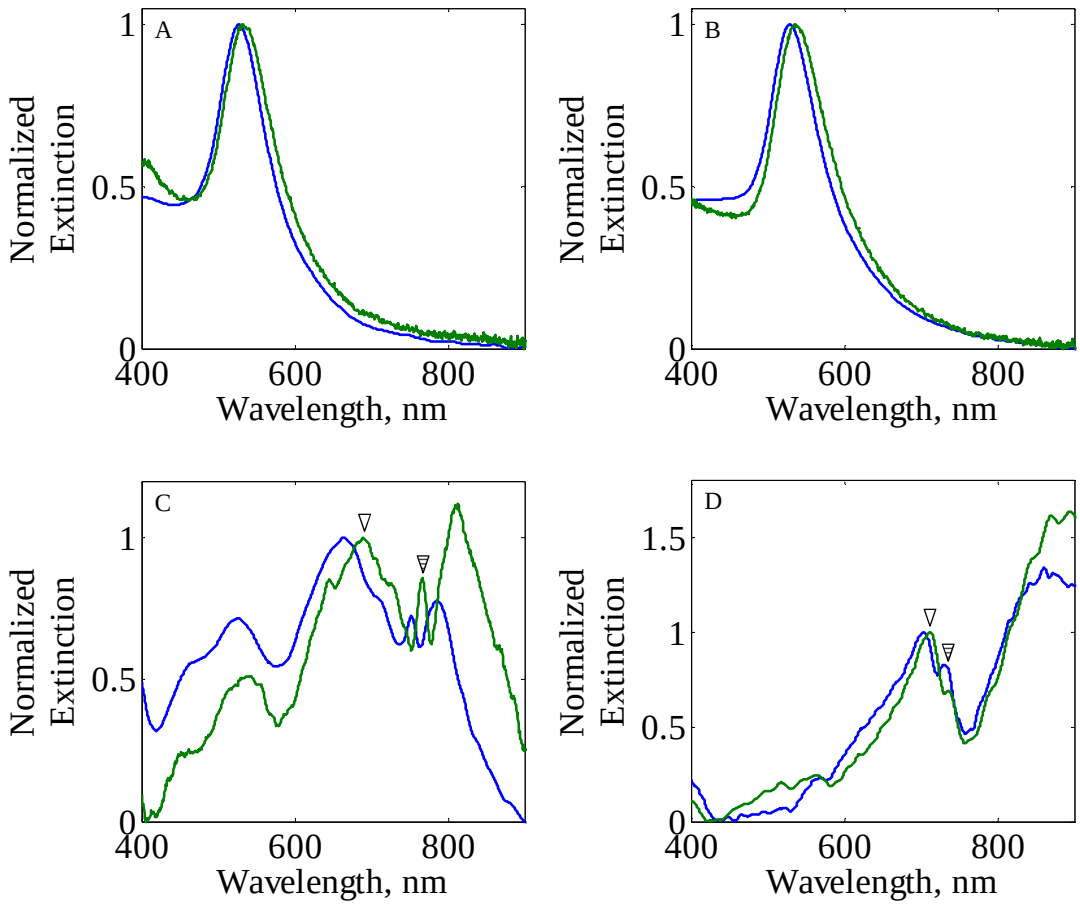

FIGURE 4.6: Experimental UV-Vis spectra in air (blue) and water (green) for A) Random Spot 1, B) Random Spot 2, C) EL Ordered, and D) Sputtered Ordered sensors. Each spectra has been normalized to the main peak used for sensing.

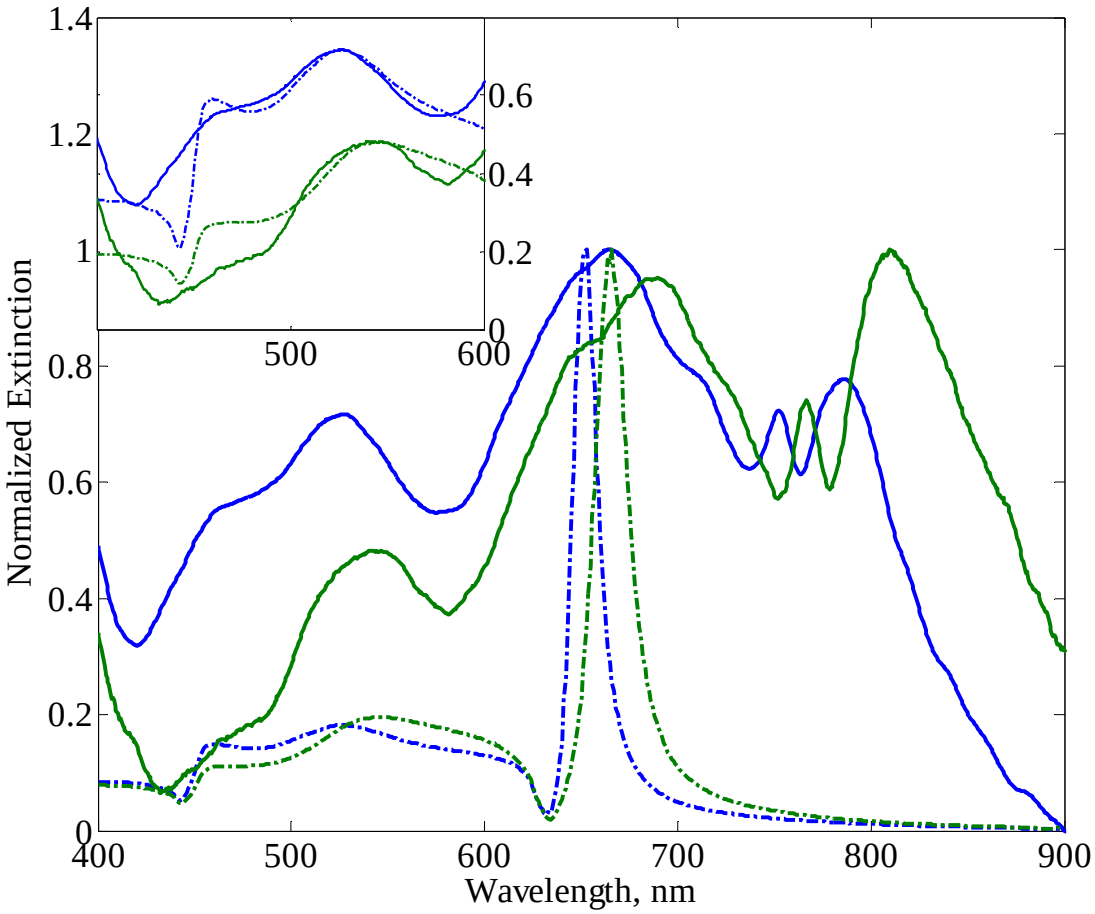

FIGURE 4.7: Normalized experimental (solid) and simulated (dashed), based on CDA) spectral response for EL Ordered sensor exposed to air (blue) and water (green). Inset shows good agreement for the prediction of the plasmon peak features when the CDA model is vertically shifted and scaled to match the plasmon region.

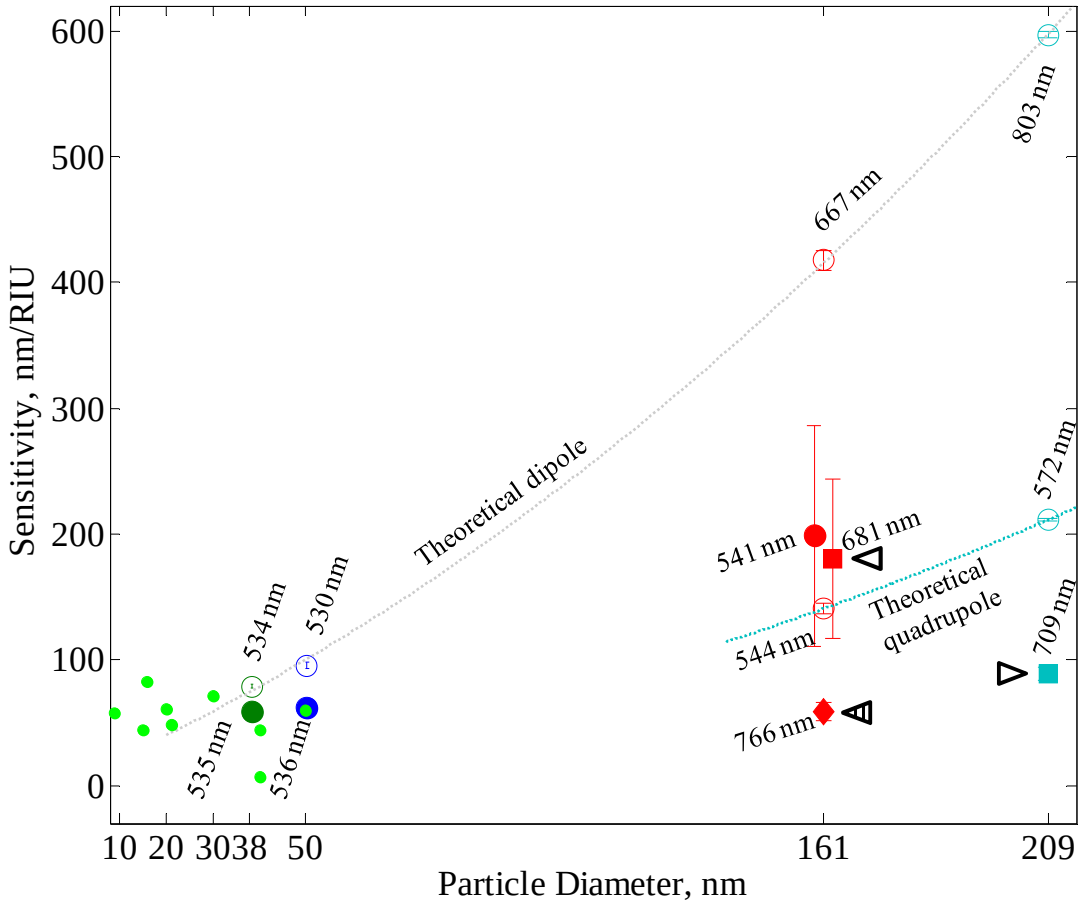

Figure 4.8: Particle size effects on experimental (solid) and Mie theory (hollow) sensitivities based on shifts from methanol peak locations (listed next to each sensitivity): Random Spot 1 (blue diamonds), Random Spot 2 (green circles), Sputtered Ordered (cyan squares), and EL Ordered (red triangles). Diffractive peaks observed in Figure 4.6 are identified with side markers: Peak 1 (hollow pointer) and Peak 2 (striated pointer). Sensitivity values for EL ordered sample have been shifted from measured particle size to allow error bars to be clearly seen. Dotted lines are to guide the eye for trends in simulated sensitivity as a function of particle size. Small light green points represent experimental results from the literature for spherical gold NPs.[33,82,114–118]

CHAPTER 5

NANORING DIFFRACTIVE SENSORS

5.1 NANORING MOTIVATION

Spherical nanoparticles have one of the lowest shape sensitivities of any NP sensors. Now that diffractive coupling has been demonstrated as a sensor, it can be extended to different NP shapes. LSPR sensors work by detecting the change in RI close to the surface of the NP. If the surface area is increased, the sensor should be more sensitive to local RI changes. A quick comparison of different geometric shapes (spheres, cylinders, rods (3:1 length to width), tetrahedrons, a 20 nm thick ring, and a 10 nm thick ring) surface area to volume shows that nanorings have the highest surface area to volume of the shapes considered. Each geometric shape has its volume set equal to the volume of a 50 nm radius nanosphere and the height fixed at 50 nm, except the tetrahedron which assumed equal side length on all sides (but still equal to the volume of the 50 nm radius sphere). The ratios of surface area to volume for each shape are 0.060, 0.075, 0.085, 0.089, 0.140, and 0.240, respectively. Based on this analysis, rings with a wall thickness of 10 nm have four times the surface area of an equivalent volume sphere.

Increased surface area is not the only motivation for nanoring selection. Plasmonic sensors with different shapes have different sensitivities. Table 1.1 illustrates that spheres have the lowest shape sensitivity of several different NP geometries. Previous experiments with nanorings that do not couple have been shown to have one of the highest RI sensitivities reported for plasmonic sensors at 880 nm/RIU.[63] This high sensitivity has the potential to be augmented even further by configuring the nanorings into ordered arrays that support diffractive coupling. Another motivating factor for nanoring research is the wavelength of the produced LSPR feature.

Researchers have reported nanoring LSPR wavelengths between 620 and 1545 nm.[63,79,119–125] These wavelengths represent the near infrared region of the EM spectrum. This region is significant in the development of sensors for biological systems and is known as the diagnostic window. In the visible range, light does not penetrate deep into living tissue due to interactions with components such as hemoglobin, water, and lipids.[126] However, in the diagnostic window, these interactions are minimized which makes sensing in this region desirable for biological applications.

This chapter outlines numerical simulations on ordered arrays of nanorings to determine their potential for sensing. Numerical simulation results are compared to existing nanoring properties in the literature and trends useful in sensor design are identified.

5.2 NANORING SIMULATIONS

Nanoring characteristics were simulated using the program DDSCAT for the following range of parameters: inner radius from 25 to 80 nm (25, 30, 35, 40, 45, 50, 60, 70, 75, and 80 nm), ring wall thickness of 10 and 20 nm, and inter-particle spacings from 500 to 1000 nm (500, 600, 670, 700, 800, 900, and 1000). Figure 5.1 identifies nanoring parameters, including inner radius, r_{in}, thickness, t, height, h, and inter-particle spacing, d_x and d_y. Extinction, scattering, and absorption efficiencies were calculated for the wavelength range from 400 to 1400 nm with a 1 nm resolution. Nanorings were simulated as individual particles as well as square arrays with the afore-mentioned inter-particle spacings. A total of 112 nanoring simulations were performed.

Matlab was used to generate nanoring dipole locations for DDSCAT. Rings were generated by discretization of two concentric circles using an implementation of a Bresenham algorithm written by John Kennedy.[127] The controlled parameters for target generation were the

desired nanoring internal radius, wall thickness, and inter-particle spacing. The program used, included in Appendix A.3, compared these parameters to find the largest dipole discretization value that would allow all of the input parameters to be matched in the created nanoring structure. This resulted in various numbers of dipoles for the different nanoring dimensions. The number of dipoles varied between 5175 and 13200 and between 400 and 1050 for ring thickness of 10 and 20 nm, respectively. The number of dipoles was decreased for the 20 nm thick rings to reduce computation time. Computational time was approximately 291 days for the 10 nm thick nanoring simulations with each simulation requiring between 1-10 days on an 8 core processor node. The reduction in the number of dipoles tends to blue shift the plasmon frequency; however, the trends between the plasmon peak and the diffractive coupling peak positions and magnitudes are still consistent with simulations with more dipoles.

Simulation accuracy can be improved by increasing the number of dipoles in the simulation, but this accuracy comes at a cost of increased computational time. This increased computational time is not always warranted. For the present study, the goal is to determine general trends that exist for diffractive coupling in nanoring arrays over a wide range of conditions. It is important to know what tradeoffs exist in terms of accuracy and computational time to pick appropriate simulation conditions. DDA simulations were previously performed in which 10 and 100 nm spheres were both modeled with a diameter consisting of 32 and 128 dipoles.[128] The peak position error relative to Mie theory ranged from 5.8 nm for the 10 nm sphere with 32 dipoles across to 1.0 nm for the 100 nm sphere with 128 dipoles across. Multiple simulations of the same nanoring were performed only changing the number of dipoles in the nanoring to determine the change in peak position for nanorings with an increasing number of dipoles. Figure 5.2 shows these simulations for 675 (blue), 5250 (green), and 17625 (red)

dipoles for a nanoring with r_{in} = 50 nm, t = 20 nm, and h = 50 nm and compares the peak locations to experimental data for a comparable nanoring reported by Huang *et al.*[123] Because the thickness (t = 15 nm) of the experimental nanoring is between those simulated in this work, Figure 5.2 also shows a nanoring with the same radius and height but with t = 10 nm (orange dotted). The experimental peak location is between the simulated peak locations as expected, indicating good correlation with experiment when a sufficient number of dipoles are included in the numerical simulations. When the number of dipoles is very small, the shape of the peak changes, showing multiple peaks when only one is predicted with a larger number of dipoles. Table 5.2 shows the number of dipoles used in each simulation.

Peak locations in the extinction spectra were identified using a peak detection algorithm (*peakdet*) freely available through Matlab exchange. Single nanoring spectra are shown in Figure 5.3. Nanorings for t = 10 and 20 nm with . Two spectral features were observed in some of the simulations at 564 and 1265 nm. These features appear when the gold RI data reported by Palik[129] are used but are not seen when using the data of Johnson and Christy[130] (Figure 5.4). Both sets of data are used regularly in the literature. Ungureanu *et al.* compared these RI data for nanospheres and nanorods and showed that for spheres there was a shift in plasmon peak position between these two data while suggesting that Palik data show excellent correlation with experimental data.[131] Despite this feature related to the choice of gold RI, this study is interested in how plasmon and diffractive coupling features change in relation to each other in the simulations. It is important to note for studies requiring more accurate peak wavelengths, correlation with experimental results will be necessary to determine the appropriate gold RI data.

5.2.1 General Observations for Nanoring Simulations

Extinction spectra for nanorings with a 10 nm thickness follow a similar pattern to other nanoparticle shapes as size increases; as the size increases, so does the wavelength of the maximum extinction peak. This shift results from phase retardation due to the increase in particle size. As the nanoring increases in size, higher order modes of electron oscillation occur. Interactions between existing oscillation modes results in phase retardation which is observed as a red shift in the plasmon wavelength.[132] Nanorings with a 20 nm thickness in general follow this trend, but multiple peaks begin to appear as the particle size reaches 50 nm. As previously mentioned, the multiple peaks in these simulations result from the small number of dipoles utilized for these nanoring simulations. This suggests for accurate prediction of peak positions for these nanorings, more dipoles would be required. Draine and Flatau performed an analysis of DDSCAT accuracy for spheres with a changing number of dipoles. They reported an error in the absorption efficiency of ~6% for a sphere consisting of 304 dipoles.[100] Unfortunately, it appears nanorings are more sensitive to the number of dipoles, potentially because of EM interactions between the inner and outer walls. Nanoring simulations that show multiple peaks due to a limited number of dipoles should not be considered representative of nanorings of that size. However, trends in diffracting coupling peak position and shifts seem consistent for these simulations and those simulations with more dipoles. It is important to remember that the peak positions that were calculated for the thicker nanorings cannot be directly compared to those from the thinner rings because of the discrepancy in the number of dipoles.

The observed red shift in plasmon peak location is accompanied by a broadening of the plasmon peak with increasing nanoring inner radius. The full width at half maximum for single 10 nm thick nanorings are 46, 73, 58, 75, 116, 102, and 134 nm for increasing r_{in} from 25, 35,

45, 50, 60, 70, to 75 nm, respectively (Figure 5.3 A)). Observations with nanospheres attribute this plasmon peak broadening to retardation effects and/or interaction between different modes' (dipole, quadrupole, *etc.*) electrons, reducing phase coherence.[132] These observations can be extended to nanorings because coupling between the inner and outer nanoring surface occurs, similar to that observed in a small NP.[125]

Diffractive coupling is observed in the simulations when the nanorings are modeled as periodic square arrays. Figure 5.5 shows how the diffractive coupling peak changes as inter-particle spacing increases for a nanoring with r_{in} = 50 nm, t = 10 nm, and h = 50 nm. The diffractive peak intensity is largest when the coupling takes place at wavelengths slightly longer than the plasmon peak wavelength. Inspection of nanoring array simulations where the inter-particle spacing is less than the plasmon wavelength shows a diffractive peak at double the inter-particle spacing. The plasmon peak wavelength follows an interesting trend for a given nanoring size at different inter-particle spacing values. For most simulations, the nanoring plasmon peak for ordered arrays 'traces' the plasmon spectra. An illustration of this is shown in Figure 5.6. Here, nanorings with an r_{in} = 50 nm, t = 10 nm are shown for a single particle (solid blue) and inter-particle spacings of 500 nm (dash red), 600 nm (dash dot green) and 700 nm(dot orange). As the spacing increases, the diffractive coupling has less effect on the plasmon peak and it returns toward its single nanoring intensity and peak wavelength. This trend has also been observed in simulations with rsa-CDA. Work is underway to determine if this is the result of isometric polarizability values which are favorable for plasmonic resonance or a different phenomenon.

Extinction, scattering, and absorbance efficiencies were calculated for each of the nanoring arrays. Typically diffractive coupling has been attributed to coherent interactions between EM waves scattered between NPs in an array. Analysis of the contributions of scattering and absorption for diffractive coupling indicates that absorbance has a significant contribution to the diffractive coupling peak, especially when the diffractive peak is close to the plasmon peak. For a r_{in} = 60 nm, t = 10 nm nanoring with an inter-particle spacing of 900 nm, the diffractive peak in extinction spectra is the result of 50.5% absorption and 49.5% scattering, determined from the calculated absorption and scattering cross sections shown in Figure 5.7. This observation is useful in the application of nanoring arrays to plasmonic heating. Device parameters could be tuned to give a strong absorption component of the diffractive coupling peak to amplify the amount of heat generated.

Near field spectra calculations were performed for a r_{in} = 50 nm, t = 20 nm, and inter-particle spacing of 500 nm nanoring. Two wavelengths were examined: the plasmon wavelength of 771 nm and the diffractive coupling region at 1004 nm. Irregular field patterns lacking expected symmetry were observed in both simulations. These irregularities occurred within the nanoring structure but also influenced the field outside the nanoring. The number of dipoles included for the near field simulation was increased from 675 to 80,000 to determine if the number of dipoles was the source of the irregularities. Increasing the number of dipoles resulted in a more uniform field outside the nanoparticle and reduced the irregularities inside the nanoring structure, but areas of high field intensity without the expected symmetry were still observed (Figure 5.8). In a previous manuscript performing DDA calculations for a gold nanoring, the field inside the nanoring structure was set to zero.[63] It is unclear whether the field pattern outside the particle is accurate in this case since other reported simulations include the field information

inside the nanoring structure.[123,125,133] Despite these irregularities in the field information, the extinction spectra are comparable to experimental data, as shown in Figure 5.2.

5.2.2 COMPARISON TO NANORINGS IN LITERATURE

Nanoring simulations in this work are comparable to previously reported single nanoring spectral response. Table 5.1 lists nanoring results from the literature for nanorings with an inner diameter in the range of 45-50 nm with a wall thickness range of 10-20 nm. These reported values were chosen because of their dimensional similarity to the simulations reported in this chapter. Even for the small size range in the table, the LSPR peak wavelength ranges from ~800 to 1360 nm. All of the nanorings reported were supported with experimental data and simulation. This wide range suggests that nanorings are very sensitive to small changes in their dimensional properties. Aizpurua *et al.* reported a wavelength change of -190 nm when the thickness was reduced by 1 nm.[125] However, results by Huang *et al.* for the same size nanoring with a thickness increase of 5 nm compared to Aizpurua *et al.*'s 10 nm thick ring show a change of +372 nm.[123] Shifting the comparison to r_{in} = 45 nm nanorings, the original trend is observed, with a shift of -354 nm. These discrepancies in reported peak locations make it difficult to confirm the accuracy of the simulation data reported in this chapter, even when the data is supported by experimental results. The results reported in this chapter are similar in peak shape and wavelength (shown in Figure 5.2) to those reported by Huang *et al*.[123]

Despite the wide range of peak locations for similar nanorings in the literature, several trends can be observed from the reported values. First, the LSPR peak tends to blue shift as the nanoring thickness is reduced. This has been attributed to coupling between the inner and outer nanoring surface, resulting in a mode splitting polarization scheme.[134] As the thickness of a

nanoring increases, the mode produced by this coupling converges to that of a planar surface plasmon mode. An alternative way of understanding this phenomenon is to consider what happens to the conduction electrons as the ring thickness decreases. Remembering that LSPR is an oscillation of conduction electrons, the mean free path for these electrons (50 nm in gold) becomes important as NP size decreases below this length.[135] When the NP size is less than this bulk mean free path, electron collisions with the surface of the NP result in a reduction of the mean free path and in turn a blue shift and peak broadening.[136] This blue shift was not observed in the simulations reported in this chapter at different ring thicknesses, which has already been proscribed to the reduction of dipoles in the thicker nanoring simulations. Second, the LSPR wavelength for nanorings with similar wall thickness increases with increasing nanoring inner diameter. The simulation data presented in this chapter corresponds well with this observed trend. Trends relating to nanoring height are not as easily discernible from the reported literature. Red shifts with increasing height have been reported, but the supporting data was not provided.[125] The rationale for this trend is similar to that of the wall thickness, that a mode splitting polarization scheme is established between the top and bottom surface of the nanoring.

5.3 DIFFRACTIVE COUPLING IN NANORING ARRAYS

Several notable differences exist in the coupling in ordered nanoring arrays and ordered spherical NP arrays. First, a coupling peak exists when the inter-particle spacing is less than the plasmon frequency. For all of the simulated spectra, the plasmon frequency was higher than 600 nm, but coupling was observed for both 500 and 600 nm spacings, albeit at double the inter-particle spacing, 1000 and 1200 nm, respectively. Figure 5.9 illustrates this trend for the 500 nm spacing with 10 nm wall thickness. This constructive interference occurs at a harmonic of the inter-particle spacing. This double wavelength coupling was also observed for the 670 nm inter-

particle spacing. Second, for nearly all the cases simulated, the diffractive coupling peak is smaller than the single particle plasmon frequency. Spherical NPs exhibit diffractive coupling peaks that are much larger than the single particle case. This is probably related to the low number of dipoles in the current study as well as the relatively few nanoring sizes and inter-particle spacings simulated. Additional simulations near the strongest diffractive coupling observed in these simulations will aid in the determination of higher extinction efficiency regions for the diffractive peak. Unfortunately, the computation time required for nanorings in periodic arrays did not allow for a more in depth analysis in this work. Work is underway to determine if an effective polarizability can be calculated for the nanorings which could then be used with the more rapid rsa-CDA approach.

The diffractive coupling peak increases as the nanoring radius increases. Figure 5.10 shows how the simulated diffractive peak extinction efficiency changes as a function of particle size for each nanoring inner radius at t = 10 nm and d = 1000 nm. This is similar to the trend observed for the plasmon peak for single nanorings. The largest magnitude diffractive coupling feature observed for 10 nm thick rings is for r_{in} = 75 nm. However, this peak magnitude was less than the single particle case (shown in Figure 5.3 A). The only 10 nm thick nanoring in the present study to have a larger extinction efficiency for the diffractive coupled feature when compared to the plasmon peak was at r_{in} = 60 nm at 900 nm inter-particle spacing. Figure 5.11 shows these two nanorings with the maximum diffractive coupling peak and with the single nanoring for each case. The overall extinction efficiency of the diffractive coupling peak for the r_{in} = 75 nm nanoring is larger, but does not exceed the single particle plasmon.

Another interesting observation is that for all inter-particle spacings and nanoring parameters simulated, there is evidence of diffractive coupling. When the same inter-particle spacing values are simulated (with CDA) for spheres equal to the radius values used in nanorings, the window where coupling is observed is much narrower. This might indicate that the nanoring structure is more tolerant to differences in fabrication conditions than spherical NPs, but further work is required to verify this result.

A very interesting feature was discovered related to diffractive coupling in nanorings at 80% of the diffractive coupling peak. This feature is apparent in Figure 5.10 at a wavelength of ~800 nm. This peak occurs in all of the nanoring simulations, independent of size, number of dipoles, thickness, or inter-particle spacing. Initially, it was believed that this peak was due to constructive interference between NPs not along the principle diffraction axis. These off-axial, off-diagonal particles are known to contribute significantly in arrays of nanospheres.[62] Further work is needed to verify the exact source of this feature.

Interactions between the nanoring plasmon peak and the diffractive coupling peak in simulations suggest that the plasmon FWHM can be significantly reduced by destructive interference when the diffractive coupling peak coincides with the plasmon peak. Figure 5.12 shows this peak narrowing for a r_{in} = 25 nm, t = 20 nm nanoring with a single particle (blue) and inter-particle spacings of 670 nm (red) and 700 nm (green). When the plasmon and inter-particle spacings are farther apart, the plasmon peak broadens and red shifts. The plasmon peak narrows as the inter-particle spacing approaches the plasmon wavelength. This ability to reduce the FWHM could be coupled with diffractive coupling to increase sensor performance more than with diffractive coupling alone.

5.4 SENSITIVITY OF DIFFRACTIVE COUPLING NANORING ARRAY

A sensitivity analysis to changes in RI from vacuum to water was performed for the simulation that had a diffractive coupling peak that was larger than the plasmon peak of the single nanoring. This occurred for the r_{in} = 60 nm, t = 10 nm nanoring with an inter-particle spacing of 900 nm whose spectra are shown in Figure 5.13. The plasmon peak wavelength for the array in air was at 839 nm. This peak shifted to 1096 nm in a water environment. Using EQ 2-4, the sensitivity of the plasmon peak is 773 nm/RIU. This value is comparable to nanoring sensitivities of 740 and 880 nm/RIU reported for nanorings with inner diameters of 45 and 60 nm, respectively, and a ring thickness of ~15 nm.[63] The diffractive coupling peak was also analyzed for its sensing characteristics. The observed diffractive coupling peak shifted from 917 nm to 1216 nm for simulations in air and water, respectively. The sensitivity of the diffractive coupling peak is therefore 896 nm/RIU, or an increase of 15.9% relative to the plasmon peak. This simulation indicates that the RI sensitivity for ordered arrays of nanorings which exhibit diffractive coupling is comparable to the highest reported nanoring plasmon sensitivity. Further increases in the diffractive coupling magnitude and FWHM should be possible by determining appropriate nanoring array conditions to promote diffractive coupling.

While the bulk sensitivity shows a modest increase relative to current nanoring sensors, the figure of merit far exceeds any known figure of merit for plasmonic sensors. The figure of merit is the ratio of the sensitivity to the full width at half maximum, as defined in EQ 2-6. The FWHM for the diffractive coupling peak of this simulated sensor is 26 nm, with a corresponding figure of merit of 34. A recent analysis of diffractive coupling sensors indicates that the figure of merit for the diffractive coupling feature in arrays of spheroidal NPs is solely a function of the frequency difference between the plasmonic peak and the diffractive coupling peak.[117] This is

important because it indicates that the figure of merit can be maximized for any nanoparticle shape or, composition allowing sensors to be designed for specific applications without a costly trial and error approach. A comparison of FOM values for non-diffractive sensors and diffractive sensors shows a significant increase for diffractive coupling sensors (see Table 5.3).

5.5 CONCLUSIONS

Ordered arrays of nanorings were characterized for their ability to support diffractive coupling over a wide range of nanoring sizes and inter-particle spacings. Numerical simulations indicated that nanorings with an internal radius of 60 nm and a wall thickness of 10 nm with a spacing of 900 nm have a diffractive coupling peak that exceeds the magnitude of the single particle plasmon peak. The sensitivity of this nanoring array to changes in RI was 896 nm/RIU for the diffractive coupling peak, which is an increase over current plasmonic sensor sensitivities. The figure of merit for this simulated nanoring sensor evaluated for the diffractive coupling peak was 34, which is the highest known figure of merit for plasmonic sensors. Further simulation work will help identify diffractive coupling nanoring sensors that exceed even these values.

TABLE 5.1: Nanoring characteristics as reported in the literature for randomly arranged, 45-55 nm inner radius nanorings.

r_{in}, nm	t, nm	h, nm	LSPR Peak, nm	Simulation	Reference
45	15‡	60‡	1354†	DDA	Larsson[137]
46	14	40	1000	Boundary Element	Aizpurua[125]
48.5	11.5	60	1030†	Finite Element	Tseng[138]
50	10	40	1170	Boundary Element	Aizpurua[125]
50	15	—	798	FDTD	Huang[123]
51	9	40	1360	Boundary Element	Aizpurua[125]
55	20‡	50‡	1223†	DDA	Larsson[137]

† Peak wavelength in refractive index of water
‡ Dimension approximated from SEM images

TABLE 5.2: Number of dipoles in each nanoring simulation.

***t* = 10 nm**		***t* = 20 nm**	
r_{in}, nm	**Number of Dipoles**	**r_{in}, nm**	**Number of Dipoles**
25	5175	30	400
35	6375	40	575
45	7650	50	675
50	8700	60	625
60	10425	70	875
70	11775	80	1050
75	13200		

TABLE 5.3: Figure of Merit comparison for non-diffractive and diffractive coupling sensors.

Shape	Material	Sensitivity nm/RIU	FOM	Reference
Sphere	Au	76.4	0.66	Nath[53]
Cube	Ag	118	5.4	Sherry[65]
Triangle	Ag	160	2.2	Mayer[64]
Rod	Au	170	1.3	Mayer[64]
Disc	Au	200	1.7	Dmitriev[66]
Bipyramid	Au	540	4.5	Chen[67]
Stars	Au	665	5.4	Nehl[68]
Ring	Au	880	2	Larsson[63]
EL	Au	180	2.1	(Experimental)
Ordered		48	2.3	(CDA)
Sputtered	Au	88	0.9	(Experimental)
Ordered		62	1.7	(CDA)
Diffractive Cylinder	Au	N/A	25	Offermans[117]
Diffractive Ring	Au	896	34	(DDA)

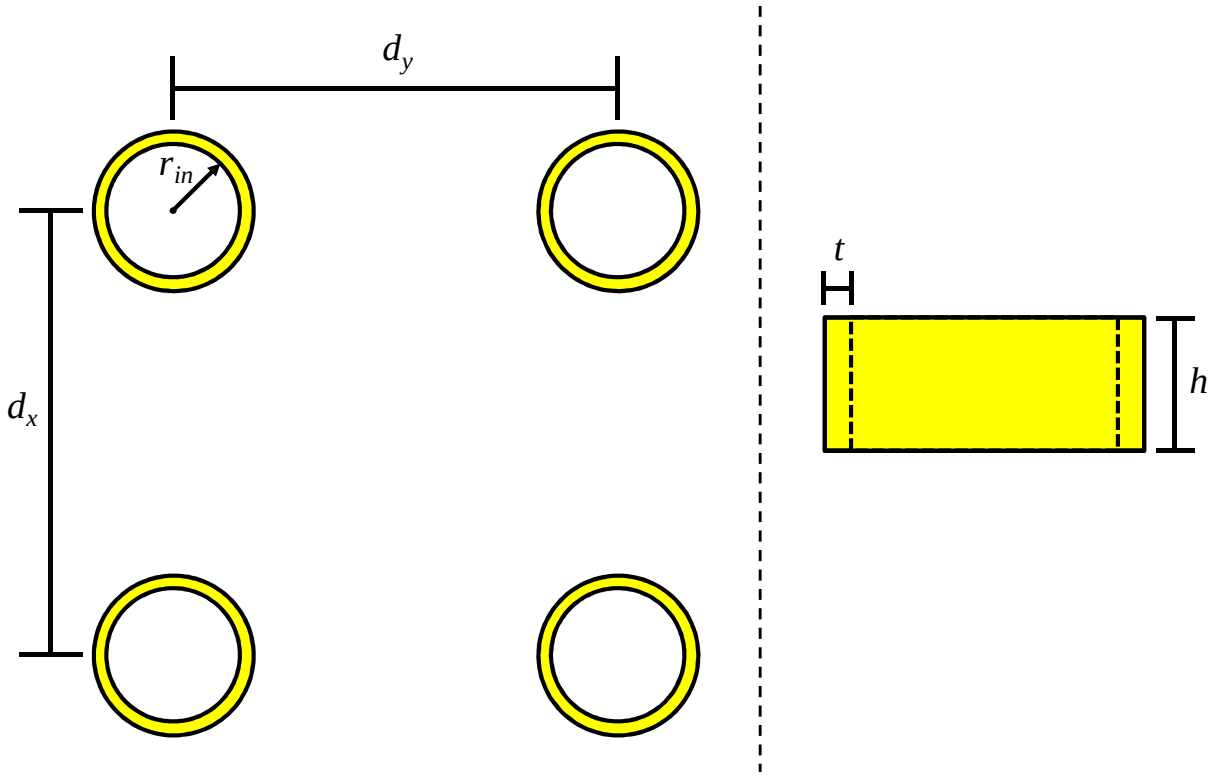

FIGURE 5.1: Depiction of nanoring dimensions for ordered arrays of nanorings: r_{in} is the inner radius, t is the wall thickness, d_x and d_y are the interparticle spacings in x and y, respectively, and h is nanoring height.

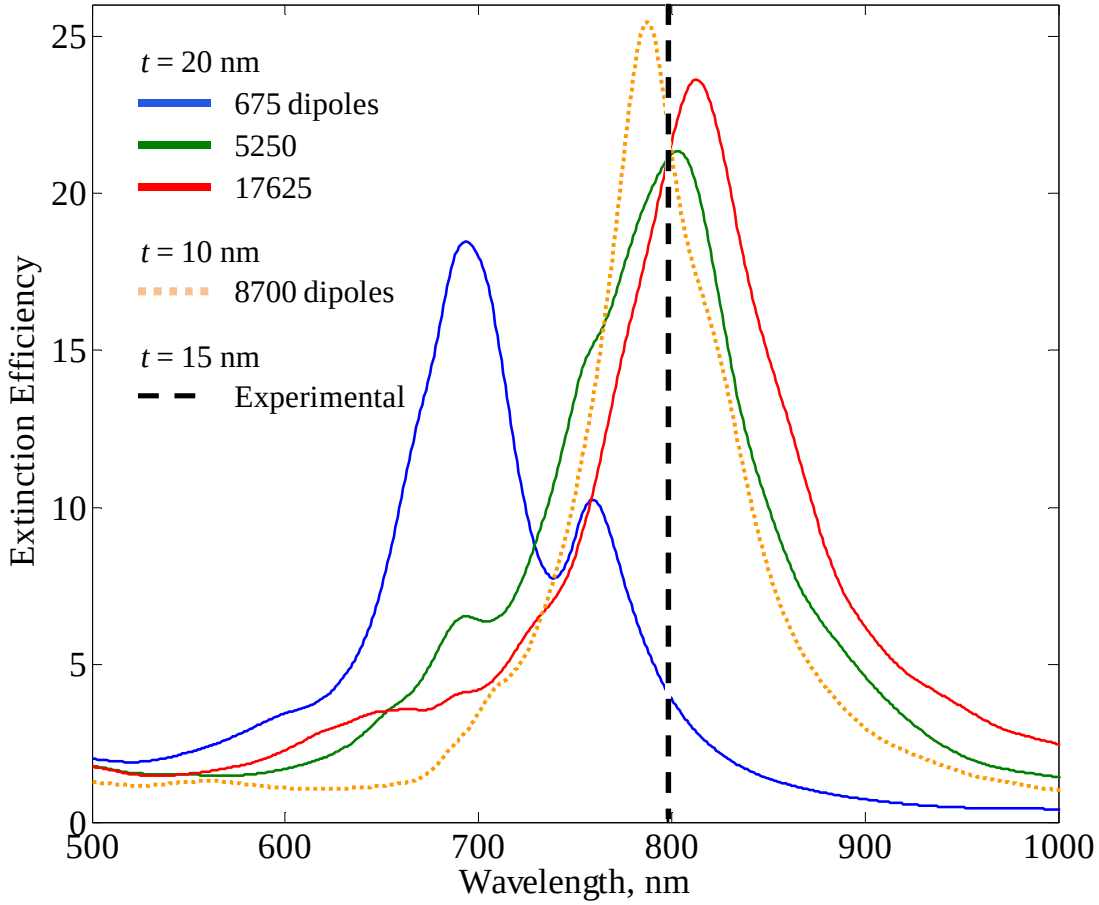

FIGURE 5.2: Nanoring simulations for increasing number of dipoles for a nanoring with r_{in} = 50 nm and h = 50 nm. As the number of dipoles increases from 675 to 17625 for the 20 nm thick nanoring, the peak redshifts and the amount of shift decreases with each increment in the number of dipoles. Experimental peak location data from Huang *et al.* for nanorings with r_{in} = 50 nm and t = 15 nm is marked with the dashed black line. This peak location is in between those simulated for t = 10 nm (orange dotted) and t = 20 nm rings.

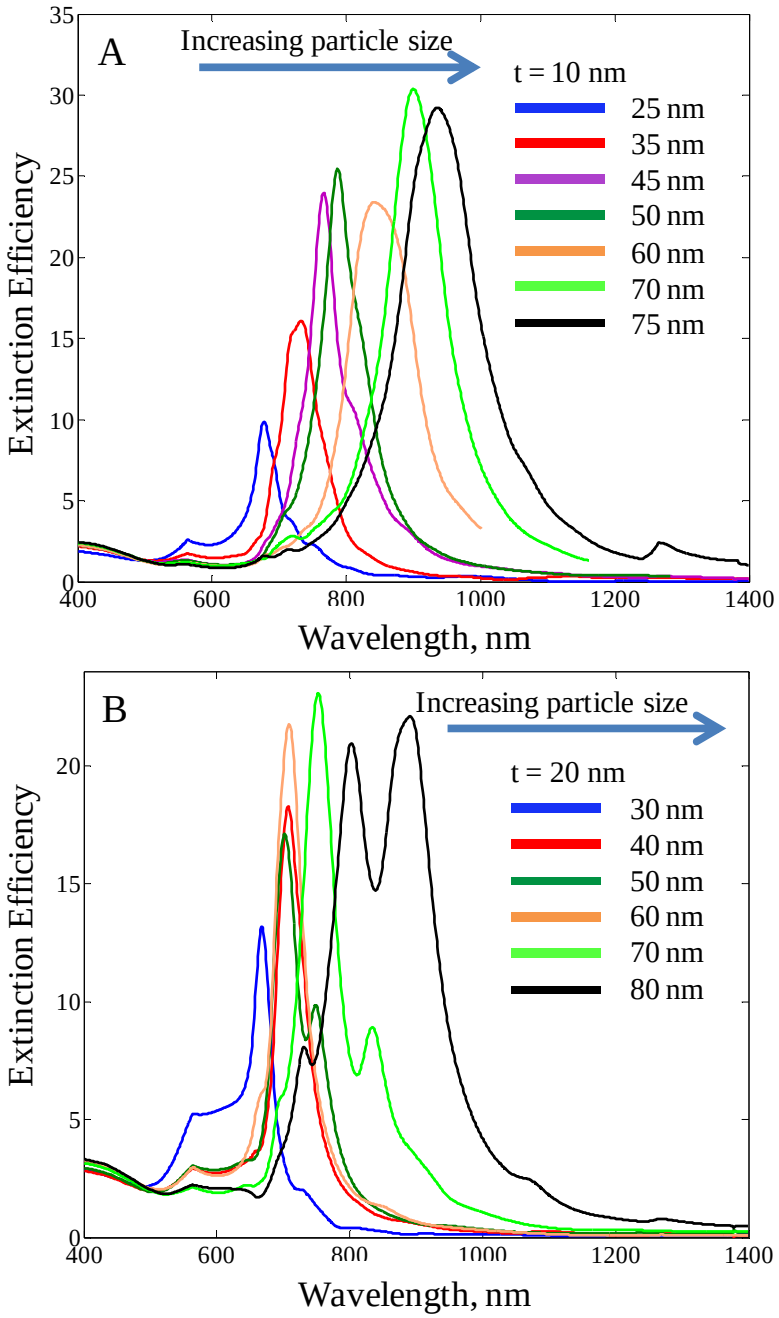

FIGURE 5.3: Single nanoring simulation extinction spectra for A) t = 10 nm and B) 20 nm with r_{in} = 25 – 80 nm and h = 50 nm.

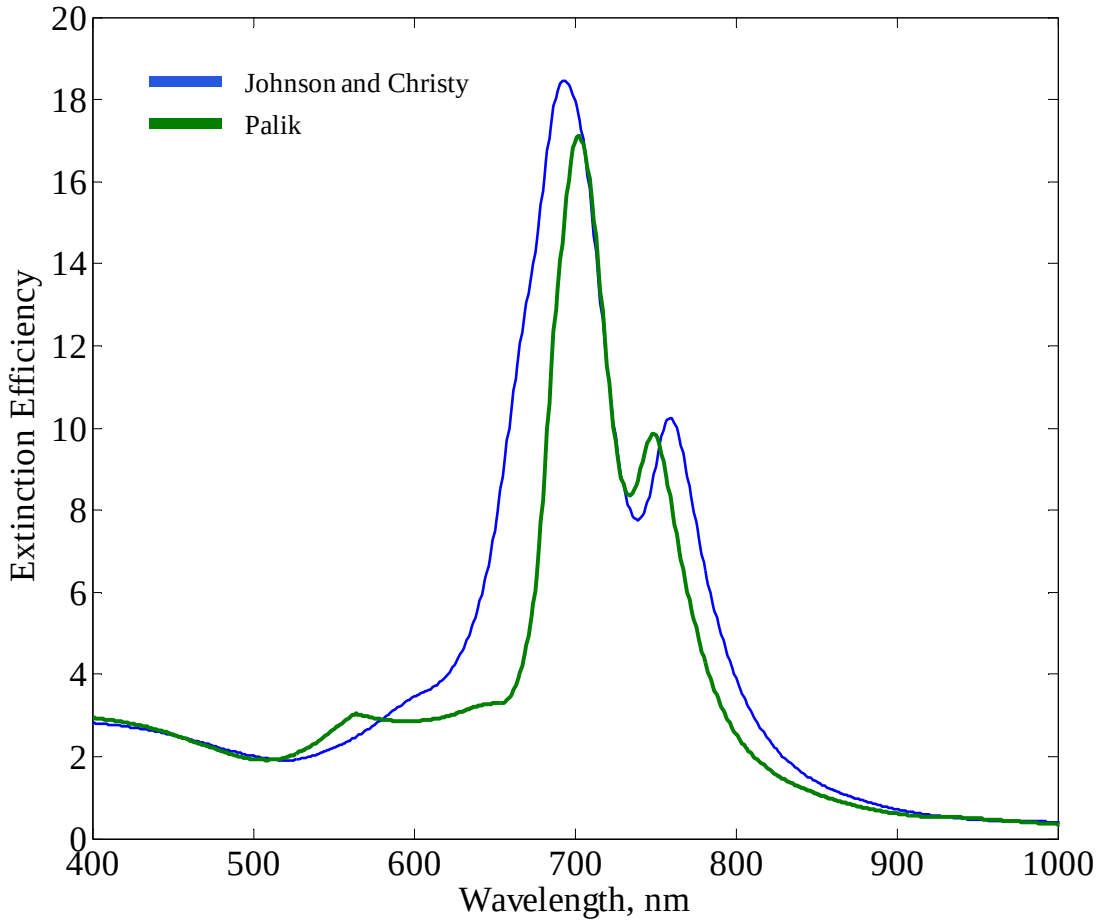

FIGURE 5.4: Comparison of Simulated spectra using gold RI values from Johnson and Christy (blue) and Palik (green) for a nanoring with r_{in} = 50 nm, t = 20 nm, and h = 50 nm. General peak features are similar, but the Palik simulation has a shoulder at 564 nm and is narrowed relative to the Johnson and Christy simulation.

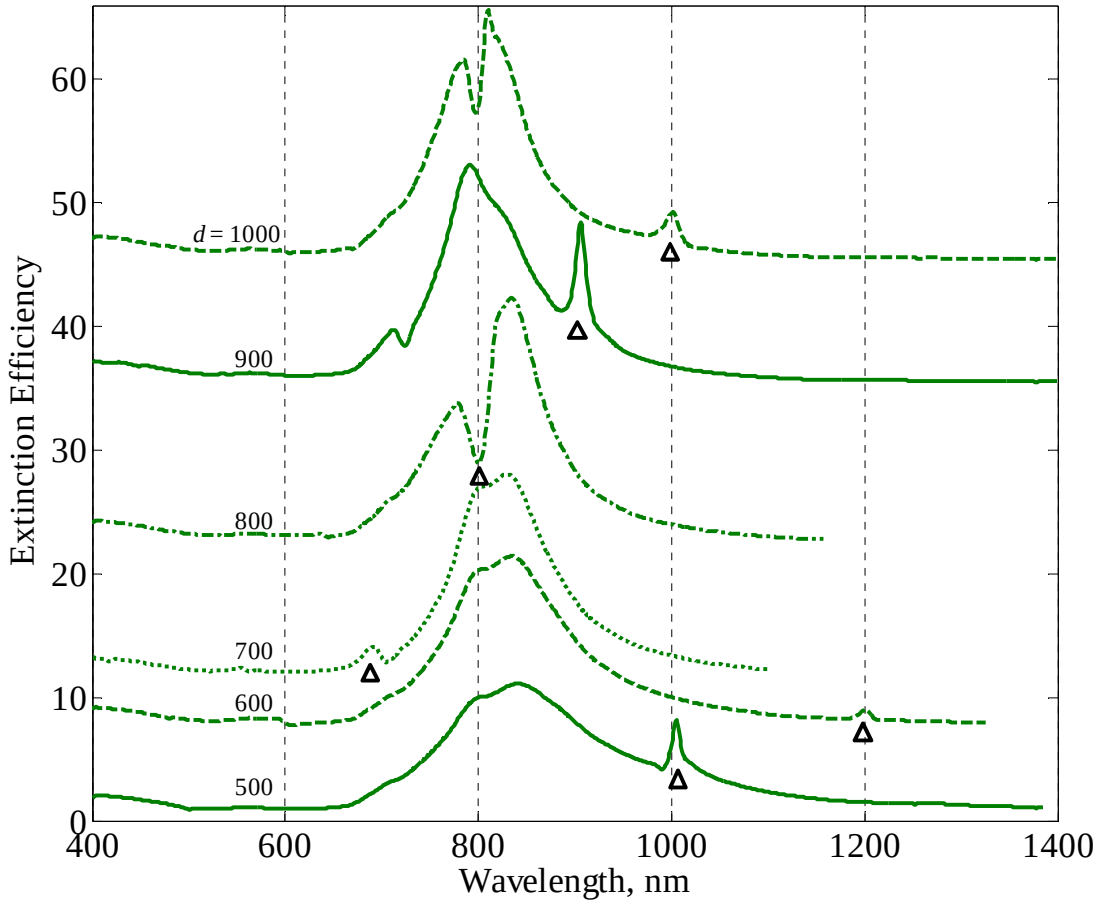

FIGURE 5.5: Diffractive coupling peaks as inter-particle spacing, d is increased from 500 to 1000 nm for r_{in} = 50 nm, t = 10 nm, and h = 50 nm. Diffractive coupling features are marked with a pointer. Simulated spectra are vertically shifted for clarity.

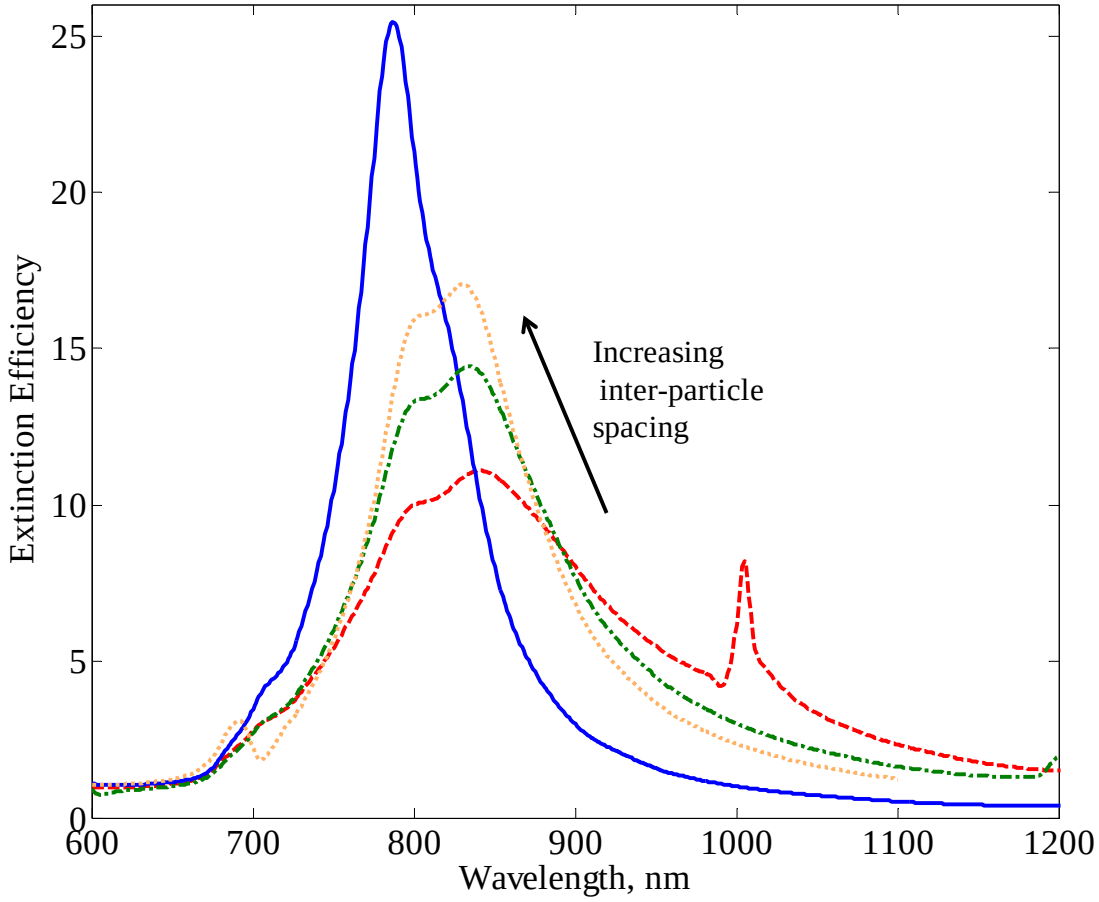

FIGURE 5.6: Plasmon peak tracing observed for nanorings with r_{in} = 50 nm, t = 10 nm and a varied from a single particle (solid blue) to inter-particle spacings of 500 nm (dash red), 600 nm (dash dot green) and 700 nm(dot orange). A diffractive coupling peak is visible for the 500 nm inter-particle spacing at 1000 nm.

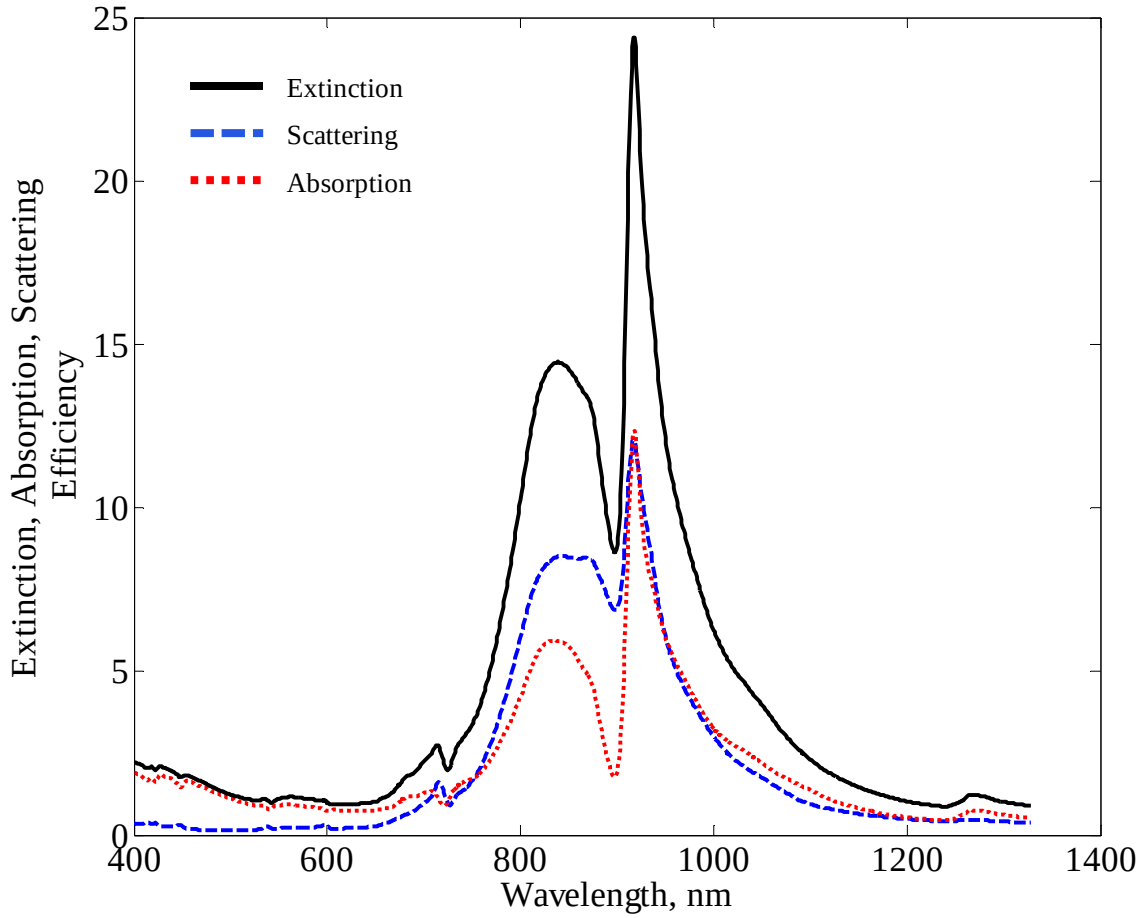

FIGURE 5.7: Scattering, absorption, and extinction simulated spectra for a nanoring with r_{in} = 60 nm, t = 10 nm, h = 50 nm, and d = 900 nm. The diffractive extinction peak at 917 nm is 50.5% absorption and 49.5% scattering.

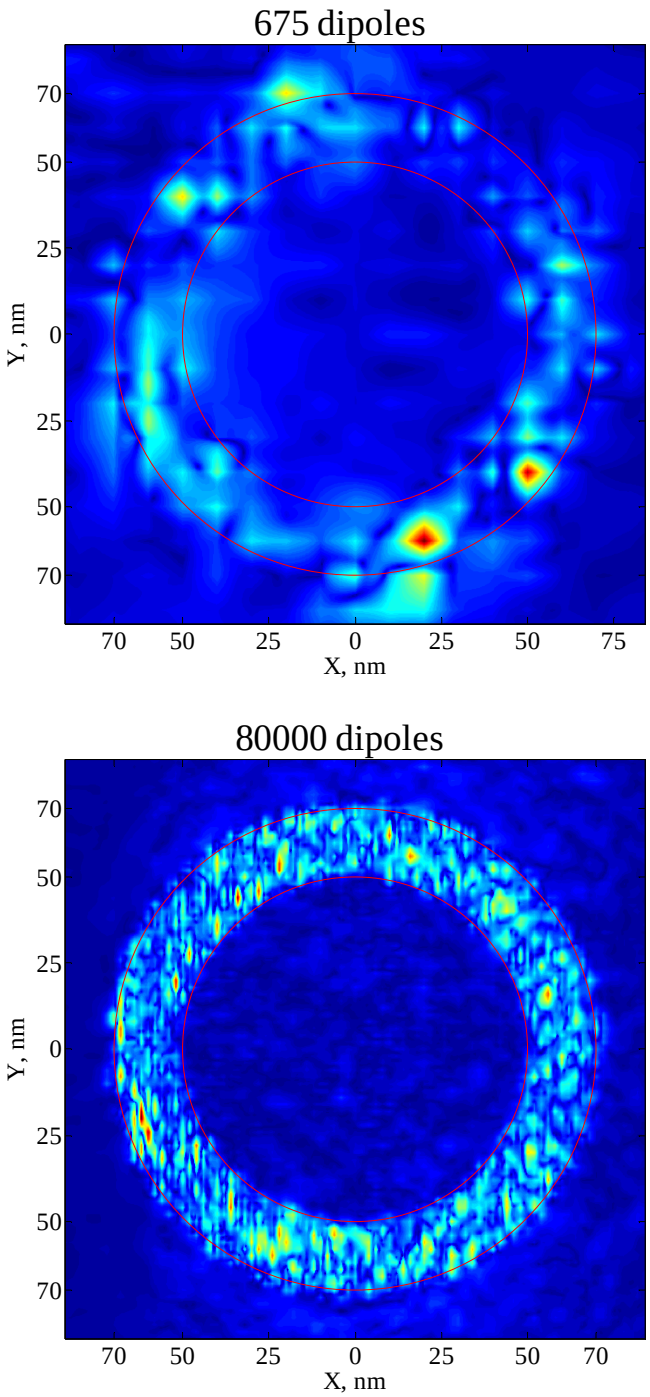

FIGURE 5.8: Near field simulations for a nanoring with r_{in} = 50 nm, t = 20 nm, and h = 50 nm at 771 nm. Field information is taken at a height of Z = 38 nm from the nanoring base. Red lines represent the nanoring cross-section. Irregular regions exist inside and outside the 675 dipole nanoring, while the irregularities appear to be restricted to inside the 80,000 dipole nanoring. Field is polarized along the X axis in both cases.

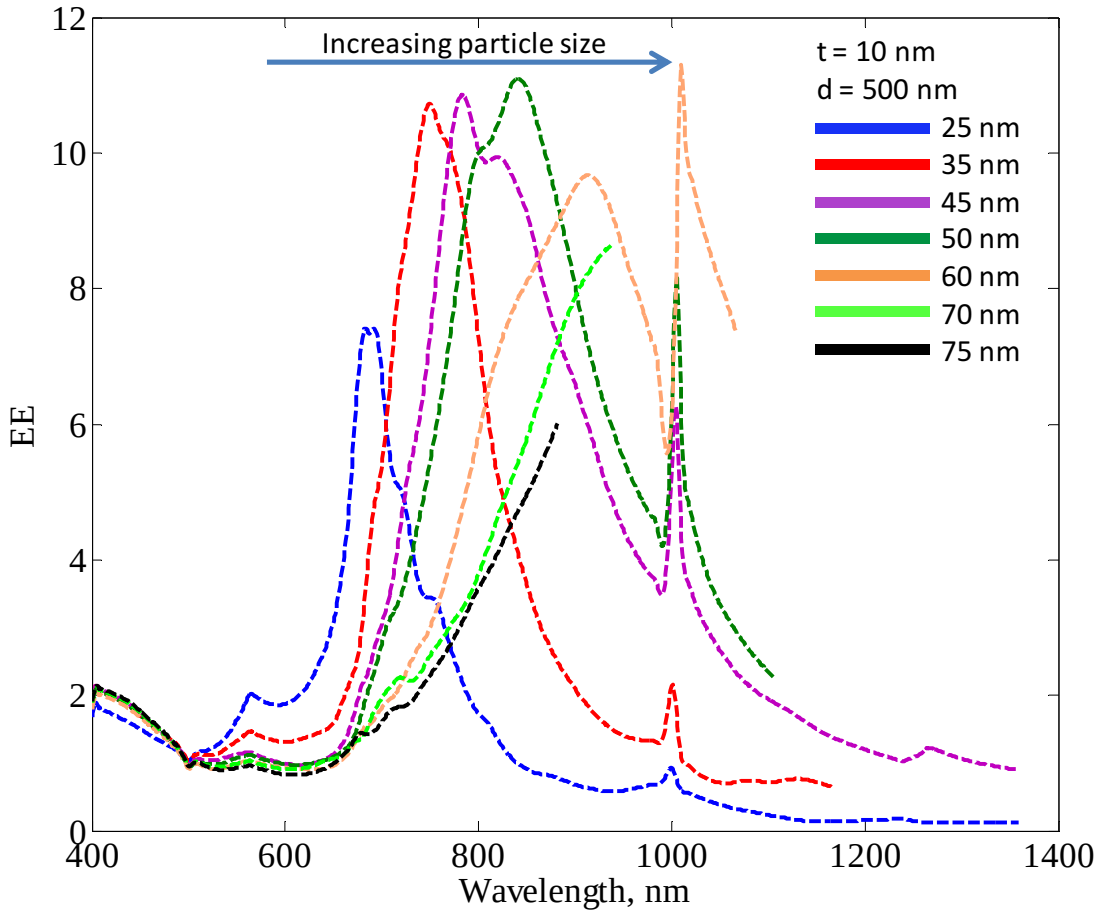

FIGURE 5.9: Illustration of diffractive coupling when inter-particle spacing is less than the plasmon frequency. Inter-particle spacing is 500 nm and t = 10 nm. Spectra are labeled according to r_{in}.

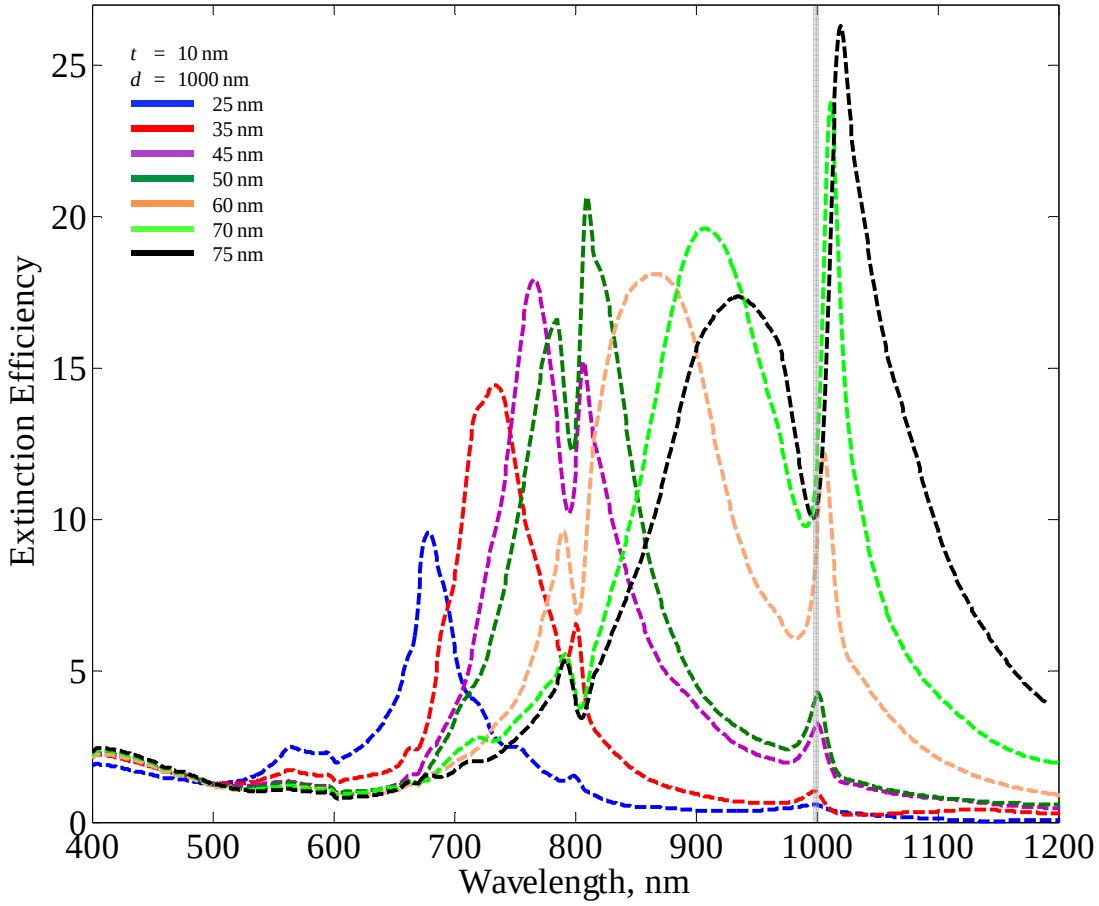

FIGURE 5.10: Increase in diffractive coupling peak extinction efficiency with increasing nanoring inner radius at t = 10 nm, d = 1000 nm, and h = 50 nm.

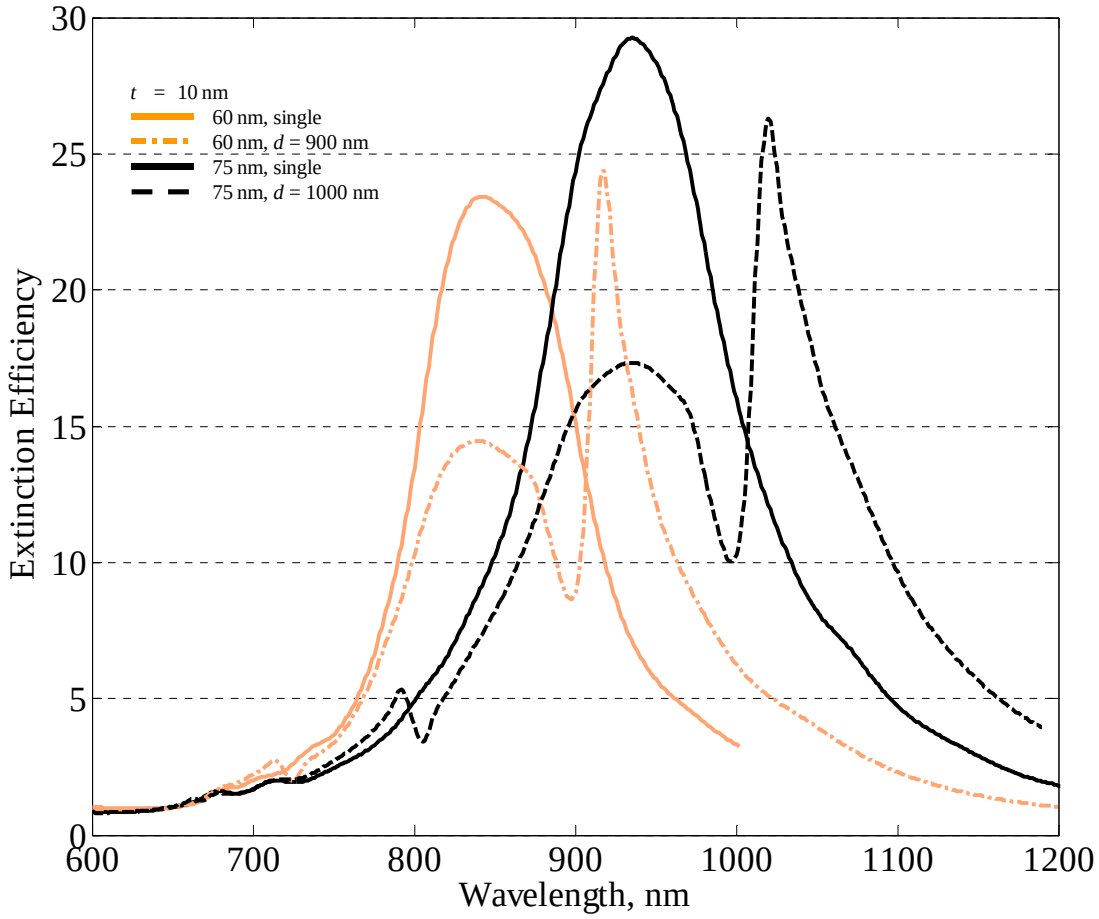

FIGURE 5.11: Comparison of diffractive peaks and single nanoring plasmons for r_{in} = 60 and 75 nm. The 60 nm nanoring with an interparticle spacing of 900 nm has a diffractive peak that is larger than the single nanoring case but it has a lower extinction efficiency than the 75 nm diffractive peak at an inter-particle spacing of 1000 nm.

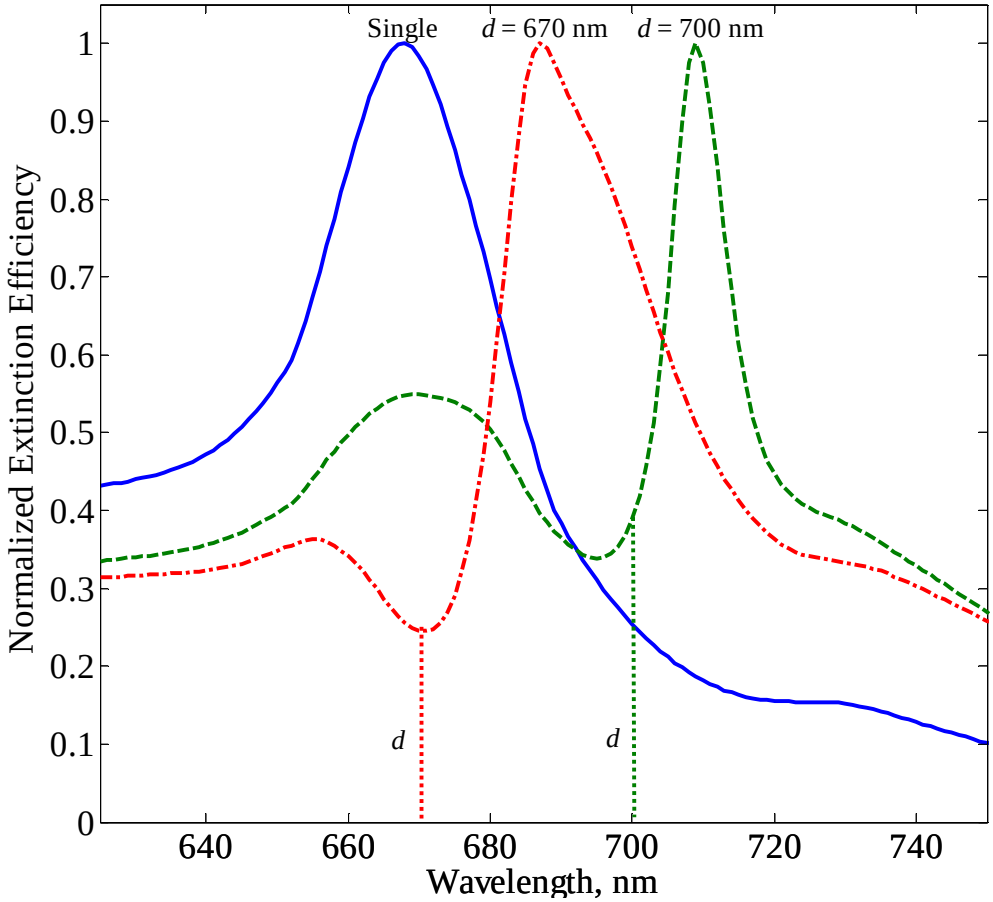

FIGURE 5.12: Destructive peak interference resulting in narrowed plasmon peak FWHM. Spectra represent (from left to right) single (blue), 670 nm (red), and 700 nm (green) inter-particle spacing for a r_{in} = 25 nm, t = 10 nm nanoring. Lines have been drawn in at the inter-particle spacing to guide the eye.

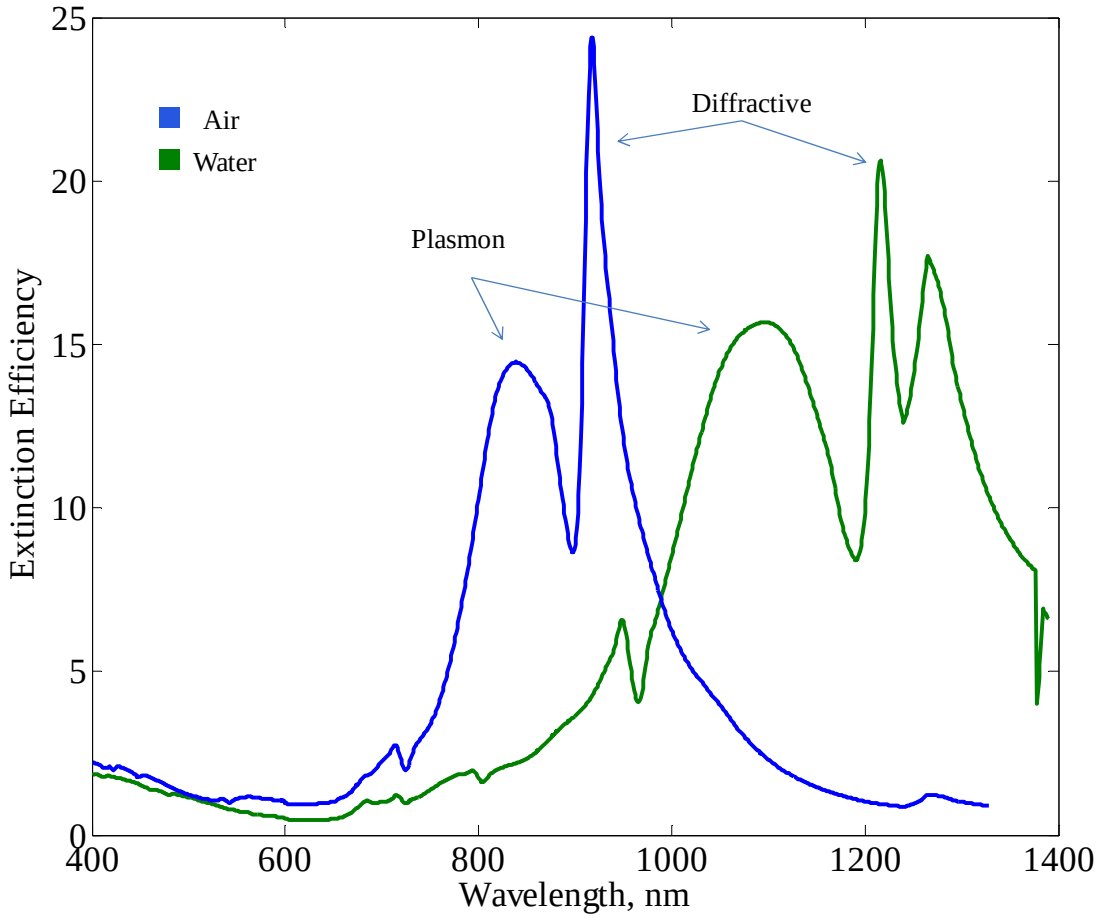

FIGURE 5.13: Simulated spectral response for a nanoring array to a refractive index change from 1 (vacuum) to 1.33 (water). Nanoring properties: r_{in} = 60 nm, t = 10 nm, and an inter-particle spacing of 900 nm.

CHAPTER 6

CONCLUDING REMARKS

6.1 IMPORTANCE OF WORK

Chemical sensing is a key component in modern society, especially in engineering applications. Because of their widespread impact, improvements to chemical sensors are a significant area of research. This work has demonstrated improved performance for refractive index nanoparticle sensors by arranging nanorings in periodic arrays to produce diffractive coupling sensors. The greatly improved figure of merit represents an advance in NP sensing technology that can be directly implemented in improving chemical sensors.

6.2 KEY FINDINGS

RI chemical sensing was achieved using ordered arrays of gold nanoparticles with cylindrical and spherical NP arrays. Sensitivity of these experimental sensors based on shifts from a methanol baseline was 88.5 and 198.6 nm/RIU, respectively. These sensitivity values were then directly compared to random NP LSPR sensors and were shown to have comparable or higher sensitivities than the representative LSPR sensors. The plasmon peak was also found to be enhanced in diffractive coupling sensors.

Nanorings were simulated based on their having the highest reported sensitivity and the increase in surface area. Simulations of rectangular arrays of nanorings for the inter-particle range from 500-1000 nm exhibited diffractive coupling for all nanoring sizes in this study. The diffractive peak was maximized relative to the single nanoring plasmon extinction for a nanoring with r_{in} = 60 nm, t = 10 nm, and an inter-particle spacing of 900 nm.

Sensing characteristics for this nanoring showed the diffractive coupling peak had a 15.9% higher sensitivity than the plasmon peak and comparable to the highest sensitivity reported in the literature for non-coupling nanorings. The figure of merit for this simulated nanoring sensor is the highest reported for plasmonic sensors at 34.

6.3 Ongoing and Future Work

6.3.1 Improvements in Nanoring Fabrication

Fabrication of NPs that closely match conditions in numerical simulations is important to identify the source of additional peaks observed in experimental diffractive coupling sensors.

Liftoff is an ongoing problem in the fabrication of patterned nanostructures. All metal deposition methods are known to have these problems. Current work is underway to make the surface of the electron resist resistant to EL plating using a chemical blocker. The hypothesis is that if the resist surface can be blocked before the pattern is developed, the EL plated gold will only form nanorings and not a film on top of the electron resist. This would eliminate the need for lift-off, leaving only the electron resist to be dissolved.

Work is also being done to characterize how chemical etching of the gold film might be used to improve lift-off. Initial experimental results suggest that gold on the surface of the electron resist is faster than etching of the NP. From these initial experiments it is also clear that etch rates for gold in non-patterned areas is faster than gold in patterned regions. If this method can be optimized, it could result in elimination of the gold liftoff step. Gold etching could also be tuned to achieve a desired nanoring thickness. A final benefit of this method could be in the removal of excess gold that penetrates through the electron resist near patterned features. As mentioned in 2.3.1.

6.3.2 RAPID ARRAY SIMULATION

Recent work by DeJarnette *et al.* suggests that the rsa-CDA could be modified with an effective polarizability for different shape factors to determine the optimal spacing for diffractive coupling in arrays of arbitrarily shaped NPs. Work is underway to create a polarizability model for nanorings based on polarizabilities calculated for the individual dipoles in nanorings simulated with DDSCAT. The dipole polarizabilities are not normally returned to the user in a useable format, but modifications to the program which allow these values to be output to a file have been implemented. It is believed this could be extended to any NP shape and composition, greatly improving the computation speed for NP arrays with square periodicity in the substrate plane.

6.3.3 NON-SENSING APPLICATIONS

Results for the larger nanorings showed that diffractive coupling can cause a broadband response in the near infrared region. This could be used to expand the effective window for energy conversion in photovoltaics past the band gap of silicon. Further work is required to determine what the optimal parameters are for generating this broadband feature. The reduced cross section of nanorings will allow most of the incident light to interact with the solar cell while absorbing NIR light and transferring the absorbed energy into the solar cell.

REFERENCES

(1) Kedem, O.; Tesler, A. B.; Vaskevich, A.; Rubinstein, I. Sensitivity and optimization of localized surface plasmon resonance transducers. *ACS nano* **2011**, 5, 748–60.

(2) Chen, H.; Kou, X.; Yang, Z.; Ni, W.; Wang, J. Shape- and size-dependent refractive index sensitivity of gold nanoparticles. *Langmuir* **2008**, 24, 5233–7.

(3) Sun, Y.; Xia, Y. Increased sensitivity of surface plasmon resonance of gold nanoshells compared to that of gold solid colloids in response to environmental changes. *Analytical chemistry* **2002**, 74, 5297–305.

(4) Okamoto, T.; Yamaguchi, I.; Kobayashi, T. Local plasmon sensor with gold colloid monolayers deposited upon glass substrates. *Optics letters* **2000**, 25, 372–4.

(5) Raschke, G.; Kowarik, S.; Franzl, T.; Sönnichsen, C.; Klar, T. A.; Feldmann, J.; Nichtl, A.; Kürzinger, K. Biomolecular Recognition Based on Single Gold Nanoparticle Light Scattering. *Nano Letters* **2003**, 3, 935–938.

(6) Raschke, G.; Brogl, S.; Susha, A. S.; Rogach, A. L.; Klar, T. A.; Feldmann, J.; Fieres, B.; Petkov, N.; Bein, T.; Nichtl, A.; Kürzinger, K. Gold Nanoshells Improve Single Nanoparticle Molecular Sensors. *Nano Letters* **2004**, 4, 1853–1857.

(7) Pedersen, D. B.; Duncan, E. J. S. *Surface Plasmon Resonance Spectroscopy of Gold Nanoparticle-Coated Substrates*; 2005; Vol. DRDC Suffi.

(8) Stetter, J. R.; Penrose, W. R.; Yao, S. Sensors , Chemical Sensors , Electrochemical Sensors , and ECS. *Journal of The Electrochemical Society* **2003**, 150, 11–16.

(9) Homola, J. Surface plasmon resonance sensors for detection of chemical and biological species. *Chemical reviews* **2008**, 108, 462–93.

(10) National Diabetes Statistics. *National Diabetes Information Clearinghouse* **2011**.

(11) Turner, C.; Walton, C.; Hoashi, S.; Evans, M. Breath acetone concentration decreases with blood glucose concentration in type I diabetes mellitus patients during hypoglycaemic clamps. *Journal of breath research* **2009**, 3, 046004.

(12) McFarland, A. D.; Duyne, R. P. Van Single Silver Nanoparticles as Real-Time Optical Sensors with Zeptomole Sensitivity. *Nano Letters* **2003**, 3, 1057–1062.

(13) Ho, C. K.; Itamura, M. T.; Kelley, M.; Hughes, R. C. *Review of Chemical Sensors for In-Situ Monitoring of Volatile Contaminants*; Albuquerque, NM, 2001; p. 34.

(14) Hübert, T.; Boon-Brett, L.; Black, G.; Banach, U. Hydrogen sensors – A review. *Sensors and Actuators B: Chemical* **2011**, 157, 329–352.

(15) Zhang, J.; Atay, T.; Nurmikko, A. V Optical detection of brain cell activity using plasmonic gold nanoparticles. *Nano letters* **2009**, 9, 519–24.

(16) Stuart, D. A.; Yuen, J. M.; Shah, N.; Lyandres, O.; Yonzon, C. R.; Glucksberg, M. R.; Walsh, J. T.; Duyne, R. P. Van In vivo glucose measurement by surface-enhanced Raman spectroscopy. *Analytical chemistry* **2006**, 78, 7211–5.

(17) Peng, G.; Tisch, U.; Adams, O.; Hakim, M.; Shehada, N.; Broza, Y. Y.; Billan, S.; Abdah-Bortnyak, R.; Kuten, A.; Haick, H. Diagnosing lung cancer in exhaled breath using gold nanoparticles. *Nature nanotechnology* **2009**, 4, 669–73.

(18) Shan, X.; Foley, K. J.; Tao, N. A label-free optical detection method for biosensors and microfluidics. *Applied Physics Letters* **2008**, 92, 133901.

(19) Akimov, Y. A.; Ostrikov, K.; Li, E. P. Surface Plasmon Enhancement of Optical Absorption in Thin-Film Silicon Solar Cells. *Plasmonics* **2009**, 4, 107–113.

(20) Mokkapati, S.; Beck, F. J.; Polman, a.; Catchpole, K. R. Designing periodic arrays of metal nanoparticles for light-trapping applications in solar cells. *Applied Physics Letters* **2009**, 95, 053115.

(21) Spinelli, P.; Hebbink, M.; Waele, R. de; Black, L.; Lenzmann, F.; Polman, A. Optical impedance matching using coupled plasmonic nanoparticle arrays. *Nano letters* **2011**, 11, 1760–5.

(22) Russell, A. G. Plasmonic Pervaporation via Gold Nanoparticle-functionalized Nanocomposite Membranes, University of Arkansas, 2012, p. 96.

(23) Singh, D.; Routbort, J.; Yu, W.; Timofeeva, E.; Smith, D. S.; France, D. M.; Heifetz, A. Heat transfer fluids containing nanoparticles **2011**, 33.

(24) Stewart, M. E.; Anderton, C. R.; Thompson, L. B.; Maria, J.; Gray, S. K.; Rogers, J. A.; Nuzzo, R. G. Nanostructured plasmonic sensors. *Chemical reviews* **2008**, 108, 494–521.

(25) Anker, J. N.; Hall, W. P.; Lyandres, O.; Shah, N. C.; Zhao, J.; Duyne, R. P. Van Biosensing with plasmonic nanosensors. *Nature materials* **2008**, 7, 442–53.

(26) Stuart, D. A. Refractive-index-sensitive, plasmon-resonant-scattering, and surface-enhanced Raman-scattering nanoparticles and arrays as biological sensing platforms. *Proceedings of SPIE* **2004**, 5327, 60–73.

(27) Willets, K. A.; Duyne, R. P. Van Localized surface plasmon resonance spectroscopy and sensing. *Annual review of physical chemistry* **2007**, 58, 267–97.

(28) Otte, M. A.; Sepúlveda, B.; Ni, W.; Juste, J. P.; Liz-Marzán, L. M.; Lechuga, L. M. Identification of the optimal spectral region for plasmonic and nanoplasmonic sensing. *ACS nano* **2010**, 4, 349–57.

(29) Simsek, E. On the Surface Plasmon Resonance Modes of Metal Nanoparticle Chains and Arrays. *Plasmonics* **2009**, 4, 223–230.

(30) Gao, S.; Koshizaki, N.; Tokuhisa, H.; Koyama, E.; Sasaki, T.; Kim, J.-K.; Ryu, J.; Kim, D.-S.; Shimizu, Y. Highly Stable Au Nanoparticles with Tunable Spacing and Their Potential Application in Surface Plasmon Resonance Biosensors. *Advanced Functional Materials* **2010**, 20, 78–86.

(31) Jensen, T. R.; Duval, M. L.; Kelly, K. L.; Lazarides, A. A.; Schatz, G. C.; Duyne, R. P. Van Nanosphere Lithography: Effect of the External Dielectric Medium on the Surface Plasmon Resonance Spectrum of a Periodic Array of Silver Nanoparticles. *The Journal of Physical Chemistry B* **1999**, 103, 9846–9853.

(32) Roper, D. K.; Ahn, W.; Taylor, B.; Dall'Asén, A. G. Enhanced Spectral Sensing by Electromagnetic Coupling With Localized Surface Plasmons on Subwavelength Structures. *IEEE Sensors Journal* **2010**, 10, 531–540.

(33) Stuart, D. A.; Haes, A. J.; Yonzon, C. R.; Hicks, E. M.; Duyne, R. P. Van Biological applications of localised surface plasmonic phenomenae. *IEE proceedings. Nanobiotechnology* **2005**, 152, 13–32.

(34) Otto, A. Excitation of nonradiative surface plasma waves in silver by the method of frustrated total reflection. *Zeitschrift für Physik* **1968**, 410, 398–410.

(35) Kretschmann, E.; Kröger, E. Reflection and transmission of light by a rough surface, including results for surface-plasmon effects. *Journal of the Optical Society of America* **1975**, 65, 150.

(36) Barnes, W. L. Comparing experiment and theory in plasmonics. *Journal of Optics A: Pure and Applied Optics* **2009**, 11, 114002.

(37) Bertucci, C.; Piccoli, A.; Pistolozzi, M. Optical biosensors as a tool for early determination of absorption and distribution parameters of lead candidates and drugs. *Combinatorial chemistry & high throughput screening* **2007**, 10, 433–40.

(38) Subramanian, A.; Irudayaraj, J. Surface plasmon resonance based immunosensing of E. coli O157: H7 in apple juice. *Trans. ASABE* **2006**, 49, 1257–1262.

(39) Grimault, A.-S.; Vial, A.; Grand, J.; Lamy de la Chapelle, M. Modelling of the near-field of metallic nanoparticle gratings: localized surface plasmon resonance and SERS applications. *Journal of microscopy* **2008**, 229, 428–32.

(40) Gunnarsson, L.; Rindzevicius, T.; Prikulis, J.; Kasemo, B.; Käll, M.; Zou, S.; Schatz, G. C. Confined plasmons in nanofabricated single silver particle pairs: experimental observations of strong interparticle interactions. *The Journal of Physical Chemistry B* **2005**, 109, 1079–87.

(41) Félidj, N.; Grand, J.; Laurent, G.; Aubard, J.; Lévi, G.; Hohenau, A.; Galler, N.; Aussenegg, F. R.; Krenn, J. R. Multipolar surface plasmon peaks on gold nanotriangles. *The Journal of Chemical Physics* **2008**, 128, 094702.

(42) Grand, J.; Adam, P.-M.; Grimault, A.-S.; Vial, A.; Lamy de la Chapelle, M.; Bijeon, J.-L.; Kostcheev, S.; Royer, P. Optical Extinction Spectroscopy of Oblate, Prolate and Ellipsoid Shaped Gold Nanoparticles: Experiments and Theory. *Plasmonics* **2006**, 1, 135–140.

(43) Kreno, L. E.; Hupp, J. T.; Duyne, R. P. Van Metal-organic framework thin film for enhanced localized surface plasmon resonance gas sensing. *Analytical chemistry* **2010**, 82, 8042–6.

(44) Ekinci, Y.; Christ, A.; Agio, M.; Martin, O. J. F.; Solak, H. H.; Löffler, J. F. Electric and magnetic resonances in arrays of coupled gold nanoparticle in-tandem pairs. *Optics express* **2008**, 16, 13287–95.

(45) Chan, G. H.; Zhao, J.; Schatz, G. C.; Duyne, R. P. Van Localized Surface Plasmon Resonance Spectroscopy of Triangular Aluminum Nanoparticles. *Journal of Physical Chemistry C* **2008**, 112, 13958–13963.

(46) Lee, K.-S.; El-Sayed, M. A. Gold and silver nanoparticles in sensing and imaging: sensitivity of plasmon response to size, shape, and metal composition. *The Journal of Physical Chemistry B* **2006**, 110, 19220–5.

(47) Chan, G. H.; Zhao, J.; Hicks, E. M.; Schatz, G. C.; Duyne, R. P. Van Plasmonic Properties of Copper Nanoparticles Fabricated by Nanosphere Lithography. *Nano Letters* **2007**, 7, 1947–1952.

(48) Kanehara, M.; Koike, H.; Yoshinaga, T.; Teranishi, T. Indium tin oxide nanoparticles with compositionally tunable surface plasmon resonance frequencies in the near-IR region. *Journal of the American Chemical Society* **2009**, 131, 17736–7.

(49) Hsiao, F.; Lee, C. Computational Study of Photonic Crystals Nano-Ring Resonator for Biochemical Sensing. *IEEE Sensors Journal* **2010**, 10, 1185–1191.

(50) Rechberger, W.; Hohenau, A.; Leitner, A.; Krenn, J. R.; Lamprecht, B.; Aussenegg, F. R. Optical properties of two interacting gold nanoparticles. *Optics Communications* **2003**, 220, 137–141.

(51) Su, K.-H.; Wei, Q.-H.; Zhang, X.; Mock, J. J.; Smith, D. R.; Schultz, S. Interparticle Coupling Effects on Plasmon Resonances of Nanogold Particles. *Nano Letters* **2003**, 3, 1087–1090.

(52) Ahn, W.; Roper, D. K. Transformed Gold Island Film Improves Light-to-Heat Transduction of Nanoparticles on Silica Capillaries. *Journal of Physical Chemistry C* **2008**, 112, 12214–12218.

(53) Nath, N.; Chilkoti, A. A colorimetric gold nanoparticle sensor to interrogate biomolecular interactions in real time on a surface. *Analytical chemistry* **2002**, 74, 504–9.

(54) Hanarp, P.; Käll, M.; Sutherland, D. S. Optical Properties of Short Range Ordered Arrays of Nanometer Gold Disks Prepared by Colloidal Lithography. *The Journal of Physical Chemistry B* **2003**, 107, 5768–5772.

(55) Sannomiya, T.; Sahoo, P. K.; Mahcicek, D. I.; Solak, H. H.; Hafner, C.; Grieshaber, D.; Vörös, J. Biosensing by densely packed and optically coupled plasmonic particle arrays. *Small* **2009**, 5, 1889–96.

(56) Lee, K.; Irudayaraj, J. Periodic and Dynamic 3-D Gold Nanoparticle−DNA Network Structures for Surface-Enhanced Raman Spectroscopy-Based Quantification. *The Journal of Physical Chemistry C* **2009**, 113, 5980–5983.

(57) Félidj, N.; Aubard, J.; Lévi, G.; Krenn, J. R.; Hohenau, A.; Schider, G.; Leitner, A.; Aussenegg, F. R. Optimized surface-enhanced Raman scattering on gold nanoparticle arrays. *Applied Physics Letters* **2003**, 82, 3095.

(58) Ru, E. C. Le; Etchegoin, P. G.; Meyer, M. Enhancement factor distribution around a single surface-enhanced Raman scattering hot spot and its relation to single molecule detection. *The Journal of chemical physics* **2006**, 125, 204701.

(59) Hicks, E. M.; Zou, S.; Schatz, G. C.; Spears, K. G.; Duyne, R. P. Van; Gunnarsson, L.; Rindzevicius, T.; Kasemo, B.; Käll, M. Controlling plasmon line shapes through diffractive coupling in linear arrays of cylindrical nanoparticles fabricated by electron beam lithography. *Nano letters* **2005**, 5, 1065–70.

(60) Auguié, B.; Barnes, W. Collective Resonances in Gold Nanoparticle Arrays. *Physical Review Letters* **2008**, 101, 1–4.

(61) Vecchi, G.; Giannini, V.; Gómez Rivas, J. Surface modes in plasmonic crystals induced by diffractive coupling of nanoantennas. *Physical Review B* **2009**, 80, 1–4.

(62) DeJarnette, D.; Roper, D. K.; Harbin, B. Geometric effects on far-field coupling between multipoles of nanoparticles in square arrays. *Journal of the Optical Society of America B* **2011**, 29, 88–100.

(63) Larsson, E. M.; Alegret, J.; Käll, M.; Sutherland, D. S. Sensing characteristics of NIR localized surface plasmon resonances in gold nanorings for application as ultrasensitive biosensors. *Nano letters* **2007**, 7, 1256–63.

(64) Mayer, K. M.; Hafner, J. H. Localized surface plasmon resonance sensors. *Chemical reviews* **2011**, 111, 3828–57.

(65) Sherry, L. J.; Chang, S.-H.; Schatz, G. C.; Duyne, R. P. Van; Wiley, B. J.; Xia, Y. Localized surface plasmon resonance spectroscopy of single silver nanocubes. *Nano letters* **2005**, 5, 2034–8.

(66) Dmitriev, A.; Hägglund, C.; Chen, S.; Fredriksson, H.; Pakizeh, T.; Käll, M.; Sutherland, D. S. Enhanced nanoplasmonic optical sensors with reduced substrate effect. *Nano letters* **2008**, 8, 3893–8.

(67) Chen, H.; Kou, X.; Yang, Z.; Ni, W.; Wang, J. Shape- and size-dependent refractive index sensitivity of gold nanoparticles. *Langmuir* **2008**, 24, 5233–7.

(68) Nehl, C. L.; Liao, H.; Hafner, J. H. Optical properties of star-shaped gold nanoparticles. *Nano letters* **2006**, 6, 683–8.

(69) Kosiorek, A.; Kandulski, W.; Glaczynska, H.; Giersig, M. Fabrication of nanoscale rings, dots, and rods by combining shadow nanosphere lithography and annealed polystyrene nanosphere masks. *Small (Weinheim an der Bergstrasse, Germany)* **2005**, 1, 439–44.

(70) Zhu, S.; Li, F.; Du, C.; Fu, Y. A localized surface plasmon resonance nanosensor based on rhombic Ag nanoparticle array. *Sensors and Actuators B: Chemical* **2008**, 134, 193–198.

(71) Heidenreich, R. D.; Thompson, L. F.; Feit, E. D.; Melliar-Smith, C. M. Fundamental aspects of electron beam lithography. I. Depth-dose response of polymeric electron beam resists. *Journal of Applied Physics* **1973**, 44, 4039.

(72) Sepúlveda, B.; Angelomé, P. C.; Lechuga, L. M.; Liz-Marzán, L. M. LSPR-based nanobiosensors. *Nano Today* **2009**, 4, 244–251.

(73) Djenizian, T.; Schmuki, P. Electron beam lithographic techniques and electrochemical reactions for the micro- and nanostructuring of surfaces under extreme conditions. *Journal of Electroceramics* **2006**, 16, 9–14.

(74) Ahn, W.; Taylor, B.; Dall'Asén, A. G.; Roper, D. K. Electroless gold island thin films: photoluminescence and thermal transformation to nanoparticle ensembles. *Langmuir* **2008**, 24, 4174–84.

(75) Blake, P.; Ahn, W.; Roper, D. K. Enhanced uniformity in arrays of electroless plated spherical gold nanoparticles using tin presensitization. *Langmuir* **2010**, 26, 1533–8.

(76) Ahn, W.; Blake, P.; Shultz, J.; Ware, M. E.; Roper, D. K. Fabrication of regular arrays of gold nanospheres by thermal transformation of electroless-plated films. *Journal of Vacuum Science & Technology B: Microelectronics and Nanometer Structures* **2010**, 28, 638.

(77) Jang, G.-G.; Roper, D. K. Continuous Flow Electroless Plating Enhances Optical Features of Au Films and Nanoparticles. *Journal of Physical Chemistry C* **2009**, 113, 19228–19236.

(78) Shi, J.; Chen, J.; Decanini, D.; Chen, Y.; Haghiri-Gosnet, A.-M. Fabrication of metallic nanocavities by soft UV nanoimprint lithography. *Microelectronic Engineering* **2009**, 86, 596–599.

(79) Teo, S. L.; Lin, V. K.; Marty, R.; Large, N.; Llado, E. A.; Arbouet, A.; Girard, C.; Aizpurua, J.; Tripathy, S.; Mlayah, A. Gold nanoring trimers: a versatile structure for infrared sensing. *Optics express* **2010**, 18, 22271–82.

(80) Almeida-Prieto, S.; Blanco-Méndez, J.; Otero-Espinar, F. J. Image analysis of the shape of granulated powder grains. *Journal of pharmaceutical sciences* **2004**, 93, 621–34.

(81) Xu, Z.; Shilpiekandula, V.; Youcef-toumi, K.; Yoon, S. F. White-light scanning interferometer for absolute nano-scale gap thickness measurement. *Optics express* **2009**, 17, 15104–17.

(82) Dean, J. A. Dean, J. A., Ed.; McGraw-Hill, 1999; pp. 1.211,1.255, 1.302.

(83) Lee, J. N.; Park, C.; Whitesides, G. M. Solvent compatibility of poly(dimethylsiloxane)-based microfluidic devices. *Analytical chemistry* **2003**, 75, 6544–54.

(84) Duyne, R. P. Van; Haes, A. J.; McFarland, A. D. In *Proceedings of SPIE*; Lian, T.; Dai, H.-L., Eds.; SPIE, 2003; Vol. 5223, pp. 197–207.

(85) Li, C.-T.; Chen, H.; Un, I.-W.; Lee, H.-C.; Yen, T.-J. Study of optical phase transduction on localized surface plasmon resonance for ultrasensitive detection. *Optics express* **2012**, 20, 3250–60.

(86) Nooke, A.; Beck, U.; Hertwig, A.; Krause, A.; Krüger, H.; Lohse, V.; Negendank, D.; Steinbach, J. On the application of gold based SPR sensors for the detection of hazardous gases. *Sensors and Actuators B: Chemical* **2010**, 149, 194–198.

(87) Sherry, L. J.; Jin, R.; Mirkin, C. A.; Schatz, G. C.; Duyne, R. P. Van Localized surface plasmon resonance spectroscopy of single silver triangular nanoprisms. *Nano letters* **2006**, 6, 2060–5.

(88) Lee, S.-W.; Lee, K.-S.; Ahn, J.; Lee, J.-J.; Kim, M.-G.; Shin, Y.-B. Highly sensitive biosensing using arrays of plasmonic Au nanodisks realized by nanoimprint lithography. *ACS nano* **2011**, 5, 897–904.

(89) Chen, C.-D.; Cheng, S.-F.; Chau, L.-K.; Wang, C. R. C. Sensing capability of the localized surface plasmon resonance of gold nanorods. *Biosensors & bioelectronics* **2007**, 22, 926–32.

(90) Blake, P.; Obermann, J.; Harbin, B.; Roper, D. K. Enhanced Nanoparticle Response From Coupled Dipole Excitation for Plasmon Sensors. *IEEE Sensors Journal* **2011**, 11, 3332–3340.

(91) Zhao, J.; Pinchuk, A. O.; McMahon, J. M.; Li, S.; Ausman, L. K.; Atkinson, A. L.; Schatz, G. C. Methods for describing the electromagnetic properties of silver and gold nanoparticles. *Accounts of chemical research* **2008**, 41, 1710–20.

(92) Curry, A.; Nusz, G.; Chilkoti, A.; Wax, A. Substrate effect on refractive index dependence of plasmon resonance for individual silver nanoparticles observed using darkfield microspectroscopy. *Optics Express* **2005**, 13, 2668.

(93) Yang, T.; Crozier, K. B. Dispersion and extinction of surface plasmons in an array of gold nanoparticle chains: influence of the air/glass interface. *Optics Express* **2008**, 16, 8570–8580.

(94) Mie, G. Contributions on the Optics of Turbid Media, Particularly Colloidal Metal Solutions. *Annalen der Physik* **1908**, 25, 377–445.

(95) Bohren, C. F.; Huffman, D. R. *Absorption and Scattering of Light by Small Particles*; Bohren, C. F.; Huffman, D. R., Eds.; Wiley-VCH Verlag GmbH: Weinheim, Germany, 1998.

(96) Mätzler, C. *MATLAB functions for Mie scattering and absorption*; Bern, Switzerland, 2002; Vol. 199.

(97) Yee, K. S. Numerical solution of initial boundary value problems involving maxwell's equations in isotropic media. *IEEE Transactions on Antennas and Propagation* **1966**, 14, 302–307.

(98) Miller, M. M.; Lazarides, A. A. Sensitivity of metal nanoparticle surface plasmon resonance to the dielectric environment. *The Journal of Physical Chemistry B* **2005**, 109, 21556–65.

(99) Purcell, E. M.; Pennypacker, C. R. Scattering and Absorption of Light by Nonspherical Dielectric Grains. *The Astrophysical Journal* **1973**, 186, 705–714.

(100) Draine, B. T.; Flatau, P. J. Discrete-dipole approximation for scattering calculations. *Journal of the Optical Society of America A* **1994**, 11, 1491.

(101) Draine, B. T.; Flatau, P. J. Discrete-dipole approximation for periodic targets: theory and tests. *Journal of the Optical Society of America A* **2008**, 25, 2693–2703.

(102) Draine, B. User Guide for the Discrete Dipole Approximation Code DDSCAT 7.1. *Arxiv preprint arXiv:1002.1505* **2010**, 1, 83.

(103) Yurkin, M. A.; Hoekstra, A. G.; Brock, R. S.; Lu, J. Q. Systematic comparison of the discrete dipole approximation and the finite difference time domain method for large dielectric scatterers. *Optics express* **2007**, 15, 17902–11.

(104) Lee, H.; You, S.; Pikhitsa, P. V; Kim, J.; Kwon, S.; Woo, C. G.; Choi, M. Three-dimensional assembly of nanoparticles from charged aerosols. *Nano letters* **2011**, 11, 119–24.

(105) Coluccio, M. L.; Das, G.; Mecarini, F.; Gentile, F.; Pujia, A.; Bava, L.; Tallerico, R.; Candeloro, P.; Liberale, C.; Angelis, F. De; Fabrizio, E. Di Silver-based surface enhanced Raman scattering (SERS) substrate fabrication using nanolithography and site selective electroless deposition. *Microelectronic Engineering* **2009**, 86, 1085–1088.

(106) Jain, P. K.; Huang, X.; El-Sayed, I. H.; El-Sayed, M. a. Review of Some Interesting Surface Plasmon Resonance-enhanced Properties of Noble Metal Nanoparticles and Their Applications to Biosystems. *Plasmonics* **2007**, 2, 107–118.

(107) Bechelany, M.; Brodard, P.; Philippe, L.; Michler, J. Extended domains of organized nanorings of silver grains as surface-enhanced Raman scattering sensors for molecular detection. *Nanotechnology* **2009**, 20, 455302.

(108) Haes, A. J.; Duyne, R. P. Van A Highly Sensitive and Selective Surface-Enhanced Nanobiosensor. *Mat. Res. Soc. Symp. Proc.* **2002**, 723, O3.1.1–O3.1.6.

(109) Stiles, P. L.; Dieringer, J. A.; Shah, N. C.; Duyne, R. P. Van Surface-Enhanced Raman Spectroscopy. *Annual Review of Analytical Chemistry (2008)* **2008**, 1, 601–626.

(110) Félidj, N.; Laurent, G.; Aubard, J.; Lévi, G.; Hohenau, A.; Krenn, J. R.; Aussenegg, F. R. Grating-induced plasmon mode in gold nanoparticle arrays. *The Journal of chemical physics* **2005**, 123, 221103.

(111) Evlyukhin, A.; Reinhardt, C.; Seidel, A.; Luk'yanchuk, B.; Chichkov, B. Optical response features of Si-nanoparticle arrays. *Physical Review B* **2010**, 82, 1–12.

(112) Auguié, B.; Barnes, W. L. Diffractive coupling in gold nanoparticle arrays and the effect of disorder. *Optics letters* **2009**, 34, 401–3.

(113) Sung, J.; Hicks, E. M.; Duyne, R. P. Van; Spears, K. G. Nanoparticle Spectroscopy: Dipole Coupling in Two-Dimensional Arrays of L-Shaped Silver Nanoparticles. *Journal of Physical Chemistry C* **2007**, 111, 10368–10376.

(114) Linden, S.; Christ, A.; Kuhl, J.; Giessen, H. Selective suppression of extinction within the plasmon resonance of gold nanoparticles. *Applied Physics B: Lasers and Optics* **2001**, 73, 311–316.

(115) Canfield, B. K.; Kujala, S.; Kauranen, M.; Jefimovs, K.; Vallius, T.; Turunen, J. Remarkable polarization sensitivity of gold nanoparticle arrays. *Applied Physics Letters* **2005**, 86, 183109.

(116) Orendorff, C. J.; Sau, T. K.; Murphy, C. J. Shape-dependent plasmon-resonant gold nanoparticles. *Small* **2006**, 2, 636–9.

(117) Offermans, P.; Schaafsma, M. C.; Rodriguez, S. R. K.; Zhang, Y.; Crego-Calama, M.; Brongersma, S. H.; Gómez Rivas, J. Universal scaling of the figure of merit of plasmonic sensors. *ACS nano* **2011**, 5, 5151–7.

(118) Thirstrup, C.; Zong, W. Data analysis for surface plasmon resonance sensors using dynamic baseline algorithm. *Sensors and Actuators B: Chemical* **2005**, 106, 796–802.

(119) Tsai, C.-Y.; Lu, S.-P.; Lin, J.-W.; Lee, P.-T. High sensitivity plasmonic index sensor using slablike gold nanoring arrays. *Applied physics letters* **2011**, 98, 153108.

(120) Baida, H.; Berthelot, A.; Crut, A.; Maioli, P.; Fatti, N. Del; Vallée, F. Spectroscopy and electron microscopy imaging of a single metal nano-object. *Advances in Natural Sciences: Nanoscience and Nanotechnology* **2012**, 3, 015003.

(121) Kang, Z.; Zhang, H.; Lu, H.; Xu, J.; Ong, H.-C.; Shum, P.; Ho, H.-P. Plasmonic optical trap having very large active volume realized with nano-ring structure. *Optics letters* **2012**, 37, 1748–50.

(122) Banaee, M. G.; Crozier, K. B. Gold nanorings as substrates for surface-enhanced Raman scattering. *Optics letters* **2010**, 35, 760–2.

(123) Huang, C.; Ye, J.; Wang, S.; Stakenborg, T.; Lagae, L. Gold nanoring as a sensitive plasmonic biosensor for on-chip DNA detection. *Applied Physics Letters* **2012**, 100, 173114.

(124) Mary, A.; Koller, D.; Hohenau, A.; Krenn, J.; Bouhelier, A.; Dereux, A. Optical absorption of torus-shaped metal nanoparticles in the visible range. *Physical Review B* **2007**, 76, 1–5.

(125) Aizpurua, J.; Hanarp, P.; Sutherland, D.; Käll, M.; Bryant, G.; García de Abajo, F. Optical Properties of Gold Nanorings. *Physical Review Letters* **2003**, 90, 5–8.

(126) Aswathy, R. G.; Yoshida, Y.; Maekawa, T.; Kumar, D. S. Near-infrared quantum dots for deep tissue imaging. *Analytical and bioanalytical chemistry* **2010**, 397, 1417–35.

(127) Kennedy, J. *A Fast Bresenham Type Algorithm For Drawing Circles*; Santa Monica, CA, 2012; pp. 1–9.

(128) Yurkin, M. A.; Kanter, D. de; Hoekstra, A. G. Accuracy of the discrete dipole approximation for simulation of optical properties of gold nanoparticles. *Journal of Nanophotonics* **2010**, 4, 041585.

(129) Lynch, D. W.; Hunter, W. R. *Handbook of optical constants of solids*; Palik, E. D., Ed.; Elsevier: San Diego, CA, USA, 1998; pp. 286–295.

(130) Johnson, P. B.; Christy, R. W. Optical Constants of the Noble Metals. *Physical Review B* **1972**, 6, 4370–4379.

(131) Ungureanu, C.; Rayavarapu, R. G.; Manohar, S.; Leeuwen, T. G. van Discrete dipole approximation simulations of gold nanorod optical properties: Choice of input parameters and comparison with experiment. *Journal of Applied Physics* **2009**, 105, 102032.

(132) Link, S.; El-Sayed, M. A. Size and Temperature Dependence of the Plasmon Absorption of Colloidal Gold Nanoparticles. *The Journal of Physical Chemistry B* **1999**, 103, 4212–4217.

(133) Liu, S. D.; Zhang, Z. S.; Wang, Q. Q. High sensitivity and large field enhancement of symmetry broken Au nanorings: effect of multipolar plasmon resonance and propagation. *Optics express* **2009**, 17, 2906–17.

(134) Aizpurua, J.; Blanco, L.; Hanarp, P.; Sutherland, D.; Kall, M.; Bryant, G.; Garcia de Abajo, F. Light scattering in gold nanorings. *Journal of Quantitative Spectroscopy and Radiative Transfer* **2004**, 89, 11–16.

(135) Link, S.; Burda, C.; Wang, Z. L.; El-Sayed, M. A. Electron dynamics in gold and gold–silver alloy nanoparticles: The influence of a nonequilibrium electron distribution and the size dependence of the electron–phonon relaxation. *The Journal of Chemical Physics* **1999**, 111, 1255.

(136) Zhang, J. Z. *Optical Properties and Spectroscopy of Nanomaterials*; World Scientific Publishing Co.: Hackensack, NJ, 2009; p. 209.

(137) Hao, F.; Larsson, E. M.; Ali, T. A.; Sutherland, D. S.; Nordlander, P. Shedding light on dark plasmons in gold nanorings. *Chemical Physics Letters* **2008**, 458, 262–266.

(138) Tseng, H.-Y.; Lee, C.-K.; Wu, S.-Y.; Chi, T.-T.; Yang, K.-M.; Wang, J.-Y.; Kiang, Y.-W.; Yang, C. C.; Tsai, M.-T.; Wu, Y.-C.; Chou, H.-Y. E.; Chiang, C.-P. Au nanorings for enhancing absorption and backscattering monitored with optical coherence tomography. *Nanotechnology* **2010**, 21, 295102.

APPENDIX A

MATLAB PROGRAMS

A.1 SEM NANOPARTICLE ANALYSIS CODE

```
function [measure] =measureaunp1(pic,px,lsb)
%%%%%%%%
%   pic is the file path and file name or a previously imported image
%   px is the number of pixels in the scalebar
%   lsb is the length of the scale bar in nm
%   Acceptable input formats:
%      measure=measureaunp1(pic)
%           where pic is either a path and filename or a previously imported image variable
%       measure=measureaunp1(pic,h)
%           where pic is a previously imported image and
%                    h is the tiff header info retrieved by h=imfinfo('filepath\filename')
%       measure=measureaunp(pic,px,lsb)
%
%   Output is saved in a structure format

format compact

switch nargin
    case 1
        %  check to see if the picture is a path or a variable
        if ischar(pic)
            h=imfinfo(pic);
            pic=imread(pic);
        else
            h=[];
        end
        pic=px_square(pic,h);

    case 2
        h=px;
        clear px;
    case 3
        if ischar(pic)
            h=imfinfo(pic);
            pic=imread(pic);
        else
            h=[];
        end
    otherwise
        error('Incorrect input')
end

if ~exist('px','var')||~exist('lsb','var')
    [ppnm lsb px]=wantscale(pic);
end
% check to see in pixels per nanometer has been calculated yet
```

```
if ~exist('ppnm','var')
   ppnm=px/lsb; %%number of pixels per nanometer
end

cutoff=findaunp(pic,50,250);
close all;
pic2=edgeaunp(pic,cutoff);
close all;
picd=size(pic2);
pic1=pic(1:picd(1),1:picd(2),1);
[L,npar]=bwlabel(pic2);
a=size(pic2);
% B=bwboundaries(pic2,'noholes');
% need to fix....%%%%%%%%%%%%%%%%%%%%%%%%%%%%%%%%%%%%%%%%%%%%%%%%%%%%%%%%%%%%%%%%
area=a(1)*a(2); %%area in nm^2
pdens=npar/area; %particles per nm^2

auprops=regionprops(L,'EquivDiameter','centroid','Area','Perimeter','ConvexImage','MajorAxisLength','MinorAxisL
ength');
perimeter=cat(1,auprops.Perimeter)';
measure.perimeter=perimeter;
auprops2=regionprops(bwperim(L),'PixelList');
for j=1:npar
   ri=zeros(npar,1);
for i=1:length(auprops2(j).PixelList)
   ri(i)=sqrt((auprops2(j).PixelList(i,1)-auprops(j).Centroid(1)).^2+(auprops2(j).PixelList(i,2)-
auprops(j).Centroid(2)).^2);
end
% measure.ri(j)=ri;
ri;
rm=sum(ri)/length(ri);
vr=sum(abs(ri-rm)./rm*100)/length(ri);
measure.Vr(j)=vr;
vp=abs(2*pi*rm-perimeter(j))./(2*pi*rm)*100;
measure.Vp(j)=vp;
end
% for i=1:length(B)
%    boundary=B{i};
%    delta_sq=diff(boundary).^2;
%    perimeter(i)=sum(sqrt(sum(delta_sq,2)));
% end

auArea=cat(1,auprops.Area)';
measure.area=auArea;
circularity=4*pi*auArea./(perimeter).^2;

convex=auprops.ConvexImage;
for i=1:length(auprops)
   convex=auprops(i).ConvexImage;
   c3=regionprops(convex,'Perimeter')';
   convperim(i)=c3.Perimeter';
end
convexity=convperim./perimeter;
```

```
Maxis=cat(1,auprops.MajorAxisLength)';
maxis=cat(1,auprops.MinorAxisLength)';
elongation=(1-maxis./Maxis);

measure.circularity=circularity;
measure.convexity=convexity;
measure.elongation=elongation;


pdia=cat(1,auprops.EquivDiameter)';
pdist=cat(1,auprops.Centroid);

overlay1 = imoverlay(pic1,pic2,[.3 .3 1]);

pic4=uint8(zeros(size(pic2)));

% scrsz = get(0,'ScreenSize');
% figure('Position',[1 1 scrsz(3) scrsz(4)])
% imshow(pic4)
dist=zeros(npar);
for k=1:size(pdist,1)
      x0=pdist(k,1);
      y0=pdist(k,2);
      pic4(round(y0)-1:round(y0)+1,round(x0)-1:round(x0)+1)=254;
%       rectangle('Position',[round(x0),round(y0),1,1],'Curvature',[1 1],'EdgeColor',[.2,1,.2],'Linewidth',1)
      radius=pdia(k)/2;
      xpos=round(x0-radius);
      ypos=round(y0-radius);
      x0=x0./ppnm;
      y0=y0./ppnm;
%       rectangle('Position',[xpos,ypos,2*radius,2*radius],'Curvature',[1 1],'EdgeColor',[1,1,1],'Linewidth',1)
%       pause(.1)
   for j=1:size(pdist,1)
      if k~=j
      x1=pdist(j,1)./ppnm;
      y1=pdist(j,2)./ppnm;
%       line([y0 y1],[x0 x1])
%       pause(.01)
      dist(k,j)=sqrt((x0-x1).^2+(y0-y1).^2);

      else dist(k,j)=0;
      end
   end
end

% pic5=getframe;
% clf
% pic5=imresize(im2bw(pic5.cdata),size(pic4));
% pic5(1,:)=0; pic5(:,1)=0; pic5(:,size(pic5,2))=0; pic5(size(pic5,1),:)=0;
overlay1 = imoverlay(overlay1,logical(pic4),[.9 .3 .3]);
% overlay1=imoverlay(overlay1,logical(pic5),[.2,.9,.2]);
subplot(2,2,1)
imshow(overlay1)
%%% plots circle equivalent diameters around centroids
f=figure(2);
```

```
imshow(overlay1)
scrsz = get(0,'ScreenSize');
set(f,'Position',[1 1 scrsz(3) scrsz(4)])
for k=1:size(pdist,1)
   x0=pdist(k,1);
   y0=pdist(k,2);
   radius=pdia(k)/2;
   xpos=round(x0-radius);
   ypos=round(y0-radius);
   x0=x0./ppnm;
   y0=y0./ppnm;
   rectangle('Position',[xpos,ypos,2*radius,2*radius],'Curvature',[1 1],'EdgeColor',[.2,.9,.2],'Linewidth',2)
end

pic5=getframe;
% imwrite(pic5.cdata,'test1.png');
close(f)
figure(1)
pdia=pdia./ppnm;
pdist=dist;

%for non-regular arrays
% % % dist=mean(min(pdist>0));

%for square arrays with ~670 spacing
i=0;
clear dist;
%loop to avoid counting same distance twice for std dev
for j=1:npar
   for k=j:npar
      if (pdist(j,k) > 500) && (pdist(j,k) < 800)
         i=i+1;
         dist(i)=pdist(j,k);
      end
   end
end
if npar>1
distdev=std(dist);
dist=mean(dist);
else distdev=0; dist=0;
end

pdiaav=mean(pdia);
pdev=std(pdia);
if pdev<1/ppnm
   pdev=1/ppnm;
end
display((sprintf('Mean particle size %4.2f ± %2.2f nm', pdiaav,pdev)));
display((sprintf('Number of particles %d',npar)));
display((sprintf('%G particles/nm^2',pdens)));
% display(num2str(sprintf('%4.3f x-Pixels per nanometer\t%.3f y-Pixels per nanometer',xppnm, yppnm)));
display((sprintf('%4.3f Pixels per nanometer\tnanometers per pixel %.2f',ppnm,1/ppnm)));
display((sprintf('Average particle distance (center to center) %.2f ± %.2f nm',dist,distdev)));
% fprintf('Average eccentricity (0 is circle, 1 is straight line): %.2f ± %.2f\n',mean(eccent),std(eccent));
```

```
subplot(2,2,2)
vislabels(L);
measure.labels=L;
subplot(2,2,3:4)

bins=(max(pdia)-min(pdia))/std(pdia)*2;
hist(pdia,npar)
% [n xout]=hist(pdia,linspace(min(pdia)+bins/2,max(pdia)-bins/2,bins),round(bins));
% bar(xout,n,'r','barwidth',.95)
axis tight
% set(gca,'XTick',round([min(pdia) linspace(min(pdia)+bins,max(pdia)-bins,bins) max(pdia)]),'YTick',[0:max(n)])
measure.particleDensity=pdens;
measure.numParticle=npar;
measure.particleDistance=pdist;
measure.meandist=dist;
measure.particledistdev=distdev;
measure.overlay=overlay1;
measure.pixelpernm=ppnm;
measure.particlediameter=pdia;
measure.meanpdia=pdiaav;
measure.pdiadev=pdev;
measure.nmperpixel=1/ppnm;
measure.lsb=lsb;
measure.lsb_pixels=px;
end


function [ppnm lsb px]=findscale(pic)
% Calculates the scale bar length for SEM images
% with user input on the location of the scale bar
% pic is a picture imported into matlab
% lsb is the length of the scale bar in nm
% px is the number of pixels in the scale bar
% ppnm is the number of pixels per nanometer

% Display the image and ask for user to select top left and bottom right points
% to form a box around the scale bar
subplot(6,2,1:10)
imshow(pic)
title('Select 2 points at opposite corners around the scale bar')
again='y';
while again~='n'
   [x y]=ginput(2);
   scalebar=pic(floor(min(y):max(y)),floor(min(x):max(x)));
   % Display the selection
   subplot(6,2,11)
   imshow(scalebar)
   again=input('Do you want to re-select the scale bar?(y/n) ','s');
   switch again
      case {'n' 'N' 'No' 'no'}
         again='n';
      otherwise
         again='y';
   end
```

```
end
clear x y again
% make the scale bar a black/white image
scalebar=im2bw(scalebar);
lsb=0; % length of scale bar
while lsb==0
lsb=input('What is the length of the scale bar in nm? ');
if ~isfinite(lsb)
   lsb=0;
   display('Invalid input.  Try again')
end
end

% find the first column with a white pixel from the left
lhc=0;
while lhc==0
   for c1=1:size(scalebar,2)
      % if found, break from loop
      if sum(scalebar(:,c1))>=1
         lhc=c1;
         break
      end
   end
   if c1==size(scalebar,2)  % statement to avoid infinite loop
      lhc=1;
      display('Scalebar not found')
   end
end
% find the first column with a white pixel from the right
rhc=0;
while rhc==0
   for c2=size(scalebar,2):-1:1
      % if found, break from loop
      if sum(scalebar(:,c2))>=1
         rhc=c2;
         break
      end
   end
   if c2==1  % statement to avoid infinite loop
      rhc=size(scalebar,2);
      display('Scalebar not found')
   end
end

scalebar=scalebar(:,lhc:rhc);

% Show the located scale bar
subplot(6,2,12)
imshow(scalebar);
% calculate the length of the scalebar in pixels
px=abs(rhc-lhc)+1;
% calculate the number of pixels per nm
ppnm=px/lsb;
end
```

```
function aunppic=edgeaunp(pic,cutoff)
%%finds and marks the edges of gold np

figure(1)

picd=size(pic);
pic1=pic(1:(picd(1)-59),1:picd(2),1);

dimg=pic1(:,:,1);
dimg=double(dimg);
a_eq=adapthisteq(pic1(:,:,1));
dimg2=double(a_eq);


bwpic=dimg<cutoff;
bw2pic=dimg2<cutoff;
bw=imclearborder(~bwpic);
bw2=imclearborder(~bw2pic);
subplot(1,2,1)
imshow(bw)
subplot(1,2,2)
imshow(bw2)
pick=input('1, 2, or 3 if inverted:  ');
if pick==1
  bwa=imfill(bw,'holes');
%    bwa=bw;
end
if pick==2
   bwa=imfill(bw2,'holes');
%    bwa=bw2;
end
if pick==3
   bw=imclearborder(bwpic);
   bw2=imclearborder(bw2pic);
   subplot(1,2,1)
   imshow(bw)
   subplot(1,2,2)
   imshow(bw2)
   pick=input('1, 2:  ');
   if pick==1
     bwa=imfill(bw,'holes');
   %    bwa=bw;
   end
   if pick==2
      bwa=imfill(bw2,'holes');
   %    bwa=bw2;
   end
end
again='b';
j=5; l=40;
while again~='n'
 if (again~='b')
    j=input('Enter circle lim: ');

    l=input('Enter factor: ');
```

```
 end
bw3=bwa;
%bw3=bwmorph(bwa,'clean');
%bw3=bwmorph(bw3,'hbreak');
%bw3=bwmorph(bw3,'spur');
bw3=imfill(bw3,'holes');
bw3=bwmorph(bw3,'fill');
bwb=imopen(bw3, strel('disk',j));
bwc=bwareaopen(bwb,l);
bwc=bwb;
bwc_perim=bwperim(bwc);
overlay1 = imoverlay(pic1,bwc_perim,[.3 .3 1]);
figure(1)
pics={pic; bwa; bwb; bwc; bwc_perim; overlay1};
picslabel={'pic'; 'bwa'; 'bwb'; 'bwc'; 'bwc\_perim'; 'overlay1'};

for i=1:6
subplot(2,3,i)
ph=pics{i,1};
imshow(ph);
title(sprintf('%s',char(picslabel{i})));
end
again=input('Do you want to try again?(y/n): ','s');
end
aunppic=bwc;
end

function cutoff=findaunp(pic,cutofflow,cutoffhigh)

picd=size(pic);
pic1=pic(1:(picd(1)-59),1:picd(2),1);
dimg=pic1(:,:,1);
dimg=double(dimg);
%surf(dimg(:,:,1),'EdgeColor','none')
%figure(2);
a_eq=adapthisteq(pic1(:,:,1));
dimg2=double(a_eq);
%surf(dimg2(:,:,1),'EdgeColor','none')

again='b';
while again~='n'
 if (again~='b')
    cutofflow=input('Enter lower cutoff: ');
    cutoffhigh=input('Enter higher cutoff: ');
 end
 step=(cutoffhigh-cutofflow)/3;

 figure(3)
 for k=1:4
  j=cutofflow:step:cutoffhigh;
  subplot(2,2,k)
  partk=dimg<j(k);
  imshow(partk);
  title(num2str(sprintf('%1.0f. cutoff %3.0f',k,j(k))))
 end
```

```
 figure(4)
 step=(cutoffhigh-cutofflow)/3;
 for k=1:4
  j=cutofflow:step:cutoffhigh;
  subplot(2,2,k)
  partk=dimg2<j(k);
  imshow(partk);
  title(num2str(sprintf('cutoff %3.0f',j(k))))
 end

 again=input('Do you want to try different cutoff values? (y/n)','s');

end
selector=input('Which image is best? ');
cutoff=cutofflow+step*(selector-1);
end

function out = imoverlay(in, mask, color)
%IMOVERLAY Create a mask-based image overlay.
%   OUT = IMOVERLAY(IN, MASK, COLOR) takes an input image, IN, and a binary
%   image, MASK, and produces an output image whose pixels in the MASK
%   locations have the specified COLOR.

%   Steven L. Eddins, The MathWorks, Inc.
%   $Revision: 1.2 $  $Date: 2007/08/15 13:18:08 $

function vislabels(L)
%VISLABELS Visualize labels of connected components
%   VISLABELS is used to visualize the output of BWLABEL.
%
%   VISLABELS(L), where L is a label matrix returned by BWLABEL,
%   displays each object's label number on top of the object itself.
%
%   Note: VISLABELS requires the Image Processing Toolbox.

%   Steven L. Eddins
%   Copyright 2008 The MathWorks, Inc.

function [ppnm lsb px]=wantscale(pic)
% function to decide how the scale of the image will be determined
decide1=input('Do you want to automatically measure the scale bar? ','s');
      switch decide1
         case {'y' 'Y' 'Yes' 'Sure' 'yes'}
            again='n';
            while again~='y'
            [ppnm lsb px]=findscale(pic);
            sprintf('\tlength of scale bar: %g\n\tpixels in scale bar: %g\n\tpixels per nm: %g\n',lsb,px,ppnm)
            again=input('Is the scale bar length correct?(y/n) ','s');
               switch again
                  case {'y' 'yes' 'Y' 'Yes'}
                     again='y';
                  otherwise
                     again='n'; clf
               end
```

```
            end
            clear again
        otherwise
            px=input('Enter the number of pixels in scale bar: ');
            lsb=input('\nEnter the length of the scale bar, in nm: ');
            ppnm=px/lsb;
    end
end

function pic1=px_square(pic,h)
% read the pixel size in x and y for non-square pixels
if exist('h.XResolution','var')
   xres=h.XResolution;
else
   xres=1;
end
if exist('h.YResolution','var')
   yres=h.YResolution;
else
   yres=1;
end
% resizes the image to make pixels square
pic1=imresize(pic,[size(pic,1)/yres*xres size(pic,2)]);
end
```

A.2 MIE THEORY CODE

```
function results=mie_matlab(wlrange,psize,material_p,material_m,varargin)
% calculate the extinction efficiency for particles of the size 'psize' over the range 'wlrange'
% psize is the diameter of the particle
% material_p is the particle material or refractive index data as follows
% Refractive index data should be in the form:
%   col 1   col 2   col 3
%   wl       n        k
% material_m is the medium material or refractive index
% size and wlrange should be in nm
%
% Set varargin(1) equal to 1 to run a weighted distribution of particle sizes

% Adapted from C. Mätzler, July 2002.

% Particle distribution code
varin=size(varargin);
if varin==1
   if varargin{1}==1
   display('calculating distribution')
   try
      if ndims(psize)==2
      diameter=psize(:,1);
      pdistribution=psize(:,2);
      % normalize the distribution
      pdistribution=pdistribution/sum(pdistribution);
%       pdistribution=pdistribution/max(pdistribution);
```

```
        psize=diameter;
        clear diameter
        else
           error('incorrect input')
        end
    catch ME
        if strcmp(ME.identifier,'MATLAB:badsubscript')
        sprintf('particle distribution requires 2 columns\n\tCol 1\t\tCol 2\n\tparticle size\tnumber of particles')
        else
        display('incorrect input for distribution.  Treating as particle size list...')
        end
    end
    end
end
% end particle distribution code

if ischar(material_p)
switch lower(material_p)
    case {'gold','au'}
        disp('gold')
        [E,n_material]=goldperm(wlrange);
    case {'silver', 'ag'}
        disp('silver')
        [E,n_material]=silverperm(wlrange);
    case {'copper', 'cu'}
        disp('copper')
        [E,n_material]=copperperm(wlrange);
    case {'a_Si'} % amorphous silicon
        disp('amorphous silicon')
        [E, n_material]=asiliconperm(wlrange);
    otherwise
        disp('Material unknown, setting to gold')
        [E,n_material]=goldperm(wlrange);
end
else
    try
    [E,n_material]=genperm(wlrange,material_p);
    catch ME
        display('invalid RI data\n using gold...')
        [E,n_material]=goldperm(wlrange);
    end
end

l_psize=length(psize);
if exist('pdistribution','var')
results.Qsca_total=zeros(size(1,length(wlrange)));
results.Qabs_total=zeros(size(1,length(wlrange)));
results.Qext_total=zeros(size(1,length(wlrange)));
results.pdistribution=pdistribution;
end

% loop for multiple particle sizes
for l_counter=1:l_psize
results.psize(l_counter)=psize(l_counter);
```

```
x=pi.*psize(l_counter)*real(material_m)./wlrange; % psize is diameter
xsq=x.*x;
m=n_material/material_m;
msq=m.*m;
%%%
% results.x=x;
% results.xsq=xsq;
% results.m=m;
% results.msq=msq;
%%%

nmax=max(round(2+x+4*x.^(1/3)));
n=(1:nmax)';
nu = (n+0.5);
z=m.*x;
%%%
% results.nmax=nmax;
% results.n=n;
% results.z=z;
%%%

sqx_1= sqrt(0.5*pi./x);
sqz_1= sqrt(0.5*pi./z);
for c1=1:nmax
   sqx(c1,:)=sqx_1;
   sqz(c1,:)=sqz_1;
end
clear sqx_1 sqz_1 c1
%%%
% results.sqx=sqx;
% results.sqz=sqz;
%%%

bx = besselj(nu, x).'.*sqx;
bz = besselj(nu, z).'.*sqz;
yx = bessely(nu, x).'.*sqx;
hx = bx+1i.*yx;

b1x=[sin(x)./x;bx(1:(nmax-1),:)];
b1z=[sin(z)./z; bz(1:nmax-1,:)];
y1x=[-cos(x)./x; yx(1:nmax-1,:)];

h1x= b1x+1i.*y1x;


for c1=1:nmax
   x1(c1,:)=x;
   z1(c1,:)=z;
   m1(c1,:)=m;
   msq1(c1,:)=msq;
end
n1=zeros(length(n),length(x));
for c1=1:length(x)
   n1(:,c1)=n;
end
```

```
clear c1

ax = x1.*b1x-n1.*bx;
az = z1.*b1z-n1.*bz;
ahx= x1.*h1x-n1.*hx;
an = (msq1.*bz.*ax-bx.*az)./(msq1.*bz.*ahx-hx.*az);
bn = (bz.*ax-bx.*az)./(bz.*ahx-hx.*az);
% cn = (bx.*ahx-hx.*ax)./(bz.*ahx-hx.*az);
% dn = m1.*(bx.*ahx-hx.*ax)./(msq1.*bz.*ahx-hx.*az);

c_n1=2*n1+1;
d_n=c_n1.*(real(an)+real(bn));
q_ex=sum(d_n);

e_n=c_n1.*(real(an).*real(an)+imag(an).*imag(an)+real(bn).*real(bn)+imag(bn).*imag(bn));
q_sca=sum(e_n);

Q_sca=2*q_sca./xsq;
Q_ext=2*q_ex./xsq;
Q_abs=Q_ext-Q_sca;

results.wl=wlrange;
if exist('pdistribution','var')
   Q_sca=Q_sca;
   Q_abs=Q_abs;
   Q_ext=Q_ext;
   results.Qsca_total=results.Qsca_total+Q_sca*pdistribution(l_counter);
   results.Qabs_total=results.Qabs_total+Q_abs*pdistribution(l_counter);
   results.Qext_total=results.Qext_total+Q_ext*pdistribution(l_counter);
end
results.Qsca(l_counter,:)=Q_sca;
results.Qabs(l_counter,:)=Q_abs;
results.Qext(l_counter,:)=Q_ext;


clear Q_abs Q_ext Q_sca ahx an ax az b1x b1z bn bx bz c_n1 d_n e_n h1x hx n n1 nmax...
         nu  q_ex q_sca sqx sqz x x1 xsq y1x yx z z1
end
end



%begin secondary functions
%%%%%%%%%%%%%%%%%%%%%%%%%%%%%%%% GOLD PERM
function [E, n]=goldperm(wavelength) %real and imag components
format compact
% Johnson and Christy
%       wavelength, real,       imaginary component
Data=[187.854545454545,1.28000000000000,1.18800000000000;
         …
         1937.25000000000,0.920000000000000,13.7800000000000;];

%plot(Data(:,1),Data(:,2),'or'); hold all;
%plot(Data(:,1),Data(:,3),'ob');
```

```
nspline=spline(Data(:,1),Data(:,2),wavelength);
kspline=spline(Data(:,1),-Data(:,3),wavelength);
E=(nspline-kspline*1i).^2;
n=(nspline-kspline*1i);
end

function [E, n]=genperm(wavelength, Data)
% Data should be in the form:
%   col 1   col 2   col 3
%   wl       n        k

nspline=spline(Data(:,1),Data(:,2),wavelength);
kspline=spline(Data(:,1),-Data(:,3),wavelength);
E=(nspline-kspline*1i).^2;
n=(nspline-kspline*1i);
end
```

A.3 NANORING GENERATOR

```
function DDAprep(r1,t,h,N_sphere,Px,Py,wlrange,n_materials,n_medium,path_out,varargin)

%   DDAprep prepares the files necessary to evaluate a ring structure with
%   the discrete dipole approximation code DDSCAT 7.2.
%
%   r1 is the inner radius of the ring in nm
%   t is the thickness of the ring wall in nm
%   h is the height of the ring in nm
%   N_sphere is the approximate number of spheres that should represent the
%       thickness of the ring
%   Px and Py are the periodic lattice spacing in x and y directions in nm
%   wlrange is a vector containing the first, last, and number of
%      wavelengths to simulate: [first last num_wavelengths]
%   n_materials is the number of dielectric materials in the sample
%       Currently this is forced to 1, but is available for future use
%   n_medium is the refractive index of the medium (scalar)
%   path_out is the path where files created will be written
%   varargin contains the paths for each dielectric material numbered in
%      n_materials.  These paths should be entered as strings and should
%      represent the path in the run environment: '../au_nk.txt'
%

%   Example DDAprep(60,40,40,5,670,670,[400 1000 601],1,1,'.\rings','..\diel\Au_palik.txt')


% Check to make sure number of paths is equal to the number of materials
n_in=length(varargin);
if n_in~=n_materials
    if n_in==0 && n_materials==1
        n_path='Au_nk.txt';
    else
    error('The number of paths provided must match the number of dielectric materials')
    end
else
    % Assign the paths for the dielectric materials to a cell array
    n_path=varargin;
```

```
end
% initialize the file name for the figure to be saved (see dda_ring_maker
%   for information on the parameters to plot or not)
if exist(datestr(now,'yymmdd'),'dir')~=7
   d_temp=datestr(now,'yymmdd');
   eval(sprintf('mkdir %s',d_temp))
end
try
   filename=[path_out '.\' datestr(now,'yymmdd') '\ring.target' '_' num2str(r1) 'r1_' num2str(t) 't_' num2str(h) 'h_'];
catch
   error('Unable to create file')
end

% Call the ring maker program
[position d]=dda_ring_maker(r1,t,h,N_sphere,1,filename);
% Create a vector to enumerate the dipole positions
dipolenum=1:size(position,1);
% Append the number of dipoles to the filename to distiguish between same
%   rings size with more dipoles.
if exist([filename '.fig'],'file')
   eval(sprintf('movefile("%s","%s")',[filename '.fig'],[filename  num2str(length(dipolenum)) 'N' '.fig']))
end
filename=[filename  num2str(length(dipolenum)) 'N'];
% Create a vector of dipole number; x,y,z location; dielectric number
%   This line will need to be changed if multiple materials are used...
places=[dipolenum' position ones(length(dipolenum),3)];

%% Target file creation
% position vectors relative to lab frame
a1=[0 0 1]; % z axis is x-axis
a2=[1 0 0]; % x axis is y-axis

% Check to see if file already exists.  If it does, it adds a number at the
% end to represent the file version.
c1=0;
while exist(filename,'file')
   c1=c1+1;
   filename=[filename num2str(c1)];
end
clear c1;
fid=fopen(filename, 'at');
% header info
fprintf(fid,...
   ['---Multisphere ring target---\n'... % Description of target
      '%i\t=\t Number of dipoles\n' ... % Number of dipoles in target
      '%f\t%f\t%f\t=\t target vector a1\n'... % x y and z components of a1 in target frame
      '%f\t%f\t%f\t=\t target vector a2\n'... % x y and z components of a2 in target frame
      '1\t1\t1\t=\tdx/d\tdy/d\tdz/d\t(normally 1,1,1)\n'... % relative spacing of dipoles in x, y, and z directions
      '0\t0\t0\t=\tlocation in lattice of target origin\n' ... % target frame co-ordinates corresponding to origin
      'ID\tx\ty\tz\ticx\ticy\ticz\n'... % comment line
      ],length(dipolenum),a1,a2);
fclose(fid);
dlmwrite(filename,places,'-append','delimiter','\t'); % append dipole locations to file

%%  Parameter file creation
```

```
% Change Px and Py to dipole spacing basis
Px=Px/d;    Py=Py/d;
%%%%%%%%%%%%%%%%%%%%%%%%%%%%%%%%%%%%%%%%%%%%%%%%%%%%%
%%%%%%%%%%%%%%%%
% NOTE: period is in x and y in Matlab, with light on z axis, but DDSCAT
%   has the light on the x axis.  The tranlsation is hard coded into this
%   code.
%%%%%%%%%%%%%%%%%%%%%%%%%%%%%%%%%%%%%%%%%%%%%%%%%%%%%
%%%%%%%%%%%%%%%%

%   pradius:  effective particle radius in nm
pradius=(3*length(dipolenum)/(4*pi))^(1/3)*d;

% Declare DDSCAT simulation parameters
%   an example user interface is available in the
%   DDA_parameter_file_maker.m file, but is currently not included here
%   since these normally stay the same
torque1='NOTORQ';
solmethod='PBCGS2';
% fftmethod='FFTMKL';
fftmethod='GPFAFT';
polmodel='GKDLDR';
binmode='NOTBIN';
Memreq=[100 100 100]*2;
Nfield=0;
Nfield_size=[0.5 0.5 0.5 0.5 0.5 0.5];
maxtol=1e-5;
maxiter=3000;
gamma1=5e-3;
S_index=[11 12 21 22 31 41];
NSO=1; %Number of scattering orders

filename1=[path_out '.\' datestr(now,'yymmdd') '\ddscat' '_' num2str(r1) 'r1_' num2str(t) 't_' num2str(h) 'h_'
num2str(length(dipolenum)) 'N'];
c1=0;
% Check to see if file already exists.  If it does, it adds a number at the
% end to represent the file version.
while exist([filename1 '.par'],'file')
   c1=c1+1;
   filename1=[filename1 num2str(c1)];
end
clear c1;
fid1=fopen([filename1 '.par'], 'wt');
d_temp=datestr(now,'yymmdd');
% header info
% fprintf(fid,'%i\t%f\t%f\n---Multisphere ring target---\na1 vector\na2
vector\nx\ty\tz\ta\tic1\tic2\tic3\tth\tph\tbe\n',length(dipolenum),0,0);
fprintf(fid1,'" ========= Parameter file for v7.2; created: %s ==================="\n', d_temp );
fprintf(fid1,'"**** Preliminaries ****"\td=%f\n',d);
fprintf(fid1,'"%s" = CMTORQ*6 (NOTORQ, DOTORQ) -- either do or skip torque calculations\n',torque1);
fprintf(fid1,'"%s" = CMDSOL*6 (PBCGS2, PBCGST, PETRKP) -- select solution method\n',solmethod);
fprintf(fid1,'"%s" = CMDFFT*6 (GPFAFT, FFTMKL)\n',fftmethod);
fprintf(fid1,'"%s" = CALPHA*6 (GKDLDR, LATTDR)\n',polmodel);
fprintf(fid1,'"%s" = CBINFLAG (NOTBIN, ORIBIN, ALLBIN)\n',binmode);
```

```
fprintf(fid1,'"**** Initial Memory Allocation ****"\n');
fprintf(fid1,'%i\t%i\t%i = dimensioning allowance for target generation\n',Memreq);
fprintf(fid1,'"**** Target Geometry and Composition ****"\n');
fprintf(fid1,'"FRMFILPBC" = CSHAPE*9 shape directive\n');
fprintf(fid1,'%f\t%f\t "%s" (quotes must be used)\n',Px,Py,filename);
% SHPAR1 = Py/d (Py = periodicity in yTF direction)
% SHPAR2 = Pz/d (Pz = periodicity in zTF direction)
fprintf(fid1,'%i = NCOMP = number of dielectric materials\n',n_materials);
for c1=1:n_materials
   fprintf(fid1,'"%s"\n',n_path{c1});
end
fprintf(fid1,'"**** Additional Near field calculation? ****"\n');
fprintf(fid1,'%i = NRFLD (=0 to skip, 1 to calculate nearfield E)\n',Nfield);
fprintf(fid1,'%f\t%f\t%f\t%f\t%f\t%f\t (fract. extens. of calc. vol. in -x,+x,-y,+y,-z,+z)\n',Nfield_size);
fprintf(fid1,'"**** Error Tolerance ****"\n');
fprintf(fid1,'%f\t= TOL = MAX ALLOWED (NORM OF |G>=AC|E>-ACA|X>)/(NORM OF AC|E>)\n',maxtol);
fprintf(fid1,'"**** Maximum number of iterations allowed ****"\n');
fprintf(fid1,'%i\t= MXITER\n',maxiter);
fprintf(fid1,'"**** Interaction cutoff parameter for PBC calculations ****"\n');
fprintf(fid1,'%f\t= GAMMA (1e-2 is normal, 3e-3 for greater accuracy)\n',gamma1);
fprintf(fid1,'"**** Angular resolution for calculation of <cos>, etc. ****"\n');
fprintf(fid1,'%f\t= ETASCA (number of angles is proportional to [(3+x)/ETASCA]2 )\n',2.0);
fprintf(fid1,'"**** Vacuum wavelengths (micron) ****"\n');
wlrange(1:2)=wlrange(1:2)/1e3; % convert wl to m from nm
fprintf(fid1,'%f\t%f\t%i\t"%s" = wavelengths (first,last,how many,how=LIN,INV,LOG)\n',wlrange,'LIN');
fprintf(fid1,'"**** Refractive index of ambient medium ****"\n');
fprintf(fid1,'%f\t= NAMBIENT\n',n_medium);
fprintf(fid1,'"**** Effective Radii (micron) ****"\n');
pradius=pradius/1e3; % convert radius to µm from nm
fprintf(fid1,'%f\t%f\t%i\t"%s" = eff. radii (first, last, how many, how=LIN,INV,LOG)\n',pradius,pradius,1,'LIN');
fprintf(fid1,'"**** Define Incident Polarizations ****"\n');
fprintf(fid1,'(0,0) (1.,0.) (0.,0.) = Polarization state e01 (k along x axis)\n');
fprintf(fid1,'%i = IORTH (=1 to do only pol. state e01; =2 to also do orth. pol. state)\n',1);
fprintf(fid1,'"**** Specify which output files to write ****"\n');
fprintf(fid1,'%i = IWRKSC (=0 to suppress, =1 to write ".sca" file for each target orient.\n',0);
% fprintf(fid1,'%i = IWRPOL (=0 to suppress, =1 to write ".pol" file for each (BETA,THETA)\n',1);
fprintf(fid1,'"**** Prescribe Target Rotations ****"\n');
fprintf(fid1,'%f\t%f\t%i = BETAMI, BETAMX, NBETA (beta=rotation around a1)\n',0,0,1);
fprintf(fid1,'%f\t%f\t%i = THETMI, THETMX, NTHETA (theta=angle between a1 and k)\n',0,0,1);
fprintf(fid1,'%f\t%f\t%i = PHIMIN, PHIMAX, NPHI (phi=rotation angle of a1 around k)\n',0,0,1);
fprintf(fid1,'"**** Specify first IWAV, IRAD, IORI (normally 0 0 0) ****"\n');
fprintf(fid1,'%g\t%g\t%g = first IWAV, first IRAD, first IORI (0 0 0 to begin fresh)\n',0,0,0);
fprintf(fid1,'"**** Select Elements of S_ij Matrix to Print ****"\n');
fprintf(fid1,'%i = NSMELTS = number of elements of S_ij to print (not more than 9)\n',length(S_index));
%define S_ij indices to print
fprintf(fid1,'%i\t%i\t%i\t%i\t%i\t%i\t%i = indices ij of elements to print\n',S_index);
fprintf(fid1,'"**** Specify Scattered Directions ****"\n');
fprintf(fid1,'"%s" = CMDFRM (LFRAME, TFRAME for Lab Frame or Target Frame)\n','TFRAME');
fprintf(fid1,'%i = number of scattering orders\n',NSO);
fprintf(fid1,'%i\t%i = M, N (diffraction orders)\n',0,0);

fclose(fid1);
dlmwrite(filename,places,'-append','delimiter','\t');
end
```

```
%% Internal functions
function circle_points=pixelator(r_eff)
% creates a pixelated circle where r_eff is the radius divided by the lattice spacing, d
% returns the points of the circle edge for the first quadrant
r=round(r_eff);

% based on code by John Kennedy, "A fast Bresenham type algoritm for drawing circles
y=0;
x=r;

xchange=1-2*(r);
% ychange=2*y+1;
RE=0;
c1=0;
while x>=y
   c1=c1+1;
   x_total(c1)=x;
   y_total(c1)=y;
   RE=x^2+y^2-r^2;
   ychange=2*y+1;
   y=y+1;
   if (2*(RE+ychange)+xchange)>0
      xchange=-1-2*x;
      x=x-1;
   end
end
x=x_total; y=y_total;
circle_points=[x y(end:-1:2); y x(end:-1:2)]';
end

function [position d]=dda_ring_maker(r1,t,h,N_sphere,varargin)
%   Generate target file to use wil from_file option with DDSCAT 7.1
%   Target is a ring structure where
%   r1 is the inner radius
%   t is the wall thickness
%   h is the height of the ring structure
%   N_sphere is the minimum number of spheres in the thickness direction
%   Set varargin to 1 to plot the resulting ring structure
%   WARNING:  Plotting structures with large numbers of dipoles can take
%            very long and be very memory intensive.
%
%   position is a matrix containing column vectors for each dipole in
%   x, y, and z, respectively.

% % % r1=79.4;  N_sphere=1; t=30; h=50;
%%
nvarin=length(varargin);
switch nvarin
   case 0
      plotyes=0;
   case 1
      if varargin{1}==1
         plotyes=1;
      else
         plotyes=0;
```

```
        end
    case 2
        if varargin{1}==1
            plotyes=1;
        else
            plotyes=0;
        end
        if ischar(varargin{2})
            filename=varargin{2};
        else
            plotyes=0;
        end
    otherwise
        plotyes=0;
end

% Define outer radius
r2=r1+t;

% calculate dipole diameter that gives the best approximation to t and h
d=t/N_sphere;
th_ratio=t/h;
c1=t*h*N_sphere;
while  (mod(t,d)~=0 || mod(h,d)~=0 || mod(r1,d)~=0) && c1>0
    c1=c1-1;
    d=t/floor(th_ratio*100)*c1/100;
%      [t/d    h/d    r1/d]
end
if c1==0
    d=1;
end
clear c1
% h_offset=d*sin(pi/3); % Trig value for touching spheres on equilateral triangle times
h_offset=round(h/d);
% N_layer=round(h/(h_offset));
N_layer=h_offset;

cp1=pixelator(r1/d);
cp2=pixelator(r2/d);

cm=[];
% outer circle points
for c1=1:length(cp2)
    for c2=1:cp2(c1,1)
        cm=[cm; [c2 cp2(c1,2)]];
    end
end
cm1=[];
cm3=cm;
if t>0
% inner circle points
    for c1=1:length(cp1)
        for c2=1:cp1(c1,1)
            cm1=[cm1; [c2 cp1(c1,2)]];
        end
```

```
    end
end
for c1=1:length(cm1)
   cm3( (cm1(c1,1)==cm(:,1) & cm1(c1,2)==cm(:,2)))=999;  % mark rows to be removed
end
cr=[]; % rows to be left
for c1=1:length(cm3)
    if cm3(c1,1)~=999
        cr=[cr c1];
    end
end
cm4=cm3(cr,:);
cm5=cm4;
for c1=pi/2:pi/2:2*pi
    % co-ordinate transform to create all quadrants
    cm5=[[cm5(:,1) cm5(:,2)]; [cm4(:,1)*cos(c1)-cm4(:,2)*sin(c1) cm4(:,1)*sin(c1)+cm4(:,2)*cos(c1)]];
end
clear cm cm1 cm3 cm4 cr cp1 cp2

N_dipole_layer=length(cm5);
cm5(:,3)=ones(N_dipole_layer,1);
cm=cm5;
for c_height=2:N_layer
    cm5=round([cm5; [cm(:,1) cm(:,2) cm(:,3)+(c_height-1)]]);
end
clear cm
N_dipole=length(cm5);
% define output matrix
position_temp=cm5;
position=[position_temp(:,1) position_temp(:,2) position_temp(:,3)];
clear position_temp;
cm5=position;
%%  Plot sphere locations
if plotyes
    %%
    if ~exist('r2','var')
        r2=r1+t;
    end
    if ~exist('cm5','var')
        cm5=position;
    end
%     [spx spy spz]=sphere(10);
    figure(10)
%     set(gcf,'visible','off')
    clf
    hold all
    if t>0
    % plot input ring size
    [X1 Y1 Z1]=cylinder(r1);
    Z1(Z1==1)=h;
    hcyl1=surf(X1,Y1,Z1,'facecolor','r');
    alpha(hcyl1,0.2)
    [X2 Y2 Z2]=cylinder(r2);
    Z2(Z2==1)=h;
    hcyl2=surf(X2,Y2,Z2,'facecolor','g');
```

```
    alpha(hcyl2,0.2)
    end
    % plot actual ring size
    cm5(cm5 == 0) = cm5(cm5 == 0) -0.5;
    cm5(cm5 < -0.5) = cm5(cm5 < -0.5) +0.5;
    cm5(cm5 > 0) = cm5(cm5 > 0) -0.5;
    h1=plot3(cm5(:,1)*d,cm5(:,2)*d,cm5(:,3)*d,'o','MarkerFaceColor','b',...
        'markeredgecolor','k','markersize',12);
    % generate axis line
    X=[0 0]; Y=[0 0]; Z=[min(cm5(:,3))*d-d*3,max(cm5(:,3))*d+d*3];
    plot3(X,Y,Z,'color','black','linestyle','--','linewidth',6)
    grid
    view(gca,[90,0,0])
    axis equal
    hold off
    try
    saveas(gcf,[filename '.fig'])
    close (10)
    catch ME
        display('Unable to save image')
    end

    %%
end
end
```